2011

Development, Deployment, and Characterization of a Ku-band Interferometer

Anthony Swochak
University of Massachusetts Amherst

DEVELOPMENT, DEPLOYMENT, AND CHARACTERIZATION OF A KU-BAND INTERFEROMETER

A Thesis Presented

by

ANTHONY F. SWOCHAK

Submitted to the Graduate School of the
University of Massachusetts Amherst in partial fulfillment
of the requirements for the degree of

MASTER OF SCIENCE IN ELECTRICAL AND COMPUTER ENGINEERING

September 2011

Electrical and Computer Engineering

DEVELOPMENT, DEPLOYMENT, AND CHARACTERIZATION OF A KU-BAND INTERFEROMETER

A Thesis Presented

by

ANTHONY F. SWOCHAK

Approved as to style and content by:

Paul R. Siqueira, Chair

Stephen J. Frasier, Member

Robert W. Jackson, Member

Christopher V. Hollot, Department Chair
Electrical and Computer Engineering

For my mother and father.

The scientific man does not aim at an immediate result. He does not expect that his advanced ideas will be readily taken up. His work is like that of the planter — for the future. His duty is to lay the foundation for those who are to come, and point the way. He lives and labors and hopes.

Nikola Tesla
(1856 - 1943)

ACKNOWLEDGMENTS

I would like to thank Professor Paul Siqueira for taking me under his wing during a time when I wasn't sure about continuing a Master's thesis degree. His constant encouragement during my research made it possible for me to be where I am today. He is an excellent advisor, colleague, and, most of all, friend. I would also like to thank Professor Stephen Frasier and Professor Robert Jackson for their professional and academic advice, ensuring that the quality of my work met the highest standards.

I would like to thank all the people at MIRSL. This thesis would not have been possible without their constant support and friendship over the years. For my friends in and out of the lab, I thank you. Harish the source of infinite wisdom and laughter without him I would not know the difference between a 2.4mm cable and a SMA, Iva and Ilke for the long study sessions endured during my first semester as a graduate student, Jorge Salazar. for teaching me everything about antennas, your enthusiasm is contagious, Jeff and Mike for playing catch in the quad and the many trips to PVP, Razi for being the big brother I never had, and keeping me sane with football, Tau for coining "Sumo" Tony, Vijay for the late night trips to Cumby's for coffee and smokes, Kris for teaching me the Polish way to say small barrel (beczulka) and small turtle (zolwik), Mandy for being the little sister I never had, I will never forget that your favorite color is orange, Brian, Shanka, and Lily for the Fresh Side parties where a Japanese Omelette was always on the menu, Jason Dvorsky for sharing his peanut butter and banana sandwiches, Joe for our shared passion for the Bruins, Jason Donovan for his unlimited movie references, Tom and Pei for helping me get started in the lab, Caitlin who always found time for an afternoon chat, Mauricio for his help when I was having circuit board problems, Ogechi who always brought

a smile to my face even on the gloomiest days, Jorge Trabal, Ibis, and Rafael for introducing me to Puerto Rican food where I learned that a large plate of food really means lots of rice, Benjamin for the chess matches which always ended badly for me, Seth, Steve, Jason, Chris, and Georgios (APL guys) for letting me sit at lunch with them whenever I was on my own at the Blue Wall, Kan and Yang for taking time out of their day to help me setup the radar, and Rockwell for taking charge of the project that I've spent countless hours on. If I have forgotten anyone, I extend my deepest thanks.

I would also like to thank Linda Klemyk and Mary Nied for their help with the administrative side of things at MIRSL. I would also like to thank Jim Bernotas at Amherst Machine for fabricating the antennas as well as the nice folks at Mount Holyoke and Mount Sugarloaf for letting us setup the radar at those locations.

Most of all, I would like to thank my family and friends back home whose constant support and love motivated me to continue forward even through some of the most stressful times of my life, if I caused any worry during those times, I apologize. I love you all and God bless.

ABSTRACT

DEVELOPMENT, DEPLOYMENT, AND CHARACTERIZATION OF A KU-BAND INTERFEROMETER

SEPTEMBER 2011

ANTHONY F. SWOCHAK

B.Sc., UNIVERSITY OF MASSACHUSETTS AMHERST

M.S.E.C.E., UNIVERSITY OF MASSACHUSETTS AMHERST

Directed by: Professor Paul R. Siqueira

Space-borne radar interferometry provides a global vantage point to understand climate change, global weather phenomenon, and other Earth dynamics. For climate change observations, space-borne interferometers can be utilized to relate ocean topography to temperature, thus providing a global map of ocean temperatures. Since the oceans are in constant motion, a single-pass interferometer is needed to successfully make these measurements of ocean height. The feasibility of a single-pass measurement is dependent on the physical size of the instrument, hence it is cheaper and more practical to launch a small, light weight instrument into space. Since instrument size scales inversely with operating frequency, high frequency microwave technology (Ku-band and Ka-band) is preferred for these types of applications. However, space-borne deployments become more difficult to implement at these frequencies since the physical structure of the instrument changes in the harsh environment of space. For that reason, a ground-based Ku-band (13.245GHz) radar interferometer has been

developed at the University of Massachusetts, Amherst Microwave Remote Sensing Laboratory (MIRSL). In this thesis, a description of the radar hardware as well as interferometric results from Mount Sugarloaf provide a measure of the performance of the radar and demonstrate the capabilities of using a ground-based interferometer as a test-bed for space-borne applications.

TABLE OF CONTENTS

LIST OF TABLES

Table **Page**

LIST OF FIGURES

Figure **Page**

CHAPTER 1

INTRODUCTION

1.1 History and Motivation

Knowledge of the Earth's climate and geology are important to our understanding of the dynamics of this planet. Efforts to collect and catalog ocean height and surface topography using radar interferometers have contributed significantly to understanding climate change, weather forecasting, and other crucial environmental changes. Thus far, our investment into the study of radar interferometry has ranged from topographic maps of the Moon [22] and Venus [13] to the SRTM[1], which cataloged 80% of the Earth's topography over an 11 day period. Future endeavors in Earth science, oceanography, and cryospheric studies, with interferometers like SWOT[2] and DESDynI[3], are in place to explore these phenomenon, and improve the technology necessary for global scale deployments to measure topographic changes over short time scales.

Because the physical structure of the interferometer is inversely proportional to the operating frequency of the instrument, the challenge of improving high frequency microwave technology for space deployments is crucial to the future of radar interferometry. This is most critical at Ku- and Ka-band frequency ranges which are known to be suitable for oceanic and cryospheric applications because of their ability to

[1]Shuttle Radar Topography Mission. See http://www2.jpl.nasa.gov/srtm/ for more details.

[2]Surface Water and Ocean Topography. Visit http://swot.jpl.nasa.gov/ for more details.

[3]Deformation, Ecosystem Structure and Dynamics of Ice. Visit http://desdyni.jpl.nasa.gov/ for more details.

achieve single-pass interferometry from low Earth orbit [2]. At these frequencies, the temperature fluctuations that satellites experience in space present a problem in the performance of microwave circuitry. Under these conditions, temperature modeling and calibration are needed to compensate for errors introduced by the expansion and contraction of metal, among other effects. This added complexity in the radar system necessitates the need to design, develop, and deploy simpler, ground-based platforms to serve as test-beds for future space-borne interferometers.

The goal of this thesis is the development and implementation of a Ku-Band radar interferometer. Previously, a Ku-band radar interferometer [19] was designed and developed at the University of Massachusetts (UMass) for testing a 20MHz dual-channel microwave receiver; however, the range resolution and data acquisition limitations inhibited successful deployment of the radar system. As a result, a 100MHz version of the same receiver was built at Ka-band and Ku-band, and was successfully implemented in a Ka-band radar interferometer [18], but was never integrated into a radar system at Ku-band. It is the objective of this master's thesis to build a working Ku-band radar interferometer around the existing revised dual-channel Ku-band receiver. The outcome of this thesis will compare data collected over a region with known topography, thus providing an opportunity to measure the accuracy, performance, and limitations of the UMass Ku-band interferometer.

1.2 Summary of Chapters

Chapter 2 will describe radar interferometry from the perspective of a ground-based radar. This chapter will illustrate the interferometric viewing geometry, discuss interferometric phase estimation, and other mathematical relationships formed from interferometric radar observations. Chapter 3 will describe the basic principles of FM-

CW[4] radar and describe the radar processing. Chapter 4 will provide a description of the radar system hardware and also give a detailed description of the antenna. Chapter 5 discusses hardware performance of the receiver, transmitter, and antenna. Chapter 6 describe the locations where the radar was deployed as well as initial results, the improvements made to the hardware, and subsequent results obtained from Mt. Sugarloaf. Chapter 7 will provide a summary of work completed as well as recommendations for future work.

[4]Frequency Modulated - Continuous Wave

CHAPTER 2

FUNDAMENTALS OF RADAR INTERFEROMETRY

2.1 Introduction

Radar interferometry is a remote sensing technique that has evolved over the years into an excellent way to measure topography, topographic change, and other geophysical phenomenon. Our understanding of radar interferometry as an effective means of measuring these global scale phenomena is owed to the contribution from scientists and engineers in the years following World War II. The first description of aircraft based interferometry was introduced by Graham [6] in 1974, detailing airborne synthetic aperture radar (SAR) interferometry as viable alternative to stereography from photographs where the requirement of fair weather limits deployment. Today, UAVSAR[1], a JPL (Jet Propulsion Laboratory) and NASA (National Aeronautics and Space Administration) supported project, represents one of the latest airborne platforms in operation, providing high-resolution images for missions ranging from topographical surveys to earthquake damage assessment [10]. One of the first spaceborne interferometric observations utilized data collected from the Seasat SAR mission conducted in 1978. Originally launched for the purpose of measuring the ocean surface, Seasat data was eventually used to demonstrate the capabilities of spaceborne interferometry using a technique called repeat-pass interferometry [11][14]. It should be noted that there are numerous interferometric configurations, each geared to a specific measurement or observation. Repeat-pass interferometry is one technique in which

[1]Uninhabited Aerial Vehicle Synthetic Aperture Radar. Visit http://uavsar.jpl.nasa.gov/ for more detail

measurements rely on the temporal coherence between observations taken at different times along the same flight-path or orbit. The dual to cross-track interferometry is along-track interferometry, which measures a targets velocity. In this chapter, discussion of cross-track interferometry will be the main focus, and is more suited for measurements of topography and topographic change. Thus, the successful analysis and interpretation of data from the Ku-band radar interferometer will require an understanding of the interferometric viewing geometry, the mathematical principles governing interferometry, and the measurement of topography.

2.2 Interferometric Phase Estimation

Radar interferometers work on the principle of "interfering" backscattered radio waves. When two antennas, A_1 and A_2, are separated by a baseline B, the range, R, to the observed target is different between antennas by ΔR. Since R is usually large, it can assumed that the returning echo is a plane wave. The phase difference between observations can be written as,

$$\phi = k\Delta R \tag{2.1}$$

where k is the free-space wavenumber. This phase difference can be estimated by taking the cross-correlation between the complex baseband voltages initially measured at A_1 and A_2,

$$\gamma = \frac{\langle V_1 V_2^* \rangle}{\sqrt{\langle |V_1|^2 \rangle \langle |V_2|^2 \rangle}} = \gamma_0 e^{-j\phi} \tag{2.2}$$

where (2.2) is referred to as a radar interferogram. Figure 2.1 shows the geometric configuration for a cross-track interferometer where a complete description of key interferometry parameters are listed in Table 2.1.

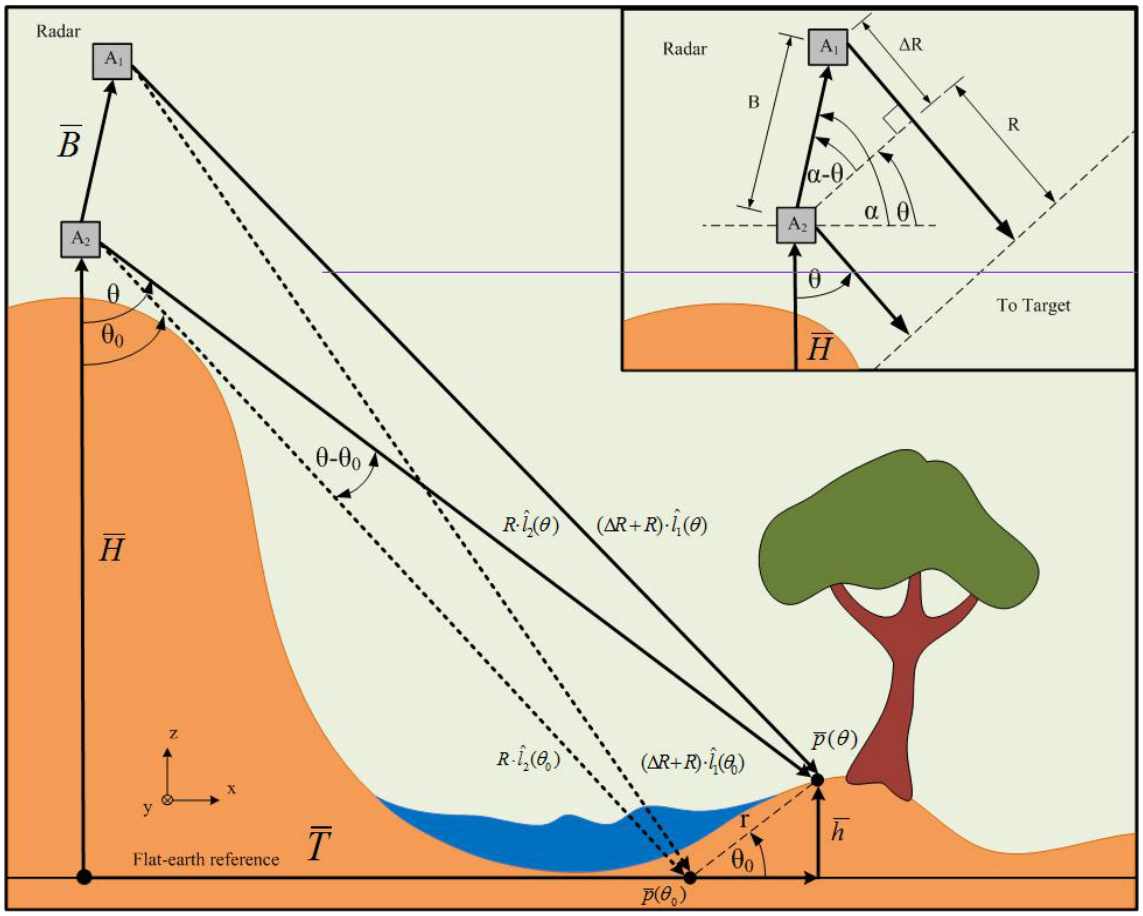

Figure 2.1. Illustration of the interferometer geometry.

2.3 Height Estimation

In the past, the height of terrain was measured with the use of human operated surveying tools. These tools paved the way for cartographers and surveyors alike, making the tasks they performed using levels, rope, and measuring sticks faster and efficient using radar interferometers. Using Figure 2.1, the height can be estimated by using the viewing geometry to express height as a function of the measure interferometric phase. By doing so, height can be expressed mathematically as,

$$|\bar{h}| = |\bar{H}| - R\cos(\theta). \tag{2.3}$$

Parameters	Description
θ	Look-angle with respect to nadir.
$\bar{p}(\theta)$	Observation point.
θ_0	"Flat-Earth" look-angle with respect to nadir.
$\bar{p}(\theta_0)$	"Flat-Earth" observation point.
α	Baseline tilt angle.
r	Slant distance between $\bar{p}(\theta)$ and $\bar{p}(\theta_0)$.
A_1	Antenna #1.
$\hat{l}_1$	A_1 unit look-vector.
A_2	Antenna #2.
$\hat{l}_2$	A_2 unit look-vector.
$\bar{B}$	Baseline vector.
R	Range to target.
H	Height of the radar assembly.
ΔR	Range difference between A_1 and A_2.
$\bar{h}$	Elevation of the terrain.
$\bar{T}$	Lateral distance from radar $\bar{p}(\theta)$.

Table 2.1. Key Interferometry Parameters

where the relationship between look-angle, θ, and interferometric phase, ϕ, is defined by rewriting the observation point or resolution element, $\bar{p}(\theta)$, in terms of the vectors illustrated in Figure 2.1 and described in Table 2.1. The observation vector, $\bar{p}(\theta)$, can be written as,

$$\bar{p}(\theta) = \bar{T} + \bar{h} = \bar{H} + R \cdot \hat{l}_2(\theta) \tag{2.4}$$

$$\bar{p}(\theta) = \bar{T} + \bar{h} = \bar{H} + \bar{B} + (\Delta R + R) \cdot \hat{l}_1(\theta). \tag{2.5}$$

By assuming a far-field approximated geometry, mathematically represented as $\hat{l}_1(\theta) \approx \hat{l}_2(\theta) = \hat{l}$, it becomes possible to equate (2.4) and (2.5) resulting in the following,

$$\Delta R = -\bar{B} \cdot \hat{l} = -B \sin(\alpha - \theta). \tag{2.6}$$

By substituting (2.6) into (2.1), an expression of ϕ indicative of the interferometric geometry can be shown as

$$\phi = -kB \sin(\alpha - \theta). \tag{2.7}$$

By rearranging terms in (2.7), θ can be expressed as

$$\theta = \alpha - \sin^{-1}\left(\frac{\phi}{kB}\right). \tag{2.8}$$

From (2.8), a relationship between look-angle, θ, interferometric phase, ϕ, and baseline separation, B, can be shown. Thus, by substituting (2.8) into (2.3), a formula for height as a function of the measured interferometric phase can be expressed as

$$|\bar{h}| = |\bar{H}| - R\cos\left(\alpha - \sin^{-1}\left(\frac{\phi}{kB}\right)\right). \tag{2.9}$$

Because interferograms are products obtained over large swaths, most of the topographic information is modulated by θ_0, denoted as the "flat-Earth" look-angle due to the local appearance of the Earth's surface from the perspective of the radar. As a result, the measured interferometric phase shown in (2.1) and (2.7) can be written as a sum of the phase quantities representing effects by both the ground topography and the "flat-Earth" look-angle [3] since these quantities are measured simultaneously by the radar. Mathematically this can be expressed as

$$\phi = \phi_{\text{topography}} + \phi_{\text{flat-Earth}} \tag{2.10}$$

where by subtracting out the $\phi_{\text{flat-Earth}}$, a "flattened" interferogram representative of only topography can be obtained.

An alternative expression for the height of the terrain can be achieved by interpreting topographic relief in terms of small perturbations in the "flat-Earth" look-angle, θ_0. In other words, topography can be thought as changes in look-angle between the "flat-Earth" observation point, $\bar{p}(\theta_0)$, and the target observation point, $\bar{p}(\theta)$, in which

the range from the radar to each of these two observation points are equal. Thus, an expression for the target look-angle can be written as

$$\theta = \theta_0 + \Delta\theta \tag{2.11}$$

where $\Delta\theta$ is the look-angle difference between $\bar{p}(\theta)$ and $\bar{p}(\theta_0)$. By assuming $\Delta\theta$ to be very small, the distance between $\bar{p}(\theta)$ and $\bar{p}(\theta_0)$ can be approximated as the arc length between the two points. As a result, $\Delta\theta$ can be expressed as

$$\Delta\theta \approx \frac{|\bar{h}|}{R\sin(\theta_0)}. \tag{2.12}$$

By combining (2.11) and (2.7), a new result for ϕ in terms of θ_0 can be shown as

$$\phi = -kB\sin((\alpha - \theta_0) - \Delta\theta). \tag{2.13}$$

By applying a trigonometric identity, (2.13) expands into the following form

$$\phi = -kB[\sin(\alpha - \theta_0)\cos(\Delta\theta) - \cos(\alpha - \theta_0)\sin\Delta\theta]. \tag{2.14}$$

Since (2.12) was established to be very small, a small argument approximation can be used to simplify (2.14) into the following expression,

$$\phi \approx -kB\sin(\alpha - \theta_0) + kB\cos(\alpha - \theta_0)\frac{|\bar{h}|}{R\sin(\theta_0)}, \tag{2.15}$$

which is equivalent to the far-field approximation of having a planar phase front. Here the phase components from (2.10) are clearly represented as the following

$$\phi_{\text{flat}-\text{Earth}} = -kB\sin(\alpha - \theta_0) \tag{2.16}$$

$$\phi_{\text{topography}} = kB\cos(\alpha - \theta_0)\frac{|\bar{h}|}{R\sin(\theta_0)}. \tag{2.17}$$

Hence, by measuring ϕ using (2.2), it becomes possible to estimate the topography $|\bar{h}|$ for all line-of-sight directions.

2.4 Interferometric Performance Assessment

Assessment of radar performance can be determined by focusing attention to the accuracy and sensitivity of height measurements as well as spatial resolution. These parameters not only give us a useful way of determining performance but also provides a quantitative method for determining which components of the hardware will most influence the measurement error. How the radar configuration effects accuracy, sensitivity, and resolution can be shown using the illustration of the interferometric viewing geometry given by Figure 2.1.

2.4.1 Height Accuracy

As seen earlier, height is obtained by triangulating range data collected from A_1 and A_2. It can be shown from (2.3), that the accuracy of height measurements is dependent on known parameters of baseline, B, radar height, $|\bar{H}|$, slant range, R, cross-track tilt angle, α, interferometric phase, ϕ, and radar wavelength, λ . Hence, the error in height can be treated as a weighted sum of error sources within the radar system [5]. By applying a Taylor series approximation to each error source, it becomes possible to determine how each source contributes to the overall height error,

$$\sigma_{|\bar{h}|}{}^2 = (a_R\sigma_R)^2 + (a_B\sigma_B)^2 + (a_{|\bar{H}|}\sigma_{|\bar{H}|})^2 + (a_\alpha\sigma_\alpha)^2 + (a_\phi\sigma_\phi)^2 + (a_\lambda\sigma_\lambda)^2, \tag{2.18}$$

where

$$a_R = \frac{\partial|\bar{h}|}{\partial R} + \frac{\partial|\bar{h}|}{\partial\beta}\frac{\partial\beta}{\partial R} \tag{2.19}$$

$$a_B = \frac{\partial|\bar{h}|}{\partial\beta}\frac{\partial\beta}{\partial B} \tag{2.20}$$

$$a_{|\bar{H}|} = \frac{\partial|\bar{h}|}{\partial|\bar{H}|} \tag{2.21}$$

$$a_{\alpha} = \frac{\partial|\bar{h}|}{\partial\alpha} \tag{2.22}$$

$$a_{\phi} = \frac{\partial|\bar{h}|}{\partial\beta}\frac{\partial\beta}{\partial(\Delta R)}\frac{\partial(\Delta R)}{\partial\phi} \tag{2.23}$$

$$a_{\lambda} = \frac{\partial|\bar{h}|}{\partial\beta}\frac{\partial\beta}{\partial(\Delta R)}\frac{\partial(\Delta R)}{\partial\lambda}. \tag{2.24}$$

2.4.2 Ground Resolution

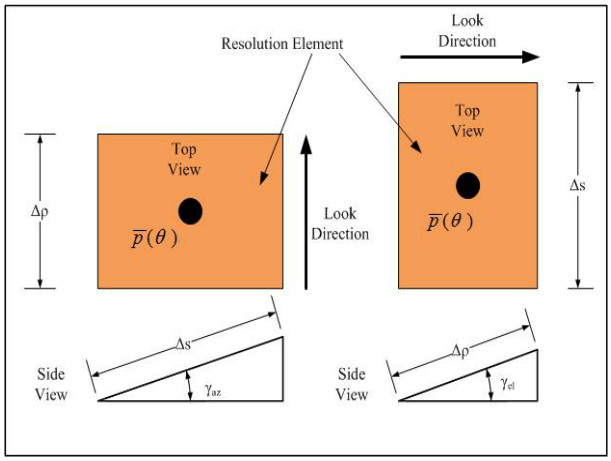

Figure 2.2. Illustration of Resolution Element $p(\theta)$.

The ability to distinguish between objects between observations depends on the spatial resolution of the radar. In this case, the resolution is determined by the radar's bandwidth, Δf and the antenna azimuthal half-power beamwidth, ϕ_{3dB}. Determining the spatial resolution requires definition of each resolution element, $p(\theta)$, seen in Figure 2.1. Figure 2.2 describes the radar observed terrain as a collection of facets or resolution elements. The area illuminated by the radar's antenna is defined as

$A = \Delta\rho\Delta s$, where the $\Delta\rho$ and Δs are defined as the cross- and along-track resolution, respectively, their mathematical representations are given as follows,

$$\Delta\rho = \frac{\Delta r}{\sin(\theta - \gamma_{\text{el}})} \tag{2.25}$$

$$\Delta s = \frac{R\phi_{3dB}}{\cos(\gamma_{\text{az}})} \tag{2.26}$$

where γ_{el} and γ_{az} represent the relative cross- and along-track slopes in terrain. Note that (2.26) neglects the contribution of baseline tilt in azimuth.

In order to fully grasp the concept of radar interferometry requires a detailed understanding of the interferometric viewing geometry and corresponding mathematical representations. Thus far, a description of radar interferometry has been presented in terms of the estimation of interferometric phase, the geometric interpretation of interferometry, the estimation of height, and the performance assessment of height. By understanding these fundamental concepts, it becomes clear as to the role of the radar and the types of radars capable of making interferometric measurements. In the following chapter, a description of FM-CW radar fundamentals and data processing are presented, thus providing an explanation as to how interferometric measurements are obtained.

CHAPTER 3

FUNDAMENTALS OF FM-CW RADAR

An FM-CW radar operates based on a pulse compression technique used in low peak-power applications such as marine navigation and radar interferometry. Regarding interferometric applications, this technique has been shown to be useful for ground-based measurements [18][20]. In this chapter, a discussion and description of the basic principles of FM-CW radar is provided. A section on data processing is also covered.

3.1 Basic Principles

In conventional pulsed-radar systems, the range-to-target is measured by calculating the round-trip time between the radar and target. Because the speed of the transmitted pulse, $c = 3 \times 10^8$m/s, it is possible to calculate the range using the round-trip time, t, measured from the radar echo. Thus,

$$R = \frac{ct}{2} \tag{3.1}$$

The maximum unambiguous range, R_{unamb}, is determined by substituting the pulse repetition time (PRT), T, with the round-trip time, t, from (3.1). The range resolution is a function of the pulse-width of the transmitted waveform, τ; thus,

$$\Delta r = \frac{c\tau}{2}. \tag{3.2}$$

In the case of pulsed radar, there is a tradeoff between increasing range resolution and sensitivity of the radar. The sensitivity for a single pulse radar can be expressed in terms of the signal-to-noise ratio (SNR) shown as

$$\mathrm{SNR}_1 = \frac{P_t G^2 {\lambda_0}^2 \sigma}{(4\pi)^3 R^4 k T_0 \Delta f F} \tag{3.3}$$

where P_t is peak transmit power, G is gain of the antenna, λ_0 is the radar wavelength, σ is the radar cross-section (RCS) of the target, $k = 1.38 \times 10^{-23}$ J/K is Boltzmann's constant, T_0 is the reference temperature, Δf is the radar bandwidth, and F is the receiver noise figure.

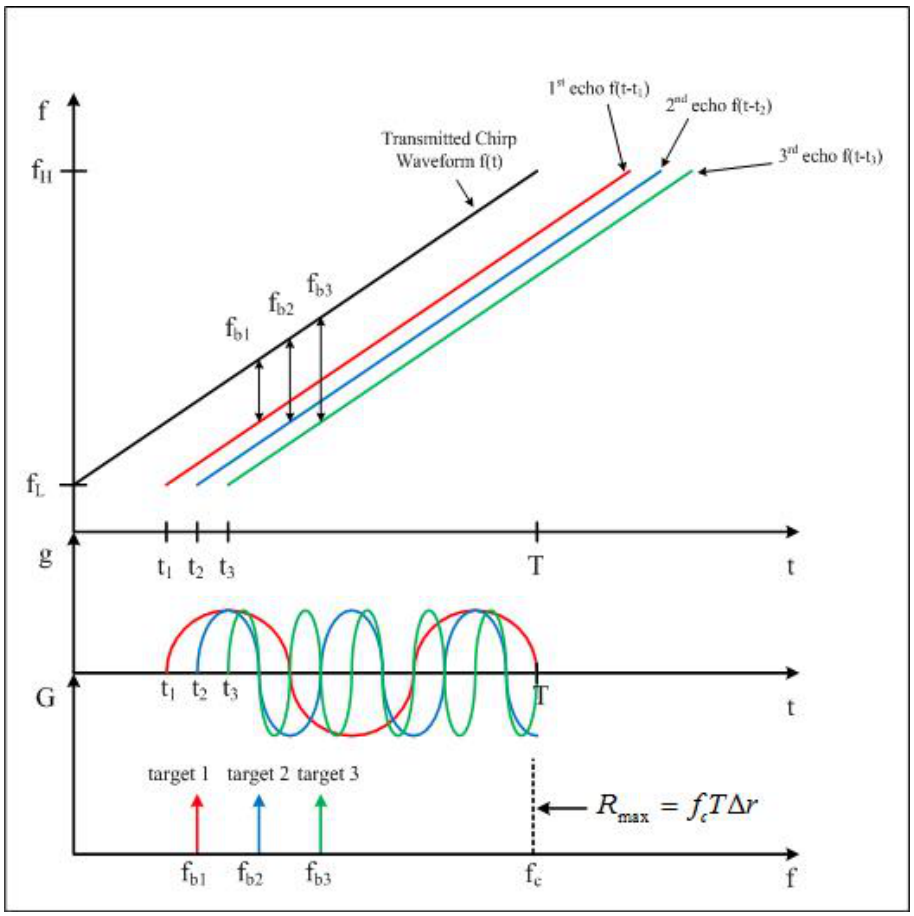

Figure 3.1. Frequency-Time Plot for Linear FM-CW Radar

FM-CW radar systems [16] operate similar to pulsed radars with the exception that the transmitted pulse is encoded in frequency, thus, requiring an additional decoding stage for the receiver. In order to fully understand FM-CW radar, it is sometimes helpful to illustrate the problem by using a frequency-time plot. Figure 3.1 describes a situation in which there are three distinct point-targets in view of the radar. The transmitted "sawtooth" waveform is a linear frequency modulated chirp with a pulse repetition time interval of T. Observing the first, second, and third echoes, we notice a corresponding return time, t_1, t_2, and t_3, and a downconverted "beat" frequency, f_{b1}, f_{b2}, and f_{b3}. The beat frequency of the n^{th} echo is given as,

$$f_{bn} = \frac{(f_H - f_L)t_n}{T} = \frac{2R_n\Delta f}{cT} = \frac{R_n}{T\Delta r} \tag{3.4}$$

where Δr represents the range resolution in an FM-CW radar system. Using (3.2), and letting $\tau = 1/\Delta f$, the range resolution of an FM-CW radar can be written as

$$\Delta r = \frac{c}{2\Delta f}. \tag{3.5}$$

The beat frequency is the spectral representation of range and is obtained by subtracting the received radar echo from the transmitted waveform. This is achieved in a hardware system using a mixer, amplifier, and filter. This configuration decodes our encoded waveform upon receive. The mixing of the transmitted waveform with the returning radar echo results in a sum and difference signal. A filter is required in order to select the desired difference signal while also setting the maximum range visible to the radar. The maximum range is set by two parameters. First, the cut-off frequency, f_c, of the "range" or anti-aliasing filter that follows the amplifiers, and second, the sample frequency, f_s, of the analog-to-digital converter (ADC). This is an important aspect of the decoding stage of the radar given the proportionality between range and frequency as seen from (3.4). Properly choosing the sampling rate

and filter cut-off frequency ensures successful data collection given the location of the radar. The maximum range, $R_{\max}$, of the FM-CW system can be expressed by rearranging terms in (3.4) where

$$R_{\max} = f_c T \Delta r = \frac{f_s T \Delta r}{2}. \tag{3.6}$$

The radar range equation for an FM-CW radar is written as

$$P_r = \frac{(T\Delta f) P_t G^2 {\lambda_0}^2 \sigma}{(4\pi)^3 R^4} \tag{3.7}$$

where $T\Delta f$ is the compression gain or time-bandwidth product of the system.

The advantages of using this type of radar system are its excellent range resolution, low peak-power, and increased sensitivity due to the ability to have a long integration time. Using (3.3), the sensitivity of an FM-CW radar can be expressed as

$$\text{SNR} = \frac{T\Delta f P_t G^2 {\lambda_0}^2 \sigma}{(4\pi)^3 R^4 k T_0 \Delta f F}. \tag{3.8}$$

The main disadvantage for a FM-CW radar systems is the isolation requirement between the transmitter and receiver, and that the target and instrument cannot move for the duration of the pulse. A conventional way to maintain a large isolation between the transmitter and receiver is to use separate antennas. This requirement reduces the complexity within the radar system; however, increases the overall cost through the additional antenna required. Furthermore, in spite of the isolation set by the distance separating the transmit and receive antenna, it is important, especially for CW radars, that the transmitter's peak power is set such that no harm is done to the receiver.

3.2 Data Processing

As discussed in Section 3.1, Fourier analysis of the received waveform is essential in FM-CW radar processing. The proportionality between range and frequency makes the use of a FFT[1] useful in sorting range data. The science data collected from the radar is acquired and stored using a data acquisition card, a peripheral device onboard a computer purchased from National Instrument (NI). Timing and control are accounted for using LabView in combination with other external devices including an arbitrary waveform generator, positioner, and 10MHz reference.

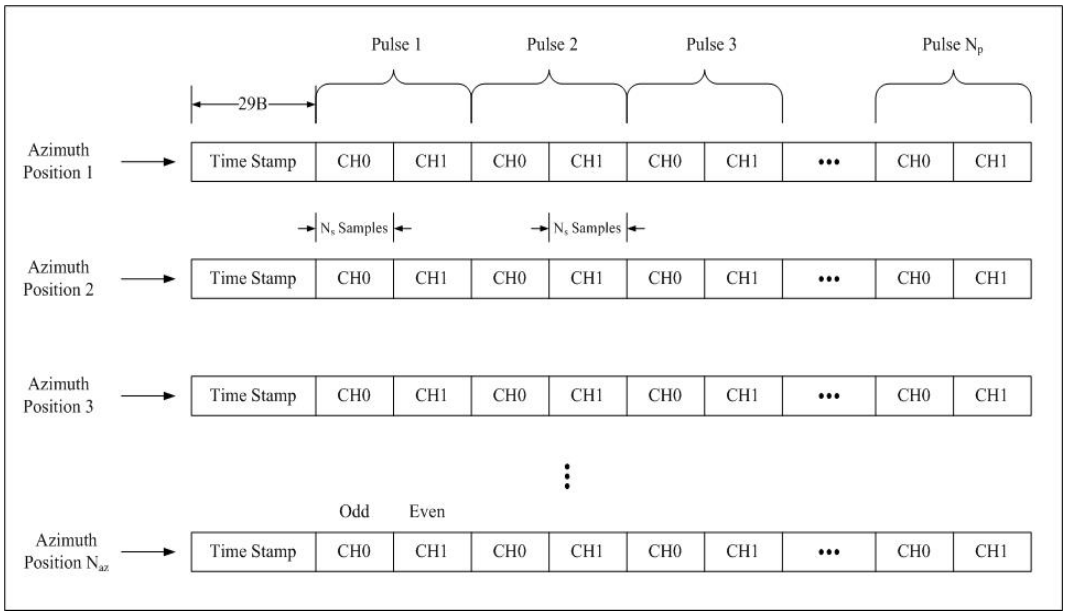

Figure 3.2. Radar Data Structure

Data is sampled by the ADC at a rate of f_s, assigning an upper limit of the maximum unambiguous frequency as $f_s/2$ with respect to the Nyquist sampling criterion. However, this setting, among others, can be adjusted to customize the radar for a variety of applications. For example, the maximum unambiguous range of the

[1]Fast-Fourier Transform.

radar can be adjusted by increasing or decreasing the sample frequency, f_s. The data acquisition parameters are listed in Table 3.1.

Parameters	**Description**
f_s	ADC sample rate (Hz)
N_s	Samples per pulse
N_p	Pulses per position
N_{az}	Scan size [degrees]
ΔN_{az}	Scan resolution [degrees per position]
$V_{pp,0}$	Scope range for ADC channel 0
$V_{pp,1}$	Scope range for ADC channel 1
T	Pulse duration
f_t	Trigger rate (Hz)

Table 3.1. Data Acquisition Parameters

Upon reception, the sampled waveforms are stored as binary files which are later read into MATLAB (Matrix Laboratory) for post-processing. Figure 3.2 illustrates how each binary file is structured. It is important to notice the effect of the data acquisition parameters, Table 3.1, on the storage mechanics. In Figure 3.2, a 29 byte timestamp is stored at the beginning of each position denoting the date and time while also providing information of the duration between adjacent data sets during the data collection. After the timestamp is stored, channel 0 and channel 1 voltage waveforms are collected from the analog-to-digital converter (ADC) and stored in an alternating fashion where the sampling window between adjacent pulses is controlled by an external trigger provided by the Tektronix arbitrary waveform generator. The trigger also keeps an account of all the pulses transmitted and received by the radar, providing the information needed to effectively control the QuickSet positioner. This basic flow of data repeats every new azimuth position. Thus, when referring to Figure 3.2, the storage flows from left-to-right and top-to-bottom.

Before any processing is performed, the timestamp at the beginning of each data set is removed. As previously established, the data format repeats every new position.

Following (2.2), the raw data is read into MATLAB in the form of a voltage matrix,

$$\mathbf{v}^{(q)} = \begin{pmatrix} v_{1,1} & v_{1,2} & \cdots & v_{1,2N_p} \\ v_{2,1} & v_{2,2} & \cdots & v_{2,2N_p} \\ \vdots & \vdots & \ddots & \vdots \\ v_{N_s,1} & v_{N_s,2} & \cdots & v_{N_s,2N_p} \end{pmatrix}^{(q)} . \tag{3.9}$$

Here channel 0 and channel 1 are acquired from the odd and even columns of the raw data matrix (3.9) which are expressed mathematically as $v_{m,2n-1}$ and $v_{m,2n}$ where $m = 1, 2, 3, \ldots, N_s$, $n = 1, 2, 3, \ldots, 2N_p$, and $q = 1, 2, 3, \ldots, \frac{N_{az}}{\Delta N_{az}}$. The parameters i, j, and q correspond to the time domain samples, pulses, and azimuth positions in (3.9). Table 3.1 provides a description of N_s, N_p, N_{az}, and ΔN_{az}. Before performing any spectral analysis on (3.9), the columns in raw data matrix are windowed with a Hann window function shown as

$$w_m = \frac{1 - \cos\left(\frac{2\pi i}{N_s - 1}\right)}{2}. \tag{3.10}$$

The Hann window function minimizes the effect of high frequency contributions at pulse edges which would otherwise distort and alias the desired signal. Once this is accomplished, the time domain signals measured from channel 0 (odd-pulse) and channel 1 (even-pulse) are converted into the frequency domain by

$$V^{(q)}_{k,2n-1} = \sum_{n=1}^{N_s} v^{(q)}_{m,2n-1} w_m \mathrm{e}^{-j\frac{2\pi}{N_s}(m-1)(k-1)} \quad (\text{channel } 0) \tag{3.11}$$

$$V^{(q)}_{k,2n} = \sum_{m=1}^{N_s} v^{(q)}_{m,2n} w_m \mathrm{e}^{-j\frac{2\pi}{N_s}(m-1)(k-1)} \quad (\text{channel } 1) \tag{3.12}$$

where the frequency domain index $k = 1, 2, 3, \ldots, \frac{N_s}{2}$ since only half of the spectral data is unique. By applying (3.11) and (3.12) to (2.2), the computational representation for an interferogram can be written as

$$\Gamma_k^{(q)} = \frac{\sum_{n=1}^{N_p} V_{k,2n}^{(q)} V_{k,2n-1}^{(q)*}}{\sqrt{\sum_{n=1}^{N_p} |V_{k,2n}^{(q)}|^2 \cdot \sum_{n=1}^{N_p} |V_{k,2n-1}^{(q)}|^2}}. \tag{3.13}$$

Since the correlation is independent of time and frequency, it becomes possible to proceed with (3.13) using MATLAB to perform the numerical processing.

As describe earlier, FM-CW radar is a pulse compression technique implemented by continuously transmitting a chirp waveform where upon reception a homodyne receiver architecture decodes the incoming radar echo into a collection of beat frequencies proportional to range. During post-processing, these beat frequencies or range bins are sorted by running the radar data through a FFT. In order to implement a FM-CW radar, the hardware supporting this operating mode has to be configured properly. Thus, a detailed description of the radar hardware is presented in the following chapter, providing substantial framework to the radar interferometer.

CHAPTER 4

RADAR SYSTEM HARDWARE DESCRIPTION

Modularity was an essential aspect to the development of the new Ku-band radar system. For that reason, it was decided to utilize as much of what already existed from past projects in terms of cables, power supply units, and data acquisition units. Furthermore, a 100MHz version of the 25MHz Ku-band dual-downconverter (Ku-DDC) served as the basis for developing a better working Ku-band radar interferometer. The basic layout of the radar system is illustrated in Figure 4.1. The transmitter and receiver hardware descriptions are presented along with a detailed description of the antenna design. The electrical and mechanical aspects of the radar system are also presented.

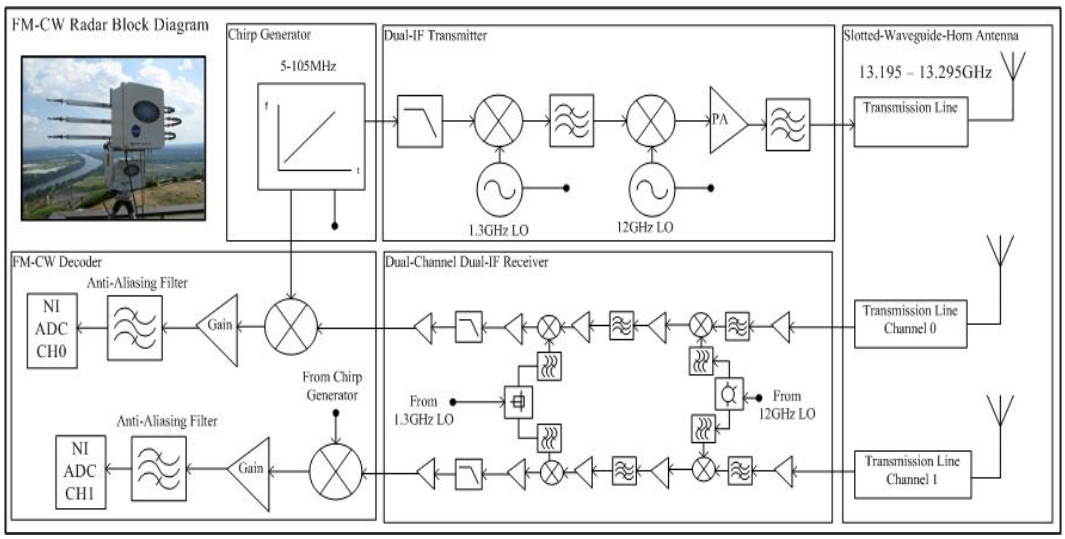

Figure 4.1. FM-CW Radar Block Diagram

Radar System Parameters	Value
Radar Type	FM-CW
Frequency	Ku
RF (Radio Frequency) Band	13.195-13.295GHz
IF (Intermediate Frequency) Band	1.195-1.295GHz
BB (baseband)	5-105MHz
RF Source	Solid State
Radar bandwidth	100MHz
Range resolution	1.5m
Polarization	Single (VV)
Peak Power	100mW (capable of 2W)
Waveform	Linear FM Chirp
Antenna	Slotted-waveguide-horn

Table 4.1. Instrument Parameters

4.1 Receiver

The Ku-band receiver is a three-stage, dual-channel microwave receiver consisting of a dual-IF receiver and FM decoder. The dual-IF receiver consists of a Ku-band to L-band downconversion stage and a L-band to baseband downconversion stage constructed on two microwave printed circuit boards, one board for each stage. A dual-IF architecture is favorable because of the amount of image rejection obtained as a result. The FM-CW decoder stage takes the downconverted signal from the dual-IF receiver and converts it into a usable waveform that is digitized and stored by a National Instrument data acquisition unit. This stage is constructed from connectorized components with 50Ω characteristic impedance. In this section, a detailed description of the Ku-band to L-band downconverter is given where as only a brief description of the L-band to baseband downconverter is presented. A hardware description of the FM-CW decoder and data acquisition unit are also present. Table 4.1 provides details on some of the key system parameters.

4.1.1 Ku-band to L-band Downconverter

The first stage in the radar receiver is the Ku-band to L-band downconverter depicted in Figure 4.2. It is powered through a ribbon cable fed from the L-band to baseband downconverter board. The RF is fed from the antenna assembly to the first stage in the receiver via rectangular waveguides and low loss SMA cables. The efficiency of the feed network is important since the presence of loss before the first amplifier adds to the overall noise figure in the receiver. Measurements of noise figure are presented in Chapter 5. From the feed, the signal arrives at the receiver through low loss SMA cables which are adapted to 2.4mm in order to connect with a pair of Southwest 2.4mm end-launch connectors, illustrated in Figure B.2 of Appendix B. Upon leaving the connectors, a Hittite HMC516 20dB low noise amplifier (LNA) sets the noise figure for each channel in the receiver. Edge-coupled filters can be seen at the output of each LNA, selecting the desired RF band while setting the initial bandwidth of the receiver. The RF filters have an insertion loss of -4.5dB and a bandwidth of 810MHz centered at 13.24GHz, hence, the 100MHz radar bandwidth is established by subsequent filtering in the L-band to baseband downconverter. Appendix B describes the analysis of edge-coupled filters at Ka-band using measured data and simulations. At the filter output are Hittite HMC521 image-reject mixer with a conversion loss of 8dB. This particular mixer suppresses the undesired image band while also performing the downconversion from Ku-band to L-band. Image rejection performance is discussed in Chapter 5. The downconversion is enabled by a +10dBm Luff Research 12GHz local oscillator or LO. The LO connects to the receiver via a 2.4mm end-launch connector, and is amplified by a Hittite HMC490 27dB amplifier. The amplifier is crucial in this case because of the +15dBm requirement at the LO port of the mixers. A "rat-race" power splitter also known as a 180^o hybrid splitter delivers the LO to each channel in the receiver, branching into subsequent edge-coupled filters that provide rejection against RF leakage between the adjacent

channels. The LO filter have an insertion loss of -4.8dB and a bandwidth of 650MHz centered at 12GHz. These filters are important not only for their ability to pass the LO but also for their ability to suppress the RF, hence acting as an electrical barrier between each channel. Channel isolation measurements are presented in Chapter 5. After downconverting from Ku-band to L-band, the L-band signal arrives at the input of the second stage in the receiver through a coaxial jumper cable and SMA end-launch connector.

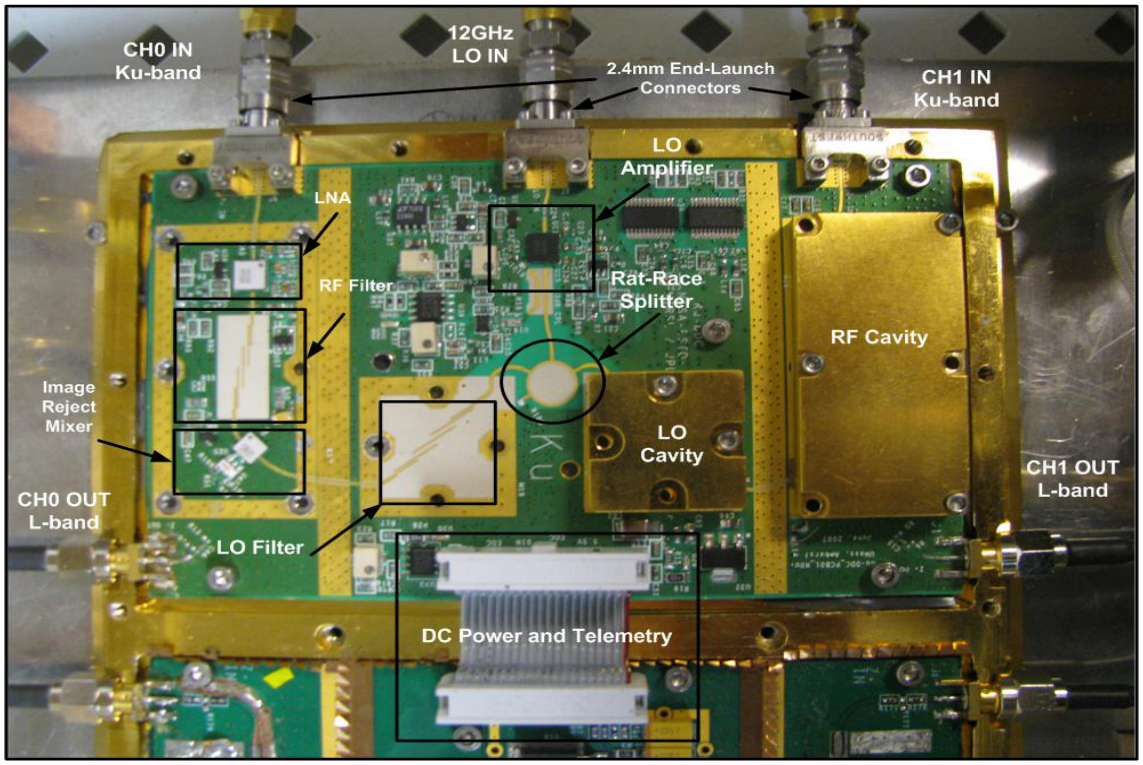

Figure 4.2. Picture of the Ku-band to L-band downconverter PCB.

4.1.2 L-band to Baseband Downconverter

The second stage in the receiver is the L-band to baseband downconverter. It is powered by an external 15V source that regulates power for all the active components on both boards. For this stage in the receiver, a +17dBm Luff Research 1.3GHz LO provides the necessary means for downconversion from L-band to baseband. For a

detailed description of the L-band to baseband downconverter, the reader is encouraged to refer to [18] since the hardware is identical to that of the Ka-band radar interferometer.

4.1.3 FM-CW Decoder

The third stage in the receiver is the FM-CW decoder depicted in Figure 4.3. As described in Section 3.1, the FM-CW decoder stage converts the baseband output of the Ku-DDC into a difference frequency. The difference frequency, or beat frequency, f_b, is a spectral representation of range, obtained by mixing the transmit chirp with the downconverted chirp echo. In order to successfully produce a beat frequency, the transmit power at the mixer should be between +7dBm and +10dBm exceeding the power level of the chirp echo. Once decoded, the beat frequency is amplified by a pair of Minicircuit ZFL-500 20dB amplifiers. This amplification ensures that the beat signal falls within the dynamic range of the ADC on the National Instrument computer. A 870kHz anti-aliasing filter sets the maximum range of the radar, eliminating any data contamination from aliasing that could appear in band upon digitization. A 5MHz low-pass filter is strategically placed after the anti-aliasing filters to ensure any baseband leakage and spurious signals that may exist at this point in the decoding process are sufficiently suppressed.

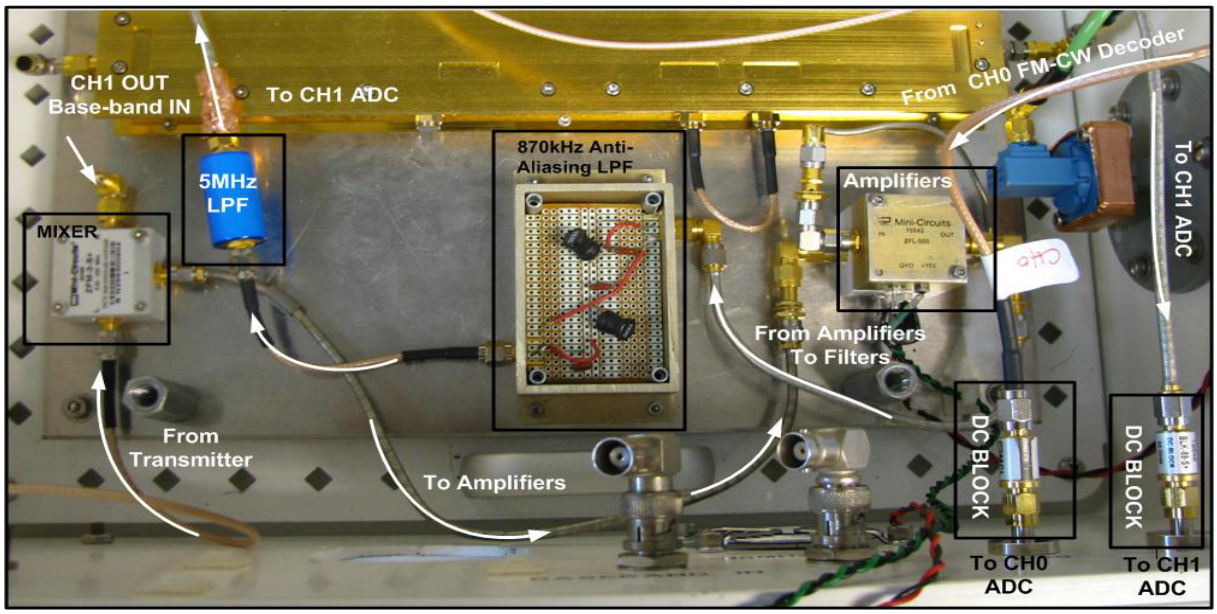

Figure 4.3. Picture of the FM-CW decoder circuit.

4.1.4 Data Acquistion Unit

The data acquisition unit used in [19] was comprised of a Hewlett Packard (HP) 8022C vector network analyzer connected via a MATLAB user interface. This method proved to be cumbersome and unreliable because of inherent phase problems when using the network analyzer for interferometry. Luckily, similarities in the baseband signal helped assimilate the new Ku-band radar system with another data acquisition unit which was incorporated into the Ka-band radar interferometer [18]. The current data acquisition unit consisted of a National Instrument, NI PXIe-1062Q, computer system capable of sampling and storing data in real-time to a 1TB RAID[1]. A LabView program, developed by Michael Shusta and Mandy Liem, served as the primary software tool during data collection. As described in Section 3.2, data is collected on the channel 0 and channel 1 ports of the National Instrument ADC. Timing and

[1]Redundant Array of Independent Disks.

control are controlled by an input trigger supplied by the transmit waveform generator. Details on data processing can be found in Section 3.2. The option to timestamp each position with GPS[2] coordinates was also available via an external AC12 Magellan GPS receiver controlled through LabView. This option was rarely implemented however since the same information could be obtained from sources such as Google Earth.

4.2 Transmitter

In the same way as the receiver, upconversion is performed in two steps, first, from baseband to L-band and, second, from L-band to Ku-band. Due to the complexity and design time of a PCB, the transmitter was developed using 50Ω connectorized components, allowing a prototype to be constructed within a short period of time. In this section, a hardware description of the two chirp generators is given along with a description of the hardware that comprises the upconverter.

4.2.1 Tektronix Waveform Generator

A Tektronix AFG3252 Dual Channel Arbitrary/Function Generator was the primary waveform generator in the radar system. The waveform generator's versatility is shown in its ability to produce sine, square, and chirp waveforms via an easily navigable user interface. For the purpose of FM-CW radar, a linear FM chirp was used. The chirp waveform was created through the Tektronix frequency sweep function. The sweep parameters are shown in Table 4.2. These values are entered into the device using a push-button interface located on the face of the instrument. The waveform was fed from the generator via a 72 inch BNC cable to the baseband input of the radar. A trigger output port on the Tektronix connects to the trigger input on

[2]Global Positioning System

the National Instrument ADC providing the necessary timing and feedback control for the data acquisition unit.

Sweep Parameters	**Value**
Amplitude	$4V_{pp}$ (+16dBm)
Start Frequency	5MHz
Stop Frequency	105MHz
Sweep Time	4ms
Hold Time	0ms
Return Time	0ms
Trigger Interval	4ms
Type	Linear
Mode	Repeat
Source	Internal

Table 4.2. Tektronix Sweep Parameters

4.2.2 Agilent Arbitrary Waveform Generator

The Agilent N8241A Arbitrary Waveform Generator (AWG) was procured to serve as the replacement to the Tektronix instrument since the method in which Tektronix creates the chirp waveform is thought to be reducing the range resolution in the far range because of non-linearities in the waveforms phase. The Agilent waveform generator uses a 1.25GHz sample clock with 10-bits of resolution. Communication with the Agilent AWG is done using the N8241A Control Utility leaving the user with a less useful interface in comparison to the Tektronix instrument. Unlike the Tektronix instrument, waveforms are defined in MATLAB by the user. Once defined, the waveform is saved in a binary format recognizable by the N8241A Control Utility. An external amplifier is required for applications above $500mV_{pp}$ due to the lack of internal amplification. Hence, a Teledyne AC238 32dB amplifier with a 1dB compression gain of approximately +16dBm was used for external amplification.

4.2.3 Ku-band Dual-IF Upconverter

In the same way as the receiver, the transmitter performs upconversion in two stages. First, a linear FM chirp is provided to the input of the radar by one of two devices either from the Tektronix waveform generator or the Agilent arbitrary waveform generator. The waveform is filtered through a 120MHz low-pass filter, thus passing only the desired baseband signal e.g. 5MHz to 105MHz. After being filtered, a splitter divides the baseband signal for transmission and reception. In order to account for the power division losses, a +16dBm chirp waveform is required at the radar input. This provides enough LO drive to both channels in the decoder stage while also providing sufficient power upon transmission. A 20dB attenuator was placed before the first mixing stage in order to set the eventual transmit power to a peak level of approximately 100mW (+20dBm). Upconversion from baseband to L-band is performed with a Teledyne MC1502 double-balanced mixer with a conversion gain of -6dB. A 1.3GHz Luff Research LO provides the LO drive of +7dBm while a Lorch Microwave ceramic band-pass filter selects the band between 1.195GHz and 1.295GHz. The subsequent conversion from L-band to Ku-band utilizes a Marki Microwave double-balanced mixer with a conversion gain of -5dB. A 12GHz Luff Research LO provides the +7dBm LO drive while a Teledyne band-pass filter selects the band between 13.195GHz and 13.295GHz. Once at Ku-band, a Cernex 40dB solid-state power amplifier (PA) boosts the signal to the desired 100mW level. Having a 1dB compression point at +33dBm, the PA allowing for a potential operating power of up to 2W. After amplification, the transmit waveform travels through a coaxial transmission line and a waveguide bulk head connector to the transmit antenna. As a note to the reader, it is important to recognize the proximity of the transmit antenna to the receive antennas, and how the amount of the leakage from the transmitter may consequently saturate the receiver. If the receiver can only tolerate a maximum input power level of +5dBm and the transmitter peak power level does not exceed +33dBm,

then up to a 28dB coupling factor can be tolerated between the transmit and receive antennas. Measured coupling between the transmitter and receiver indicate that the couple factor is actually much higher than 28dB, alleviating any doubt that the receiver performance would degrade for peak power levels at +20dBm.

4.3 Antenna

A Ku-band corporate-fed patch array antenna was used in a previous Ku-band radar interferometer [19]. This antenna benefited from it's low cost, light weight, and high bandwidth, but lacked in efficiency and sturdiness. Due to the losses in the feed structure the receiver noise figure suffered, thus making an antenna with better efficiency more desirable.

A resonant slotted waveguide-horn antenna showed considerable potential with it's prior success in the Ka-band radar interferometer [18]. Its simplistic design, sturdiness, and high efficiency outweighed a potentially higher cost caused by high machining tolerances and the possible need for multiple prototyping. As a result, cost and strict matching requirements necessitated careful design. In the following, a detailed description of antenna design methodology is provided, including analytic formulation and computer simulation. Table 4.3 provides antenna specifications that were important factors in the design.

θ_{3dB}	45^o	Half-power elevation beamwidth
ϕ_{3dB}	1^o	Half-power azimuthal beamwidth
BW	100MHz	Antenna bandwidth
SLL	13dB	Uniform aperture illumination
D_0	29.6dB	Estimated directivity, $\frac{41{,}253}{\theta_{3dB}\phi_{3dB}}$
f_c	13.245GHz	Antenna center frequency

Table 4.3. Antenna Specifications

4.3.1 Linear End-Fed Slotted Waveguide Array

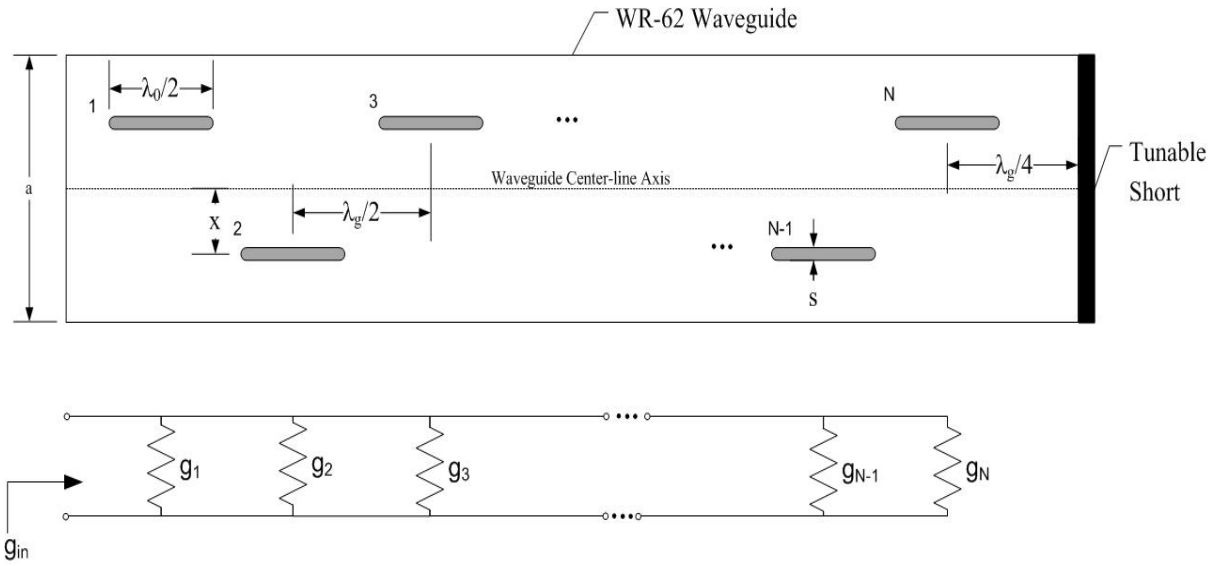

Figure 4.4. Illustration of the slotted waveguide with equivalent circuit model

The slotted waveguide array antenna is easily fabricated since it requires only precision milling of slots on the rectangular waveguides broad-wall. However, attention to slot configuration, spacing, and dimensioning along with waveguide loading, feeding, and dimensioning is a significant part of the design process. Figure 4.4 presents an illustration of the slotted waveguide array, describing some of the variables which characterize the antenna and influence it's performance.

The positioning of slot elements are along the length of the waveguide, making machining uncomplicated. Slot separation, length, and offset are dimensions which are used to tune the antenna to the desired frequency range.

The process of design begins by choosing a slot separation of $\lambda_g/2$, thus creating a 180^o phase difference between adjacent slots. By alternating slot displacement off the center-line axis while still maintaining $\lambda_g/2$ separation, the phasing across the array remains constant, keeping the main beam at broadside. The slots alternating pattern

can be best understood through the modeling of surface currents in a rectangular waveguide, as described in Section A.2.

Next, a slot length, l_s, is chosen to be resonant, $\lambda_0/2$. As a result, the resonant length in combination with the longitudinal slot configuration allows for the simplification of the physical model to a circuit model of shunt resistors. In Figure 4.4, the antenna is loaded with an electrical open, spaced $\lambda_g/4$ away from the last slot; this creates a standing wave in the array further ensuring proper matching and broadside radiation.

Finally, the resonant slot offset from the center-line (Figure 4.4), x, is used to determine the normalized[3] conductance at each slot using the following equation,

$$g_0 = 2.09\frac{a}{b}\frac{\lambda_g}{\lambda_0}\cos^2\left(\frac{\pi}{2}\frac{\lambda_0}{\lambda_g}\right)\sin^2\left(\frac{\pi x}{a}\right) \tag{4.1}$$

Equation (4.1) is giving by Stevenson [17], where a and b are the inner dimensions of WR-62 Ku-Band waveguide and λ_g and λ_0 are the dominant mode waveguide and free-space wavelengths. Equation (4.1) is compared with computer simulations and discussed in Section 4.3.4. The normalized input conductance of the antenna is written as

$$g_{\text{in}} = \sum_{n=1}^{N} g_n = 1, \tag{4.2}$$

where N is the total number of slot elements in the array. A uniformly illuminated array aperture simplifies (4.2) to the following,

$$g_{\text{in}} = Ng_0 = 1. \tag{4.3}$$

Equation (4.3) indicates that the conductance at each slot should be inversely proportional to the total number of slot elements in the array; hence, $g_0 = 1/N$. Referring

[3]Normalized to the waveguide characteristic conductance, G_0.

to Table 4.3, an N-element array is required in order to satisfy $\phi_{3dB} = 1^o$ where N is determined, first, by approximating the element pattern of a slot with that of a magnetic dipole,

$$F(\phi) = \frac{\left[\cos(\frac{kl_s}{2}\cos(\phi)) - \cos(\frac{kl_s}{2})\right]}{\sin(\phi)}, \tag{4.4}$$

where l_s is the length of the slot or magnetic dipole, k is the free-space wavenumber, and ϕ is the angle from broadside in the direction of the array axis in the far-field.

A uniformly weighted and normalized array factor is defined as the following,

$$AF(\phi) = \frac{1}{N}\frac{\sin(\frac{N}{2}kd\cos(\phi))}{\sin(\frac{kd}{2}\cos(\phi))}, \tag{4.5}$$

where N is the number of elements in the linear array and d is the spacing between each element, recall $d = \lambda_g/2$. By multiplying (4.4) and (4.5), the radiation pattern of the slot array can be written as,

$$E_(\phi) = F(\phi)AF(\phi). \tag{4.6}$$

From (4.6), it becomes possible to determine what N is needed to obtain $\phi_{3dB} = 1^o$. For this case, a 70-element array was chosen. Using (4.3), $g_0 = 1/70 \approx 0.014$, thus providing a good approximation for single-slot conductance.

4.3.2 Parallel-Plate Feed Structure

The design of the parallel-plate feed structure is constrained by the separation, d, and height, h, of the parallel-plates. The height is chosen to be one free-space wavelength, λ_0, ensuring that the only the dominant mode, TE_0, is supported. The separation is chosen to be $d = \frac{2}{5}\lambda_0$; this, satisfies the relation developed by Gruenberg

[7], where the normalized conductance of resonant waveguide slots radiating into an infinite parallel-plate section can be characterized by,

$$g = 2.75\frac{dg_0}{\lambda_0} \quad \text{for} \quad d < \lambda_0/2. \tag{4.7}$$

4.3.3 E-Sectoral Horn

A standard slotted waveguide array has high gain in azimuth but low gain in elevation. For the purpose of creating a topographic map of ground terrain, a 45^o beamwidth is desired (4.3). Hence, additional gain in elevation can be achieved by shaping the beam using a E-plane sectoral horn. Designing this horn section of the antenna requires an understanding of how the horn dimensions correspond with the matching and beamwidth of the antenna. To understand the impedance matching better, a wedge geometry was used to approximate the internal structure of the horn. This approximation is useful because field solutions to the wedge exist in most electromagnetic textbooks [9]. These field solutions are used to approximate for the horns characteristic impedance, $Z^{\mathrm{TE}_0}(\rho)$ where ρ is the radial dimension from the horn's throat to the horn's aperture. Section A.1 provides a detailed derivation of $Z^{\mathrm{TE}_0}(\rho)$.

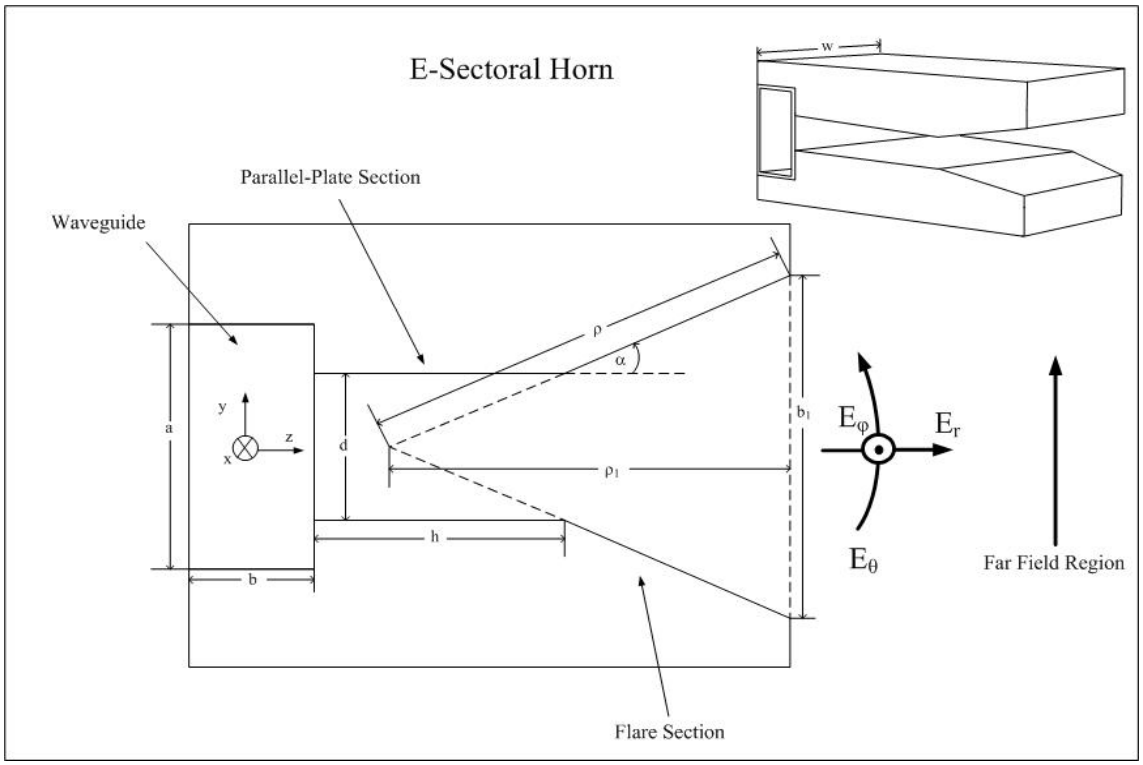

Figure 4.5. E-plane sectoral horn.

Referring to (A.5), it is shown that the impedance of the horn depends on the radial distance, ρ. By minimizing the amount of reflected energy between the horn and the air surrounding the antenna, it becomes possible to determine the value for ρ. The return-loss equation [12] that gives the reflection coefficient looking out of the horn section using the horn's aperture as the reference plane is written as

$$\Gamma_{\text{air}}(\rho) = \frac{120\pi - Z^{\text{TE}_0}(\rho)}{120\pi + Z^{\text{TE}_0}(\rho)}. \tag{4.8}$$

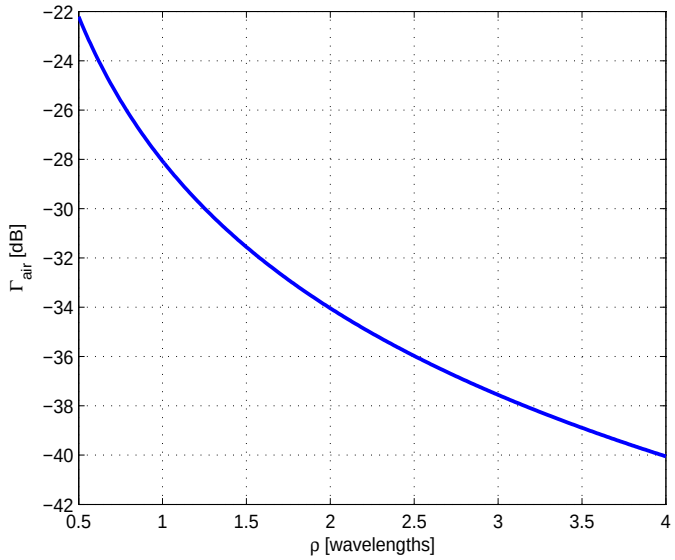

Figure 4.6. Γ_{air} versus ρ

Figure 4.6 is a plot of (4.8) with respect to ρ. Balancing the options of the horn's physical size with the matching characteristics gives the design curve shown in Figure 4.6 from which the radial distance, ρ, was chosen to be $1.5\lambda_0$. Once the matching criterion was fulfilled, it became possible to focus on the beamwidth specification. In order to satisfy beamwidth requirements, the far-field approximation for an E-plane sectoral horn antenna was used. This approximation can be found in most antenna handbooks [1].

Using Figure 4.5 as a reference for the actual physical geometry, the equations that represent the analytical formulation of the electric field in the far-field region are

$$\bar{E} = \hat{\theta} K_1 \frac{\mathrm{e}^{-j(k(r-r_1)-\frac{\pi}{2})}}{r} \left[1 + \cos(\theta)\right] F(t_1^{'}, t_2^{'}) \tag{4.9}$$

$$K_1 = \frac{w\sqrt{\pi k \rho_1} E_y}{2\pi^2} \tag{4.10}$$

$$r_1 = \rho_1 \sin^2(\theta/2) \tag{4.11}$$

$$F(t_1^{'}, t_2^{'}) = \left[C(t_2^{'}) - C(t_1^{'})\right] - j\left[S(t_2^{'}) - S(t_1^{'})\right] \tag{4.12}$$

$$t_1^{'} = \sqrt{\frac{k}{\pi\rho_1}}\left(-\frac{b_1}{2} - \rho_1 \sin(\theta)\right) \tag{4.13}$$

$$t_2^{'} = \sqrt{\frac{k}{\pi\rho_1}}\left(+\frac{b_1}{2} - \rho_1 \sin(\theta)\right) \tag{4.14}$$

where E_y represents the magnitude of the y-polarized electric field inside the horn structure, $b_1 = 2\rho\sin(\alpha)$ is the dimension of the mouth opening, and $\rho_1 = \rho\cos(\alpha)$ is the distance from the throat to the mouth of the horn section. Using the above equations it is determined that $\alpha \approx 22^o$ forms a pattern where $\theta_{3dB} = 45^o$.

4.3.4 Computer Simulations

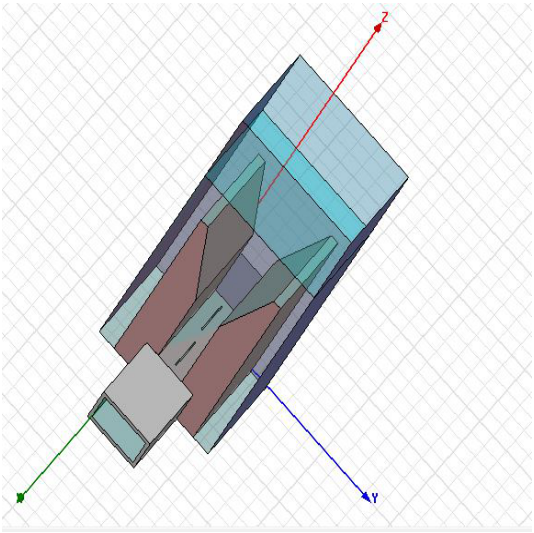

Figure 4.7. Single antenna cell modeled in Ansoft HFSS.

To move the antenna design beyond the theoretical treatment described thus far, the antenna structure was modeled and simulated in the frequency domain using the Ansoft HFSS[4] software package. Figure 4.7 illustrates the model used to represent the

[4]High Frequency Structure Simulator

physical antenna structure. Because the computer resources to model and simulate the entire 70-element finite antenna array would be immense, infinite array theory to employing a single cell model with periodic boundary conditions was used. Parametric sweep simulations on this model for various slot lengths, l_s, and offsets, x, were used to optimize the values of slot impedance. This technique was adopted from Elliot's analytical approach in determining the correct resonant length and slot offset [4]. Figure 4.8 shows the normalized conductance, G/G_0, and susceptance, B/G_0, as a function of slot length for fixed values of slot offset. The required slot length is approximated by comparing the normalized slot conductance values with the value obtained from (4.3) in which $G/G_0 = g_0 \approx 0.014$. From Figure 4.8, it was determined that $l_s = 443$ mil (1.12522 cm) for $x = 19.8$ mil (0.50292 mm) would work best. To go one step further, HFSS was then used to check the validity of (4.1) and (4.7). Figure 4.8 shows good agreement between Gruenberg's approximation and computer simulations. Notice that the HFSS approximation of slot conductance begins to deviate from analytical formulations as B/G_0 becomes non-zero.

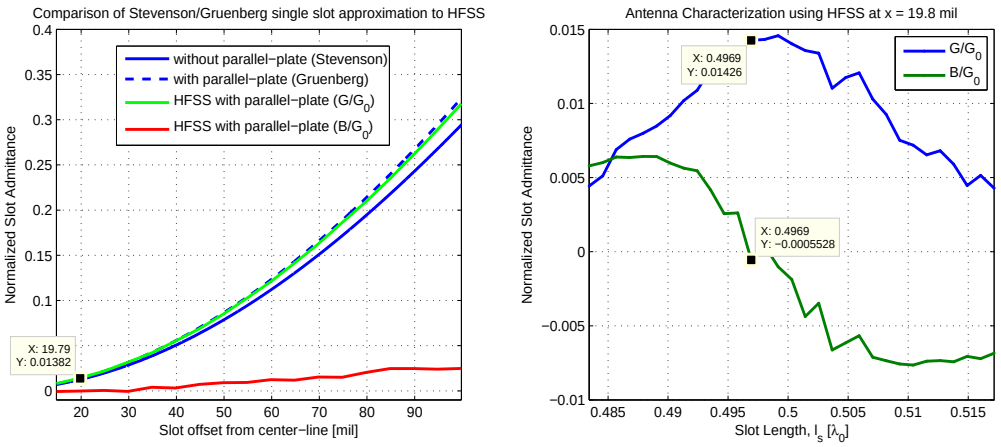

Figure 4.8. Single slot approximation (left) and HFSS Simulation (right).

4.3.5 Antenna Mounting, Configuration, and Fabrication

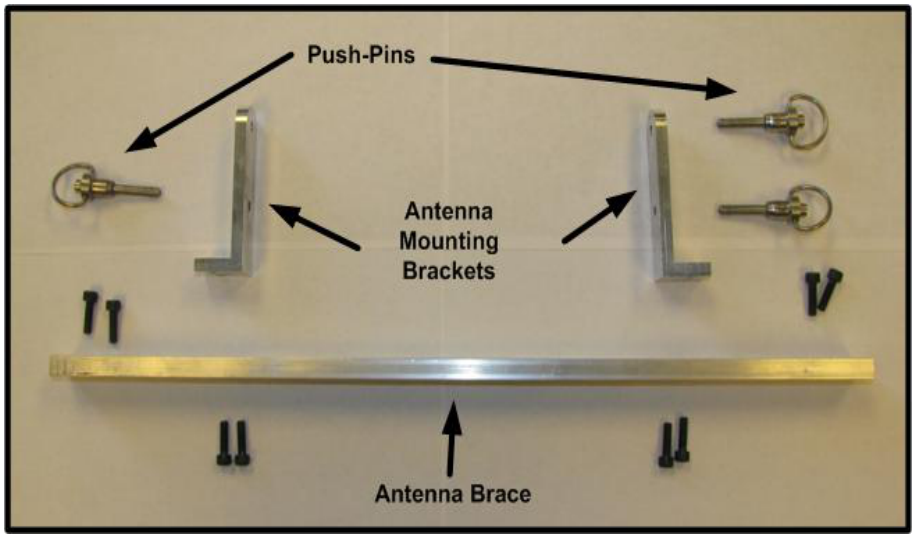

Figure 4.9. Antenna Mounting Bracer.

The antenna mount was designed for the Ka-band slotted-waveguide antennas and was built in such a way that the heavier, larger Ku-band slotted waveguide antennas could be retrofitted to the existing mount. As a result, antenna mounting braces were fabricated to be used with the existing structure, providing the support needed. It was important to make these special bracers in order to prevent bowing along the length of the antenna which could result in an undesirable change in the antennas radiation pattern. An exploded view of the antenna brace is illustrated in Figure 4.9. The antennas are supported through special antenna brackets via three metal push-pins which fit into holes spaced along three vertical support beams. Each beam consists of 16 holes spaced 20mm apart allowing for a maximum baseline separation of 30cm. In the current antenna configuration, the two receive antennas are separated by 28cm while the transmit antenna lies in the middle between the two receive antennas. Although the system was designed for variability and versatility, hardware configuration is limited in terms of antenna placement. For that reason, the feed from antenna assembly to the radar box will require longer flexible waveguides

as well as a larger, more capable antenna mount in order to accommodate various baseline separations. Refer to [18] for a detailed description of the antenna mount.

Antenna fabrication[5] was started by first, acquiring the necessary raw materials for the horn and array. These materials included an aluminum block and three 50 inch long aluminum straight-section waveguides[6]. The antennas were fabricated through an automated process where machining tolerances were limited to be within 0.1 mil, requiring all design dimensions to be within this limitation. Appendix C provides the final antenna design plans as well as an exploded view of the antenna after fabrication.

4.4 Power Distribution

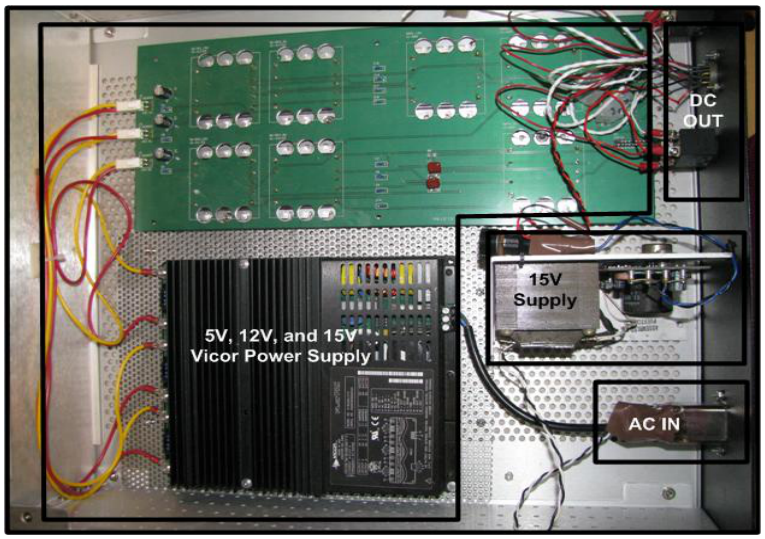

Figure 4.10. Radar Power Supply Unit.

There are two power supply units that power the radar and positioner. One of the two power supply units was reused from the previous Ka-band radar interferometer

[5]Supervised by Jim Bernotas of Amherst Machine Shop located in Amherst, MA.

[6]Purchased from Flann Microwave.

which mainly supplies 24V to a QuickSet positioner while also providing a 10MHz reference oscillator for synchronizing the entire radar system. The other power supply unit was taken from the Ku-band radar interferometer [19] consisting of a 15V power supply at 3A and Vicor power unit supplying three voltage channels rated for 15V, 12V, and 5V at 2.1A each. The Vicor unit supplies power to the Ku-DDC and the two solid state local oscillators. The extra 15V supply was added in order to provide enough current to the power amplifier described in Section 4.2.3. Cross-talk between components in the radar was prevented by isolating the biasing circuitry, while voltage ripple was maintained by adding Vicor ripple attenuator modules (RAM) to the biasing network. This power configuration was necessary in that it helped remove some of the striping effects in the FM-CW imagery due to various oscillating signals riding on the various power supplies of the interferometer's active components. Section 6.4 provides a detailed explanation of the debugging process that was used to detect these oscillating signals, as well as the hardware modifications put in place as a response to these problems. Figure 4.10 shows a photograph of the primary power supply for the radar.

4.5 Positioner

The positioner is a QuickSet integrated controller fixed-mounted to a tripod with telescoping legs. The positioner is capable of scanning in azimuth and elevation. However, the elevation scan remains unused due to large swath coverage in elevation provided by the antenna. The positioner is controlled through a LabView program on board the National Instrument computer. The control signals generated by LabView are sent to the positioner via a serial cable connecting the National Instrument and positioner. The serial controls and power are wired through a military connector that mates with a military socket at the base of the positioner. Figure 4.11 presents a photograph of the Quickset positioner, highlighting some of the important features.

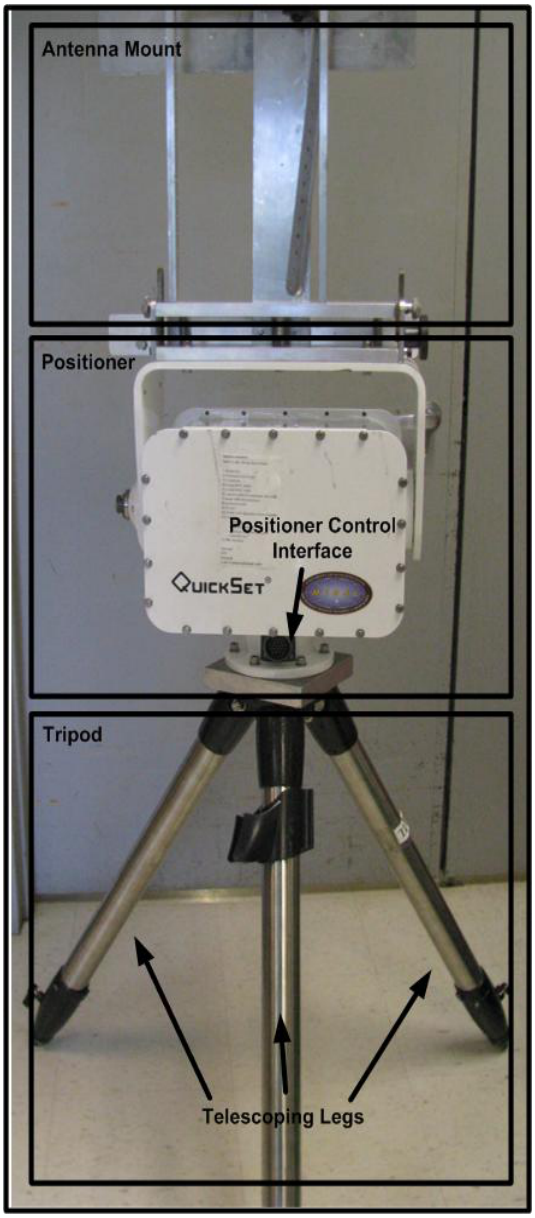

Figure 4.11. A photograph of the Quickset positioner, tripod, and antenna/radar mount.

The hardware descriptions presented in this chapter illustrate the components that comprise the FM-CW radar. However, hardware description alone does not present a complete description of the radar hardware. For that reason, metrics such as gain, isolation, noise figure, and linearity are useful when evaluating the performance of

the radar hardware. In the following chapter, a concise look into the radar hardware performance is presented, providing measurable data highlighting the capabilities and limitations of the instrument.

CHAPTER 5

RADAR SYSTEM HARDWARE EVALUATION

In this chapter, a comprehensive evaluation of the radar system hardware is presented, providing measurement results of the receiver, transmitter, and antennas in terms of performance metrics such as return loss, gain, isolation, noise figure, linearity, and peak power.

5.1 Ku-Band Dual-Channel Dual-IF Downconverter

5.1.1 Return Loss Measurement

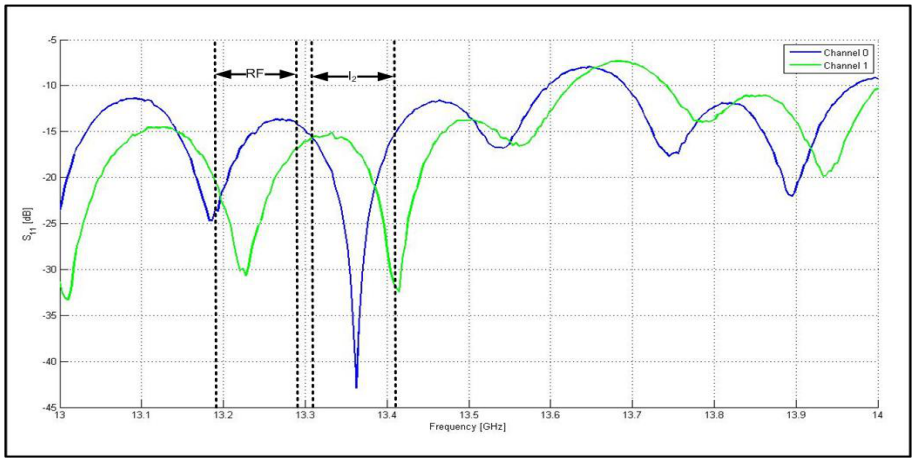

Figure 5.1. Ku-DDC Input Return Loss

The receiver return loss, S_{11}, was measured at the waveguide-feed interface immediately before the receiver antenna using a HP8722C vector network analyzer, calibrated at a power level of -30dBm. The return loss is an important metric because of it's ability to show how well-matched the system is over the radar bandwidth.

Figure 5.1 shows the matching performance for both channels in the receiver, emphasizing the performance over the radar bandwidth, RF, and image bandwidth, I_2. The S_{11} measurement observed at these frequencies is below -10dB, indicating a good impedance match over the radar and image bandwidths. It is important to take notice of the matching at the image band due it's close proximity to the desired RF band, see Section 5.1.5. The matching performance can be attributed to the design of the transmission lines inside the PCB as well as the pin-placement of the end-launch connector. An end-launch connector with proper pin-placement is depicted in Figure B.2 of Appendix B.

5.1.2 Receiver Gain Measurements

The gain performance of the receiver is described in this section. It is defined as a ratio of output power delivered to the load and the available power at the input of the receiver. The following equation describes this relationship,

$$G = \frac{P_L}{P_{in}} \tag{5.1}$$

where P_{in} was the power supplied at the input of the receiver board using a Rohde & Schwarz signal generator and P_L was the power measured at the output of the receiver board using an Agilent Power Spectrum Analyzer. This measurement was made for each channel and subsequent stages in the receiver except for the FM decoding stage. Gain measurement results are shown in Figures 5.2 and 5.3. Analysis of Figure 5.2 shows that for both channel 0 and channel 1, the gain response is fairly flat over the radar bandwidth; however, upon further examination, the gain response of channel 1 is approximately 5dB lower than that of channel 0. In order to explain this gain difference, it is important to realize the inherent problems with PCB design to tolerances during fabrication and imperfections from human error during design. The source of this gain difference potentially stems from an insufficient supply of LO

power to channel 1 resulting in poor conversion gain from the mixer. An asymmetric split in power along the LO distribution could also explain the gain difference between channel 0 and channel 1. Another explanation to this problem comes from the manner in which the HMC521 image-reject mixer is oriented on the side of channel 1. Since this mixer is a prepackage component, the LO, IF, and RF ports have asymmetric qualities when placed side-by-side. Hence, placement of this component causes the LO and RF ports to be swapped and repurposed for channel 1. Luckily, for this particular mixer, the LO and RF share the same bandwidth, hence, the resulting downconversion from Ku-band to L-band remain unaffected as long as the LO drive at the RF port is larger than the RF drive at the LO port.

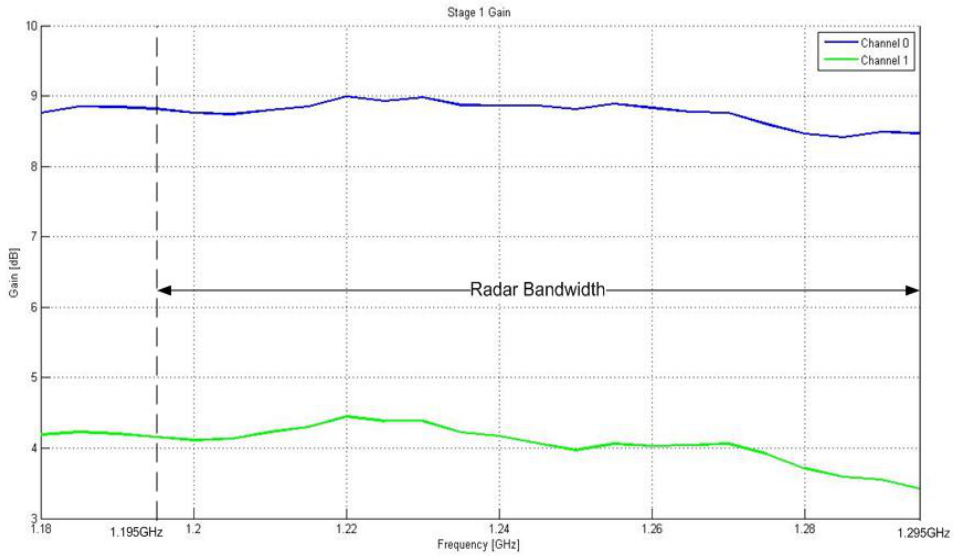

Figure 5.2. Ku-band to L-band Downconverter Gain Measurement

The gain measurement shown in Figure 5.3 shows a large difference in gain when compared to Figure 5.2. It is important to understand that receiver was originally developed for a airborne/spaceborne platform in which a pulsed radar was envisioned. As a consequence, a pulsed radar would require a large amount of gain to increase

sensitivity. Since the radar is being implemented as a FM-CW radar, the gain required at this stage of the receiver is unnecessary. Further analysis of Figure 5.3 shows that channel 1 has fairly good gain flatness over the radar bandwidth, while channel 0 shows a 10dB gain difference at the 5MHz band edge suggesting a problem with one of the baseband amplifiers. Figure 5.4 shows the total gain measured for the Ku-DDC, essentially, the combination of Figures 5.2 and 5.3.

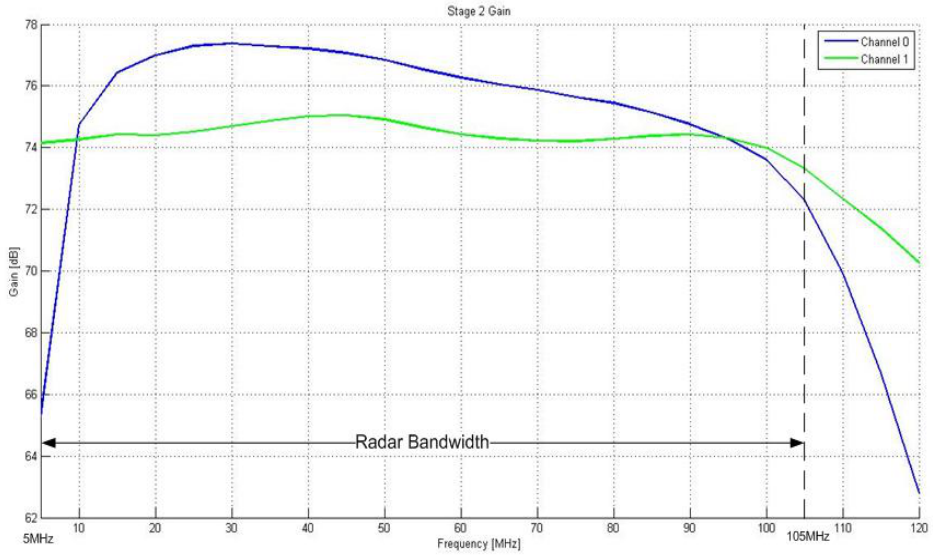

Figure 5.3. L-band to Baseband Downconverter Gain Measurement

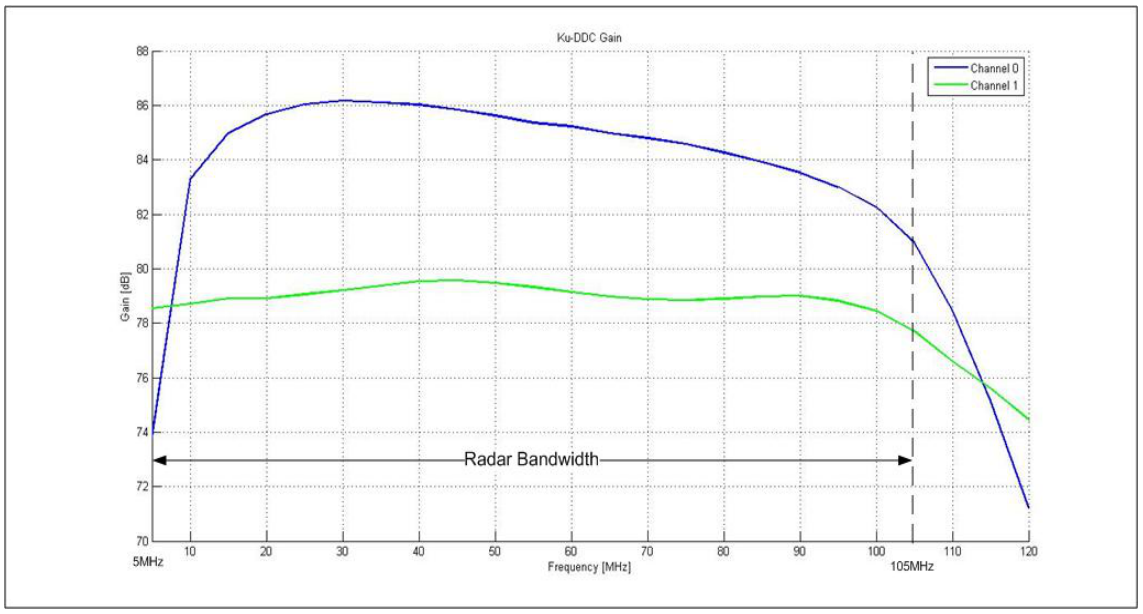

Figure 5.4. Ku-DDC Gain Measurement

5.1.3 Channel Isolation Measurements

Isolation between two channels on the receiver is desired when using the radar receiver for interferometry. This is important because contamination from interchannel coupling can bias phase estimation when correlating data between channel 0 and channel 1. Isolation can be measured by injecting a known source at the input of the receiver while measuring the corresponding output power on the opposite channel. This measurement was performed for the Ku-band to L-band downconverter as well as the L-band to baseband downconverter. Figures 5.5 and 5.6 show the measured coupling between channel 0 and channel 1. The Ku-band to L-band downconverter is shown in Figure 5.5 having interchannel isolation values ranging between 65dB and 76dB over the radar bandwidth while analysis of Figure 5.6 shows isolation values as low as 50dB over the radar bandwidth. Thus, interchannel isolation can only be as good as observations for the L-band to baseband downconverter.

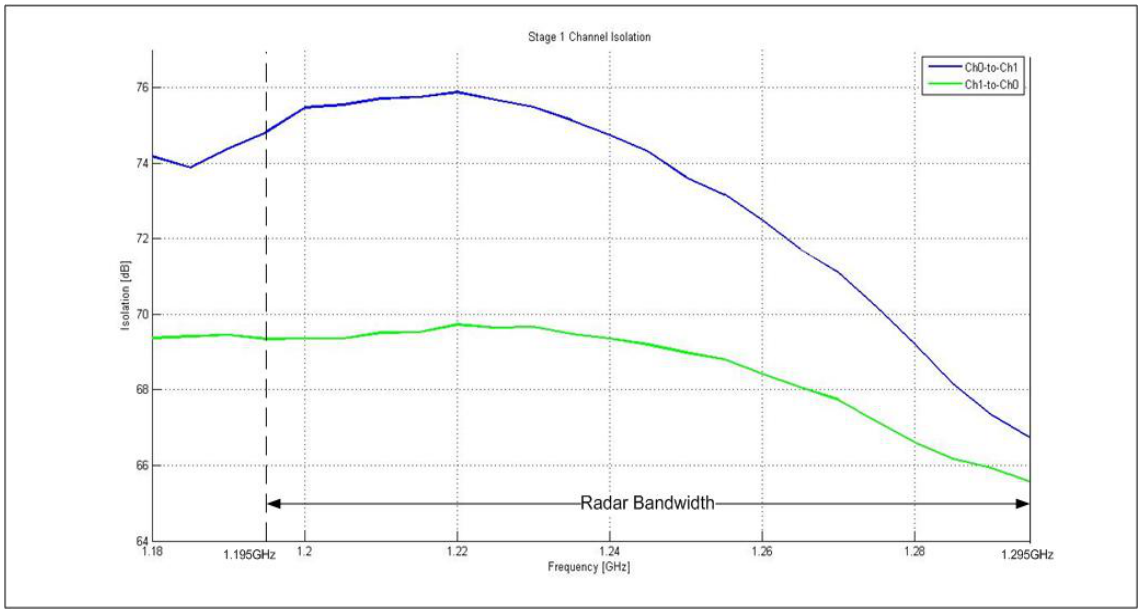

Figure 5.5. Ku-band to L-band Downconverter Channel Isolation Measurement

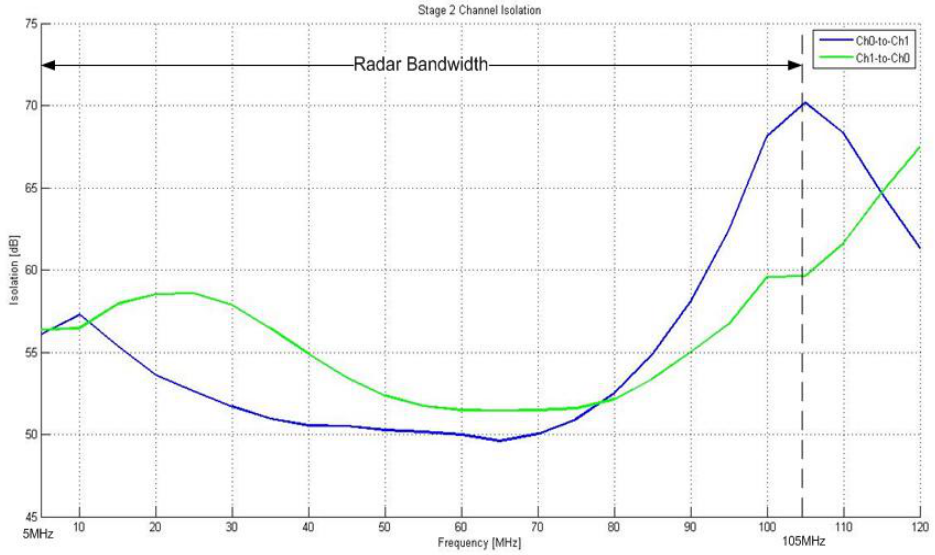

Figure 5.6. L-band to Baseband Downconverter Channel Isolation Measurement

There are numerous signal paths where interchannel coupling can occur. The two main paths can be attributed to the supply for each channel of their carrier

signals through the LO distribution network, which physically connects each channel. The interchannel coupling is partially controlled with filters used to pass the 1.3GHz and 12GHz carrier frequencies while rejecting the RF signals from the LO path. Other coupling paths exist besides the main LO distribution circuit which include unshielded connector junctions at the edge of the PCB, waveguide flange junctions, and the receiver antenna interfaces, just to name a few.

Prevention of interchannel coupling can be done through filtering, shielding, or other hardware modifications. Thus far, filtering combined with the inherent component-level isolation have been the primary mechanisms for preventing cross-talk at the LO distribution interface. Consequently, problems encountered in [19][18] have also lead to special enclosure designs that further prevent coupling through the air and PCB interface. Presently, a new PCB and enclosure are being designed for Ka-band applications. The goal is to see whether or not hardware modifications to the PCB and enclosure affect isolation performance. Details on this particular topic are not presented in this thesis.

5.1.4 Noise Figure Measurement

The noise figure is a measure that quantifies how much of desired signal is degraded noise. The noise factor, F, a dimensionless representation of noise figure, can be calculated for a cascade of microwave components using the Friis equation [12],

$$F = F_1 + \frac{F_2 - 1}{G_1} + \frac{F_3 - 1}{G_1 G_2} + \cdots \tag{5.2}$$

where subscripts 1, 2, and 3 represent the order of each component in the cascaded microwave system. Equation (5.2) is typically used for calculating the total noise figure from components in a radar system that have individually known noise figure and gain. For instance, F_1 and G_1 could represent the parameters for a lossy transmission line or a low noise amplifier, typical components for all radar receivers.

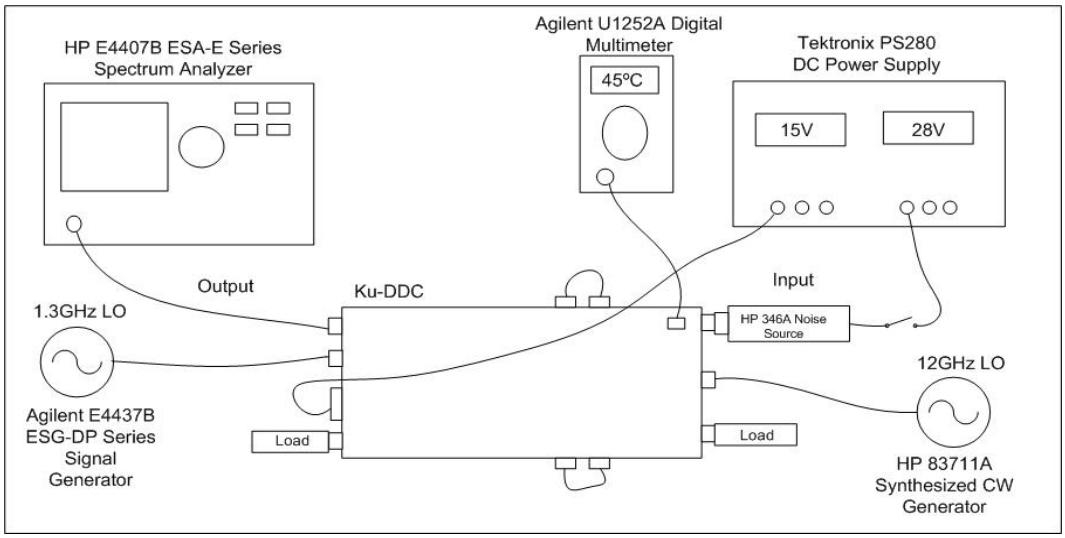

Figure 5.7. Experimental setup for measuring noise figure using the Y-Factor Method.

For this system, the noise figure was measured and calculated using a technique called the Y-Factor Method. Figure 5.7 shows the Y-Method experimental setup including some of the equipment such as a 28V noise source, a 28V power supply, and a spectrum analyzer with the capability of measuring channel power. For this measurement, the spectrum analyzer's resolution, video, and integrating bandwidths were adjusted to 1kHz, 10kHz, and 1MHz, respectfully, allowing for a more accurate measurement of noise power at the output of the receiver.

The Y-factor method calculates the noise power by taking the ratio between the noise power measured for hot and cold loads, measured at the output of the receiver. This ratio is given as,

$$Y = \frac{P_{HOT}}{P_{COLD}}, \tag{5.3}$$

where P_{HOT} and P_{COLD} represent the measured noise power when the noise source is turned on and off, with the on state relating to the condition of elevated noise. Since the noise source is a known quantity in the experiment, a parameter called ENR or

excess noise ratio is given. This parameter is provided by the noise source and varies depending on the frequency of operation. The ENR is expressed as,

$$ENR = \frac{(T_{HOT} - T_{COLD})}{T_{REF}} \tag{5.4}$$

where T_{HOT} and T_{COLD} represent on and off temperature of the noise source while T_{REF} is the reference temperature. The reference temperature was measured using a temperature probe. Typically, $T_{COLD} \cong T_{REF}$, in which case, (5.4) is rewritten as,

$$ENR = \frac{T_{HOT}}{T_{COLD}} - 1. \tag{5.5}$$

By rearranging the terms in (5.5), it becomes possible to solve for T_{HOT}. Using (5.3), the value of Y-factor is determined by understanding that power and temperature are proportional quantities. Thus, (5.3) can be rewritten as,

$$Y = \frac{T_{HOT}}{T_{COLD}}. \tag{5.6}$$

Since heat is a primary source of noise for any electronic device, temperature becomes an intuitive quantity to deal with when calculating noise figure. Thus, noise figure can be expressed as,

$$F_{REC} = 1 + \frac{T_e}{T_{REF}}, \tag{5.7}$$

where

$$T_e = \frac{T_{HOT} - YT_{COLD}}{Y - 1} \tag{5.8}$$

represents the equivalent noise temperature of the receiver. Applying the Y-factor method, the measurement of noise figure for the Ku-DDC is illustrated in Figure 5.8. It should be noted that representation of noise figure shown in Figure 5.8 is calculated

for the receiver alone. Incorporating the loss from the transmission lines connecting the receiver to the antennas adds to the overall noise figure,

$$F|_{dB} = F_{REC}|_{dB} + L_{TL}|_{dB}, \tag{5.9}$$

where $L_{TL}|_{\text{dB}}$ is the loss in the transmission line connecting the antennas to the receiver. The transmission line loss was approximated 1.5dB, thus, by using (5.7) and (5.9), it can be seen that the line loss adds 1.5dB of noise to the measurements shown in Figure 5.8. Further analysis of Figure 5.8 shows that the noise figure between channel 0 and channel 1 differed by approximately 2dB. The difference in noise figure was attributed to the difference in gain described in Section 5.1.2. By using (5.2), it can be seen that changes in a component's individual gain and noise figure directly affect the overall system noise figure.

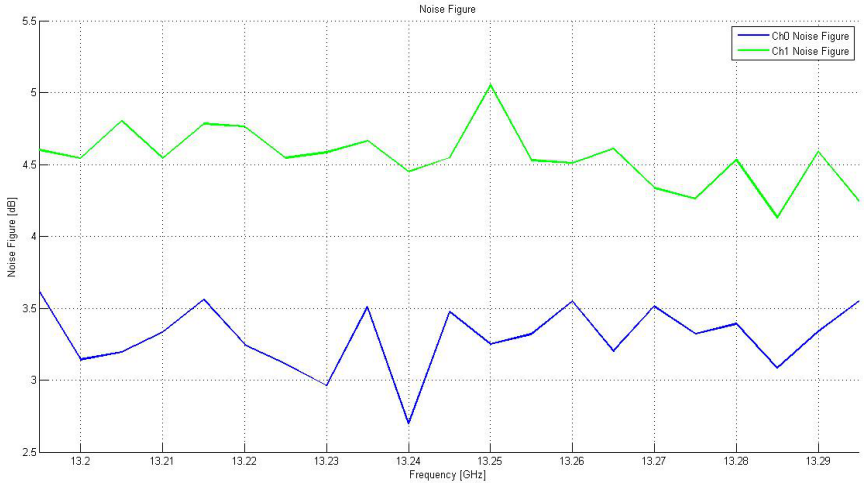

Figure 5.8. Noise Figure Measured using Y-Factor Method.

5.1.5 Image Rejection Measurement

An image is a frequency or band of frequencies resulting from the non-linear operation of a mixer. For this particular radar system three images are created

from the two-stage downconverter. Figure 5.10 shows where the images occur with respect to the RF band. These image frequencies are undesired and unavoidable if left unchecked. Image frequencies can hinder the performance of the radar since they exist outside the intended bandwidth of the radar. This becomes problematic for the antenna if the image band is well matched. A discussion of beam and impedance matching is present in Section 5.3 of this chapter. As a consequence for having a two-stage design, three image bands emerge; specifically, I_1, I_2, and I_3 shown in Figure 5.10. From this figure, it is apparent that I_1 and I_3 are distant enough from the RF band that they are likely to be suppressed by the filters in the receiver. On the other hand, suppressing I_2 with filtering alone is very difficult since the amount of cut-off necessary would require a filter well out-of-reach in terms of design capability. As discussed in Section 4.1.1, two image-reject mixers were employed to help suppress the image band. Figure 5.9 shows image-reject ratio measurement, which represents the amount of rejection between the I_2 and RF bands. The rejection of I_2 displays behavior contradictory to that of an image-reject mixer, and more towards rejections enforced primarily from filtering. This is most apparent in the shape of the rejection ratio, which is similar to a filter's roll-off. Thus, poor rejection of I_2 can be observed from Figure 5.9 which is unfortunate due to the introduction of data contamination since RF and I_2 downconvert to the same baseband signal. The image rejection ratio can be improved by increasing the frequency of the baseband signal, thus increasing the separation of the desired RF band and undesired image band.

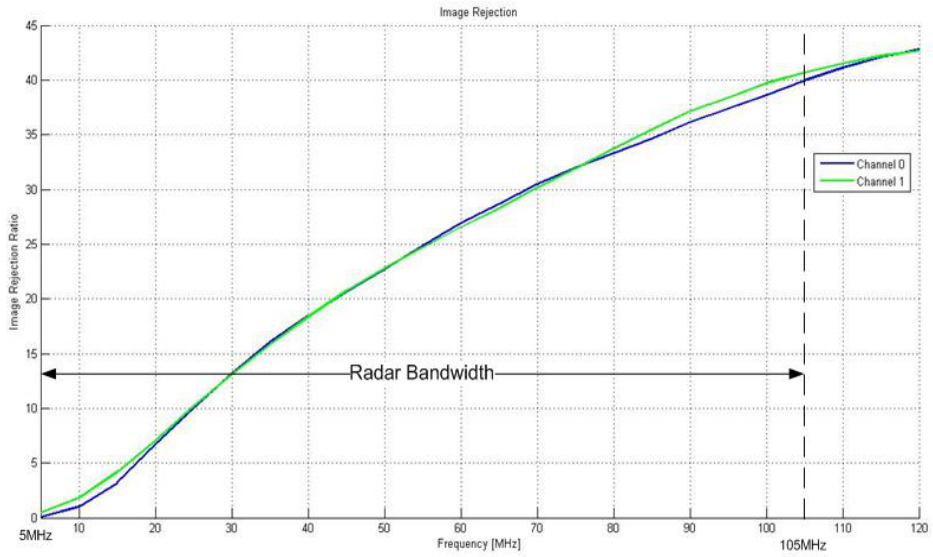

Figure 5.9. Image rejection measurement of the Ku-DDC

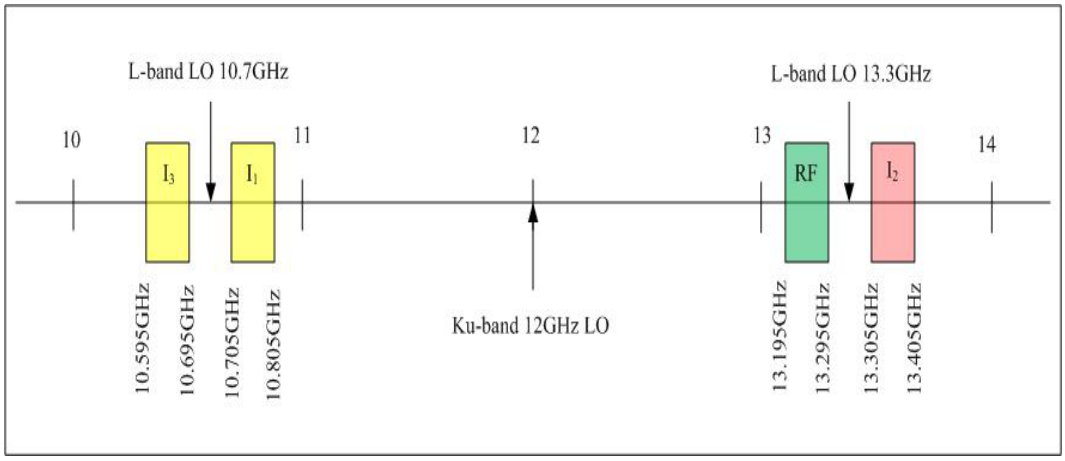

Figure 5.10. Image Frequency Chart

5.1.6 Linearity Measurements

The receiver is a nonlinear device where observations such as gain compression and third-order intermodulation distortion are products of this nonlinear behavior.

In this section, measurements of gain compression and third-order intermodulation distortion are presented.

Gain compression is defined as the point at which the gain of the receiver saturates and deviates from an ideal gain track. Typically, the 1dB compression point, P_{1dB}, references the point when the receiver's output power saturates, decreasing by 1dB down from the ideal gain. The measurement of gain compression is straight-forward and was conducted in a manner similar to the gain measurements discussed in Section 5.1.2.

Intermodulation distortion is a type of interference measured by injecting a two-tone signal at the input of the receiver. This two-tone signal is represented as,

$$x(t) = \cos(2\pi f_1 t) + \cos(2\pi f_2 t), \tag{5.10}$$

where $f_1 < f_2$. For this experiment, $f_1 = 13.240$GHz and $f_2 = 13.250$GHz are translated after downconversion to 60MHz and 50MHz, respectively. The output response of the receiver can be modeled as a Taylor series,

$$y(t) = y(0) + \sum_{m=1}^{M} x^m(t) \left[\frac{d^m y(t)}{dx^m(t)}\right]_{x(t)=0}, \tag{5.11}$$

where $M = 3$ is the maximum number of terms taken in the model. The frequency locations of the third-order intermodulation products can be determined by expanding (5.11). As a result, the location of these spurious signals are found within the radar bandwidth at $2f_1 - f_2 = 13.230$GHz and $2f_2 - f_1 = 13.260$GHz, which translate, after downconversion, to 70MHz and 40MHz, respectively. Thus, the measurement made at the spectrum analyzer is the downconverted representation of (5.11). Figure 5.11 shows the setup for measuring the third-order intermodulation product.

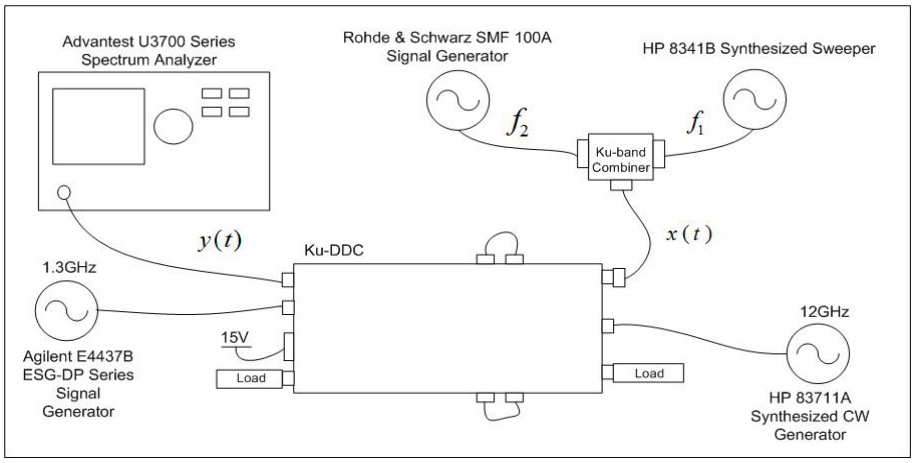

Figure 5.11. Experimental Setup: Third-Order Intermodulation Product

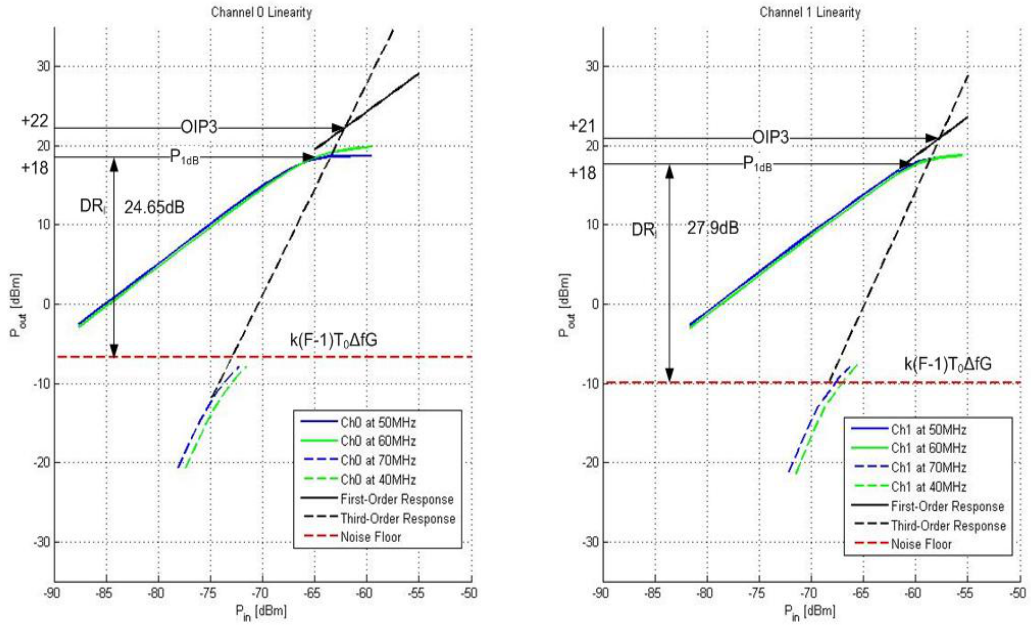

Figure 5.12. Linearity Measurements

Measurements such as P_{1dB}, OIP3, and DR_l describe the linearity performance of the receiver. Figure 5.12 shows these measurements for both channel 0 and channel 1. The 1dB compression point was measured for both channels to be approximately

+18dBm. As mentioned prior, this measurement establishes the maximum output power level of the receiver. Using this measurement, the linear dynamic range of the receiver is calculated as,

$$DR_l = \frac{P_{1dB}}{N_0}, \tag{5.12}$$

where N_0 is the output noise power of the receiver. The output noise power is given as,

$$N_0 = k(F-1)T_0\Delta f G, \tag{5.13}$$

where $k = 1.38 \times 10^{-23}$ J/K is Boltzmann's constant, F is the receiver noise figure, T_0 is the reference temperature of the receiver, Δf is the receiver bandwidth, and G is the total gain of the receiver. Using (5.12) and (5.13), the linear dynamic range was calculated to be 24.7dB and 27.9dB for channel 0 and channel 1, respectively.

The next measurement involved finding the intersection point between the ideal first- and third-order responses of the receiver also known as the OIP3 or third-order intercept point referred to the output. The OIP3 measurement was approximated to be +22dBm and +21dBm for channel 0 and channel 1, respectfully. This measurement represents the point when the output power level of the third-order intermodulation product matches the power level of (5.10) after downconversion. Further analysis of Figure 5.12 shows the OIP3 in close relation to the P_{1dB} suggesting a chance that a saturated receiver could introduce spurious signals at the output of the receiver. Thus, receiver saturation is an undesired affect, preventable by increasing antenna separation or reducing transmit power recall Section 3.1 on transmitter and receiver isolation for continuous-wave or FM-CW type radars.

5.2 Ku-Band Dual-IF Upconverter Evaluation

5.2.1 Peak Power Measurement

The transmitter peak power is set by a solid state amplifier, calibrated to +20dBm or 100mW. This relatively low peak power level is set because the radar operates in

FM-CW mode, allowing for long integration times over coherent targets such as trees, crops, and buildings. Peak power was measured using an Agilent spectrum analyzer; before setting up this measurement, however, a control measurement was required to ensure that the correct power was being measured on the spectrum analyzer. The control source in this experiment was a Rohde & Schwarz signal generator. Figure 5.13 shows the transmitter peak power measured over the signal bandwidth, RF, as well as the image bandwidth, I_2, (see Figure 5.10). Analysis of Figure 5.13 shows that part of I_2 is transmitted with the desired RF signal. This transmission occurs because the RF and I_2 bands are separated by 10MHz making it difficult to suppress the image through filtering alone. Section 5.3.2 discusses and illustrates the antenna performance when operating out-of-band.

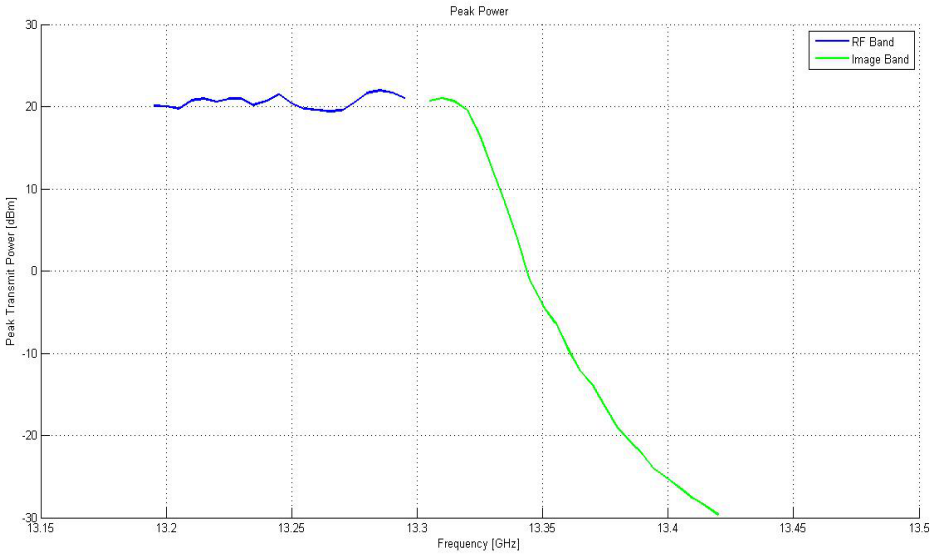

Figure 5.13. Peak Power Measurement

5.2.2 Chirp Generator Measurement

The phase of a linear chirp waveform can be described as the following equation,

$$\theta(t) = \frac{\pi \Delta f}{T} t^2 + 2\pi f_0 t + \theta_0, \tag{5.14}$$

where Δf is the bandwidth of the chirp, T is the duration of the chirp, f_0 is the start frequency of the chirp, t is time, and θ_0 is some constant phase offset. The phase was estimated by solving for the coefficients of the quadratic in (5.14). This was accomplished by using a least squares algorithm [15] in conjunction with a best fit curve. The chirp waveform was measured with an Agilent oscilloscope connected through LAN[1] via MATLAB. Before measuring the chirp waveform, a controlled experiment was conducted to ensure that the setup worked properly. In this experiment, a single-tone waveform was measured on the oscilloscope and confirmed in post-processing using MATLAB. A linear FM chirp was created from both of the waveform generators described in Sections 4.2.1 and 4.2.2. The chirp generators were setup with a start and stop frequency at 5 and 105MHz and chirp duration of 1ms. The waveform was captured over a 10ms sample window and digitized at a rate of 400MHz. Figure 5.14 shows measurement results taken from both the Tektronix and Agilent waveform generators. The left plot compares estimated phase with that of a simulated chirp while the right plot gives the frequency-time representation of the measured phase. This measurement is obtained by taking the time-derivative of (5.14) shown as

$$f(t) = \frac{1}{2\pi} \frac{d\theta(t)}{dt}. \tag{5.15}$$

[1]Local Area Network

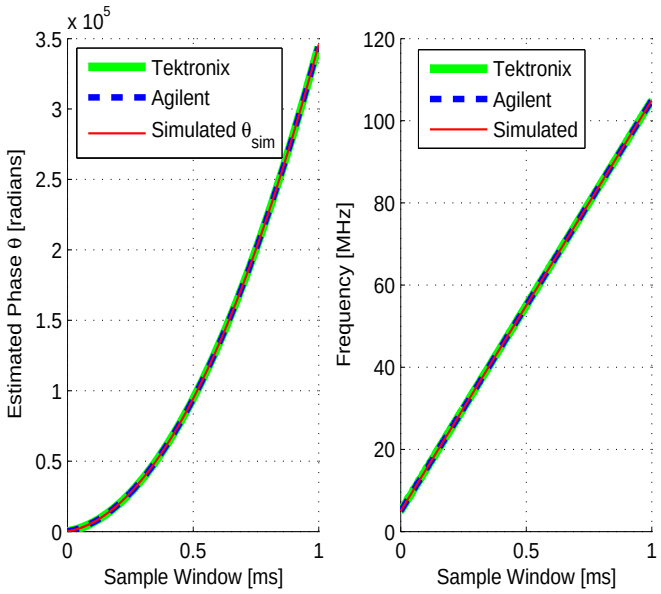

Figure 5.14. Phase estimation measurement compared with simulated chirp phase (left). Frequency-time representation for phase estimates (right).

Linearity tends to be an important factor concerning the performance of the waveform generator. From the results presented in Figure 5.14, it is not completely evident whether or not non-linearities are a dominating factor during waveform generation. These non-linearities can be described as additional time-dependent terms to (5.14) or as a piece-wise type non-linearity introduced from an imperfect digital-to-analog conversion process. The electrical interaction between the radar hardware and chirp waveform is also significant factor since the radar hardware consists of non-linear components that may or may not operate in the preferred linear region. This potential non-linear interaction between the hardware and signal has not been covered, but should be measured and explored for further future performance assessment. This is important because these nonlinear effects introduce ambiguities in the radar image that become unusable during data processing.

5.3 Antenna Measurements

5.3.1 Impedance Matching

Tuning the antenna to the desired operating frequency was necessary before beginning any measurements in the near-field chamber. This was accomplished by measuring the return loss on a 20GHz vector network analyzer using a precision adjustable short[2] connected to the end of the slotted-waveguide antenna as the tuning mechanism. Having the ability to precisely adjust the position of the short made it possible to enforce the $\lambda_g/4$ spacing between the short and the final slot in the antenna array. This is important because the placement of the short in this way produces an electrical open-circuit which simplifies the antenna model established in Section 4.3. It should be noted that the spacing between the short and final slot can also be an integer multiple of $\lambda_g/4$. Figure 5.15 shows the return loss measurement of one of the three slotted-waveguide antennas. It should be noted that the antenna bandwidth is less than the 100MHz receiver bandwidth when defined for a VSWR <= 2. However, this impedance mismatch at the band edges allows for a natural taper across the waveform behaving similar to a window function used for minimizing range sidelobes during data processing. The narrow band response of the antenna is due to the fact that for a resonant or standing wave antenna, the bandwidth is inversely proportional to the number of elements in the array, and can be estimated using the following equation [8],

$$BW = \pm\frac{50\%}{N}, \tag{5.16}$$

where N is the number of elements in the array for a VSWR <= 3. Using (5.16), the 70-element slotted-waveguide array, as described in Section 4.3.1, should have a predicted bandwidth of 1.42% or 189MHz, which is close to the measured bandwidth

[2]Precision adjustable shorts were produced by Robert A. Rivers at Aircom, Inc.

of 120MHz or 0.91% shown in Figure 5.15. In order to double the bandwidth of the slotted-waveguide array the number of elements in the array must be reduced by a factor of 2. One way to achieve this doubling effect is to feed the array from the center, creating two subarrays that half the input impedance, effectively, reducing the size of the array without changing the radiation pattern.

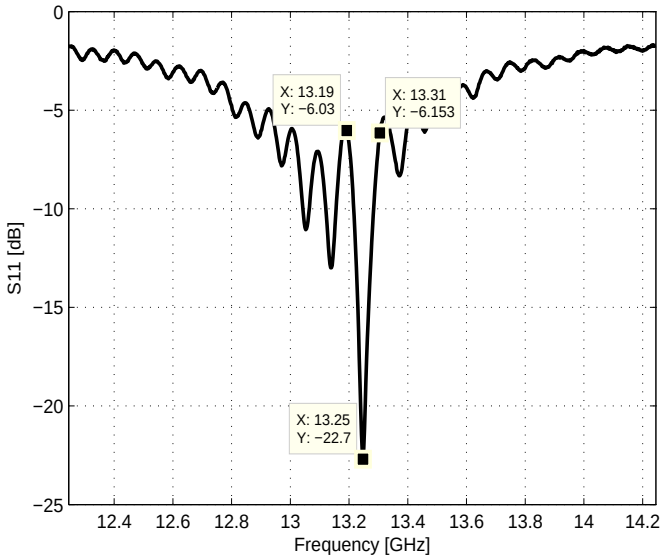

Figure 5.15. Return Loss Measurement.

5.3.2 Beam Matching

Impedance matching of the antenna is important in that it ensures that the antenna radiates energy instead of storing or reflecting it. Figure 5.15 shows that the antenna is well matched at 13.245GHz. Further analysis of Figure 5.15 suggests other potential matching location seen as multiple resonances surrounding this frequency. While the input impedances are well matched at these are frequencies the match does not necessarily imply good beam performance in the desired broadside direction. For this reason, a combination of impedance and beam matching is enforced to ensure proper antenna performance. Figure 5.16 shows a collection of azimuthal pattern

measurements spanning over the RF and image frequency bands. Figure 5.16 also shows the consequence of deviating too far from 13.245GHz, demonstrating the effects of beam splitting. This behavior results from the antenna's resonant structure design. Hence, when the antenna operates off resonance, it starts behaving less like a resonant antenna and more like two opposed traveling wave antennas. A traveling wave antenna is used in frequency scanning applications and has behavior characterized by observations seen in Figure 5.16.

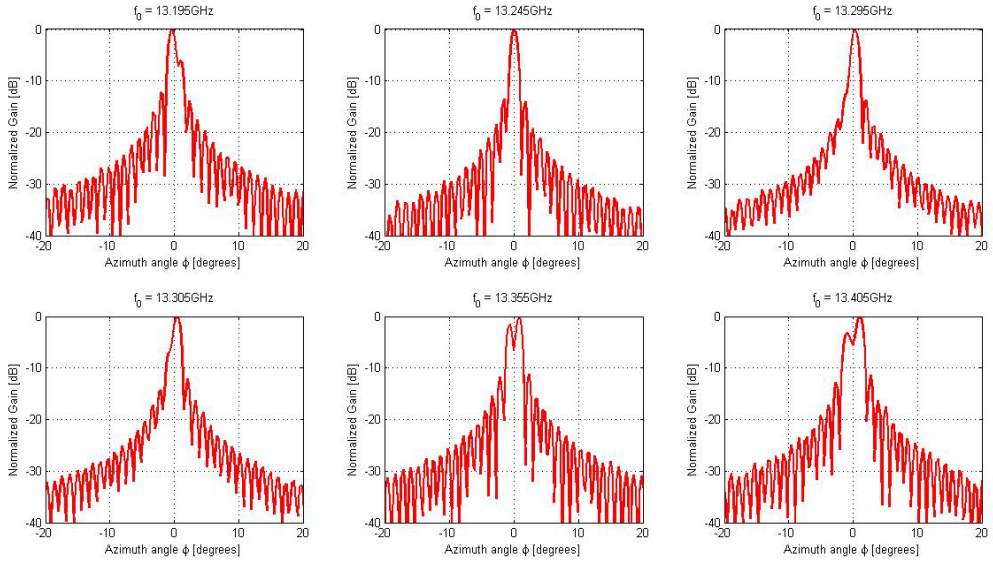

Figure 5.16. Illustration of beam mismatching.

5.3.3 Near-Field Measurements

Antenna measurements were conducted using the near-field antenna chamber located in the basement of Marcus Hall at the University of Massachusetts. Figure 5.17 shows how the antenna was setup inside the near-field chamber. Measurements were taken using the NSI (Nearfield System, Inc.) 2000 software. This was implemented by measuring the magnitude and phase of the voltage in a rectangular grid in front of the antenna aperture, thus requiring the painstaking process of aligning the antenna to the measuring probe, which was necessary in obtaining good radiation patterns.

Once measurements were completed, a spatial-Fourier transform converted the measured near-field data to far-field radiation patterns in azimuth and elevation. Figure 5.18 shows good agreement between the measurements and simulations. Simulations were written in MATLAB using (4.6) and (4.9) for measurements of azimuthal and elevation patterns, respectively.

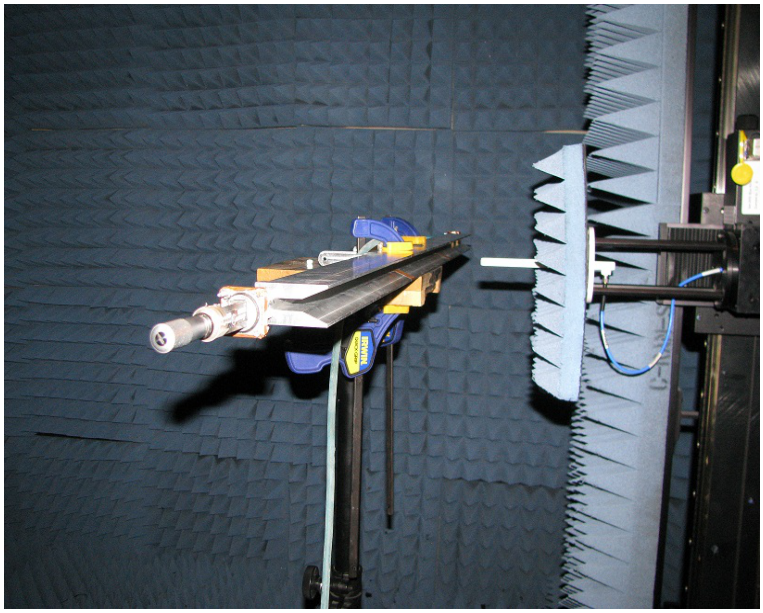

Figure 5.17. The slotted-waveguide-horn antenna measured inside the near-field chamber.

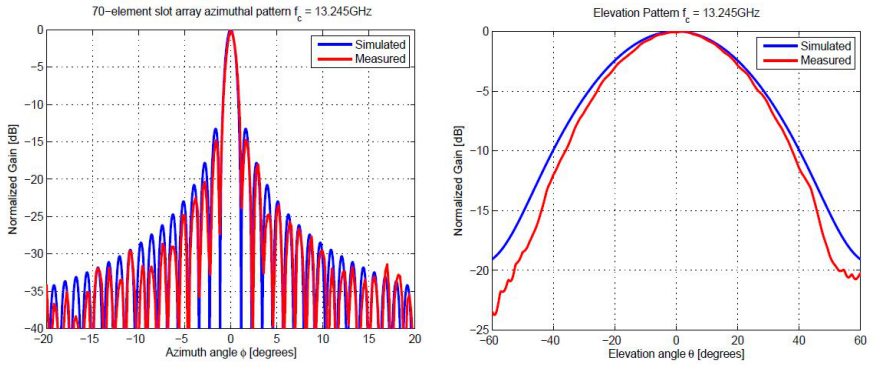

Figure 5.18. Azimuth (left) and elevation (right) far-field patterns.

So far, a comprehensive analysis and discussion of the hardware performance has been presented, breaking down the receiver, transmitter, and antenna components by highlighting some of their key characteristics and figures of merit. Hence, a measure of their collective performance can be obtained by deploying the radar in a location suitable for interferometry. In the following chapter, detailed analysis and discussion of results obtained from Mount Sugarloaf are presented, providing measures which demonstrate the radar's ability to produce interferometric results.

CHAPTER 6

INTERFEROMETRIC RESULTS

In this chapter, interferometric observations from Mount Sugarloaf are presented as well as a comprehensive look into some of the troubleshooting techniques used to improve the quality of the radar image. A description of hardware modifications is also presented followed by an assessment of image quality. Lastly, analysis and discussion on topographic estimates from Mount Sugarloaf are provided along with geographically transformed results.

6.1 Site Background

In order to provide initial feedback on the overall performance of the radar, experiments have been conducted at sites located in the area surrounding the University of Massachusetts, Amherst. These tests site include Skinner State Park and Sugarloaf State Park.

6.1.1 Mount Holyoke

Mount Holyoke, located in South Hadley, MA, elevation 285m, is part of Skinner State Park. This location was chosen, historically, for the success with deployments using a UMass built Ka-band radar interferometer [18]. Prior to the development of the Ku-band radar interferometer, access to the second level observation deck of the Mount Holyoke Summit House provided an excellent view of the Connecticut River Valley, however, in the following year, access to the observation decks were denied based on the condition of the deck support beams. As a result, a location in the

near vicinity of the Summit House was chosen to supplement the original location. Unfortunately, setup difficulties and constant shadowing from trees and other plant-life located in the foreground of the radar discouraged any future deployments at this location.

6.1.2 Mount Sugarloaf

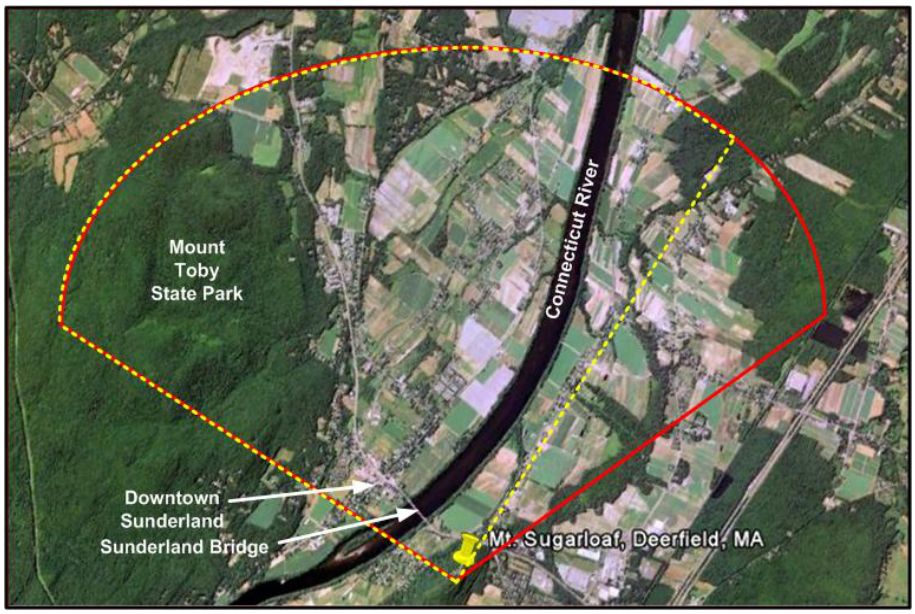

Figure 6.1. An aerial photograph is presented of the deployment site located at Mt. Sugarloaf in South Deerfield, MA (Google Earth). Areas highlighted in red and yellow (dashed) indicate scan locations for August 26, 2010 and June 3, 2011 deployments.

Sugarloaf State Park, located in South Deerfield, MA, elevation 199m, is part of Sugarloaf State Park. This location was chosen for its short commute from the university, access to the observation deck, and similar viewing geometry to that of Mount Holyoke. From this location, Sunderland, Mount Toby State Park, and the Connecticut River can be seen. Unlike Mount Holyoke, the Mount Sugarloaf observation deck was located several meters from the mountain's edge, hence, larger shadowed regions appear in directions where the mountain's edge was furthest from

the radar. Despite the inherent shadowing effects at each location, Mount Sugarloaf was chosen for future deployments.

6.2 Radar Deployment

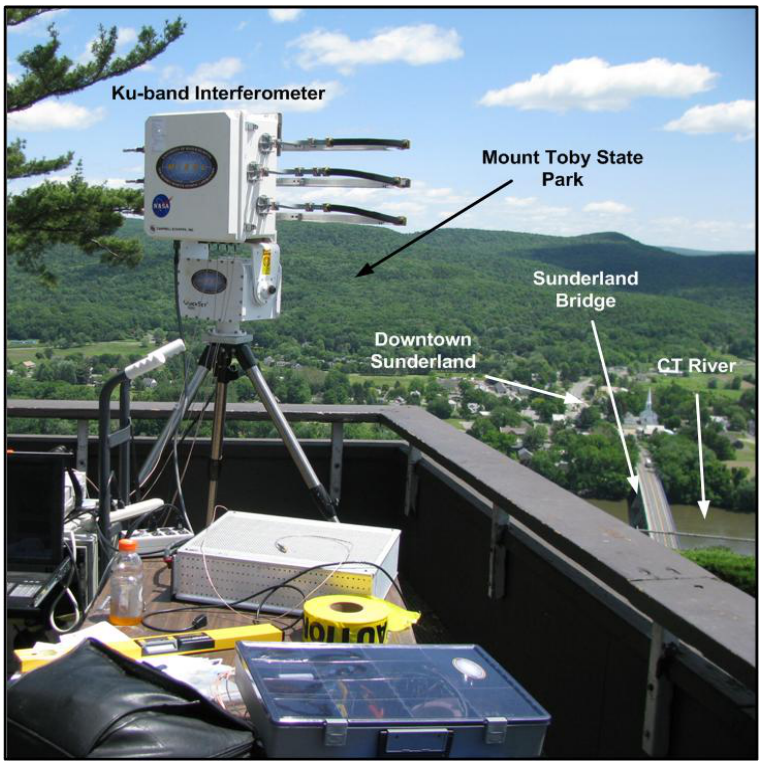

Figure 6.2. A photograph taken of the Ku-band interferometer at the Mount Sugarloaf observation deck looking out over downtown Sunderland, MA.

The radar interferometer was deployed at one corner of the lower observation deck looking out over Sunderland and South Deerfield, MA. An aerial view of the deployment site is presented in Figure 6.1 highlighting the approximate scan locations. Power was accessible via 20A outlets located in the stairwell leading to the upper-level observation decks. This was a critical requirement in that the radar was not battery operated. For each experiment, the radar was assembled and disassembled on site per deployment. As depicted in Figure 6.2, lifting the radar in it's assembled state would

have been quite cumbersome. As a result, experiments conducted at the mountain logistically required at least three people to ensure a successful deployment. The bulk of the radar assembly consists of setting up the positioner, securing the radar box to the positioner, attaching the three antennas to the radar box, and connecting power, control, and signal cables. Once deployed, configuration parameters were entered into the radar through a data acquisition program in LabView. Using this program, a configuration report was created, outlining some of the basic data acquisition parameters such as sample rate and pulse count; these parameters are described in Table 3.1 of Section 3.2.

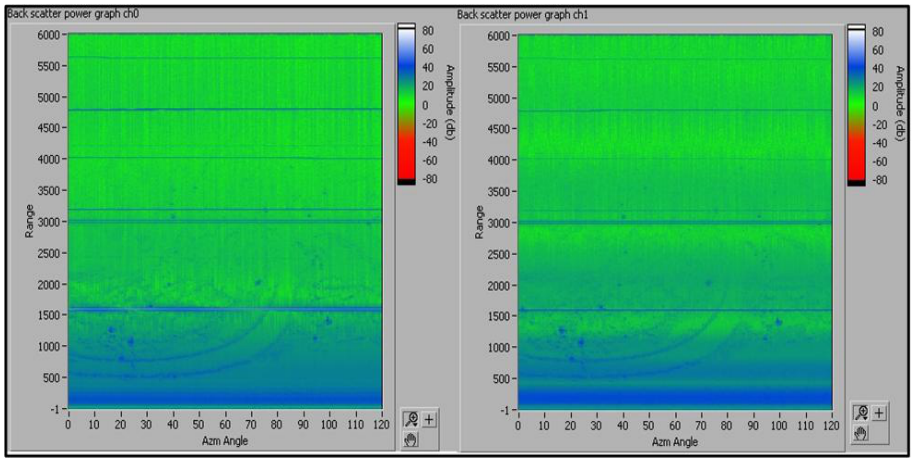

Figure 6.3. The backscattered power from channel 0 (left) and channel 1(right) collected in real-time on August 26, 2010 deployment at Mount Sugarloaf using the LabView data acquisition program.

For mountain observations, the radar was configured to make 90^o or 120^o scans at 0.5^o per position delivering 256 looks per position at a rate of 250Hz. Since the sample rate was usually kept at 2MHz, the digitizer can uniquely sample signal frequencies as high as 1MHz, or ranges as far as 6km. The source generator is configured to provide a 100MHz bandwidth chirp resulting in a slant range resolution of 1.5m. Depending on the signal strength of the returning echo, the amplitude range on the ADC can also be configured to increase the gain of the incoming signal. In order to determine

the signal strength before automating the collection process, a quick-scope program in LabView was used to display the digitally converted voltage data in real-time. To maximize the success rate of the radar deployment, a large number of scans can be programmed into the configuration report; this was common practice since the radar was interruptible at any time during the acquisition process. Figure 6.3 shows real-time backscattered power computed after subsequent position data acquisitions. This real-time data display was incorporated into the main data acquisition program used with the Ka-band interferometer. This capability provided instant feedback to the performance of the radar reassuring confidence in the collected data.

6.3 Initial Results

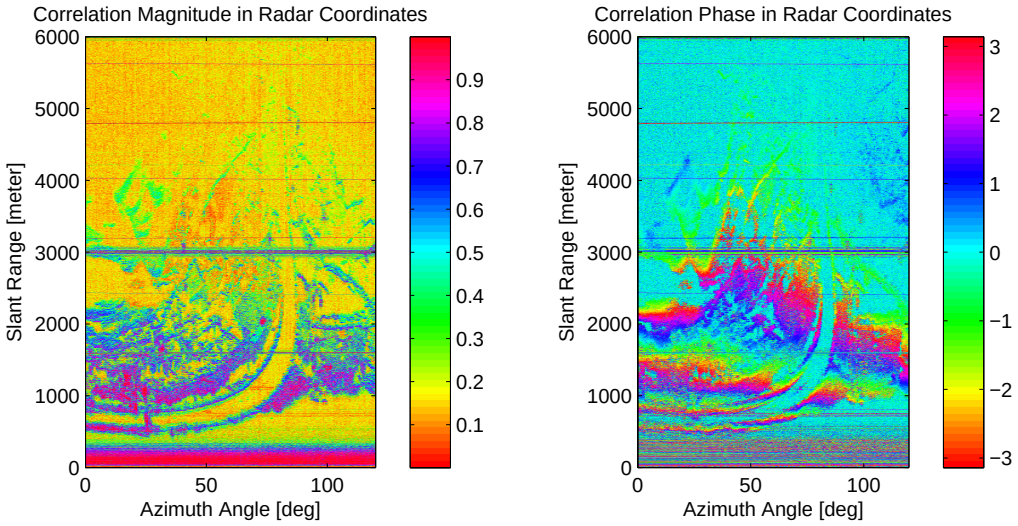

Figure 6.4. Correlation magnitude (left) and interferometric phase (right) observed from Mount Sugarloaf on August 26, 2010.

Initial results from Mount Sugarloaf are shown in Figure 6.4 in the form of correlation magnitude and phase taken between the two spatially separated antennas using 2.2 to perform the calculation. These results were collected over a 120^o azimuthal swath presenting a panoramic snap-shot of downtown Sunderland and South

Deerfield, MA. From the correlation magnitude in Figure 6.4, the Connecticut River shows low correlation magnitude while trees and other fixed objects such as building, mountains, and parked cars show correlation magnitudes close to unity. Low correlation values over the river are a result from the random phase of the signal reflected from the water surface. Because of the fluidity of a water target, the phase of the reflected signal changes at time scales on the order of milliseconds, hence resulting in a low value for the interferometric correlation. Other physical phenomenon can also contribute to low correlations values through behavior such as forward scattering and absorption consistent with results having low SNR. However, the trees along the shoreline of the river exhibit very high correlation values providing contrast between the river and river's edge. This observation can be explained by dihedral scatterers formed by the orientation of trees and shoreline. Although observations of correlation magnitude show typical behavior over water, observations of the correlation phase behave unusually, portraying deterministic behavior in some areas. According to Figure 6.4, the interferometric phase appears to have measured values of approximately 0^o in locations with consistently low SNR, where the phase is expected to be more random. These locations include areas over water, shadowed regions, and locations in the far-field where the angle of incidence is near grazing. Despite these unusual results, observations over Mount Toby State Park exhibit phase fringes typical for topographic terrain.

Further analysis of Figure 6.4 shows "striping" at fixed range bins. By creating range profile of the correlation magnitudes averaged over all azimuth angles, it becomes possible to differentiate range anomalies from actual data. Figure 6.5 shows some of the more dominant interferers located at ranges (frequencies) of 1597m (266kHz), 3011m (501kHz), 3196m (532kHz), 4012m (668kHz), 4793m (798kHz), and 5609m (934kHz).

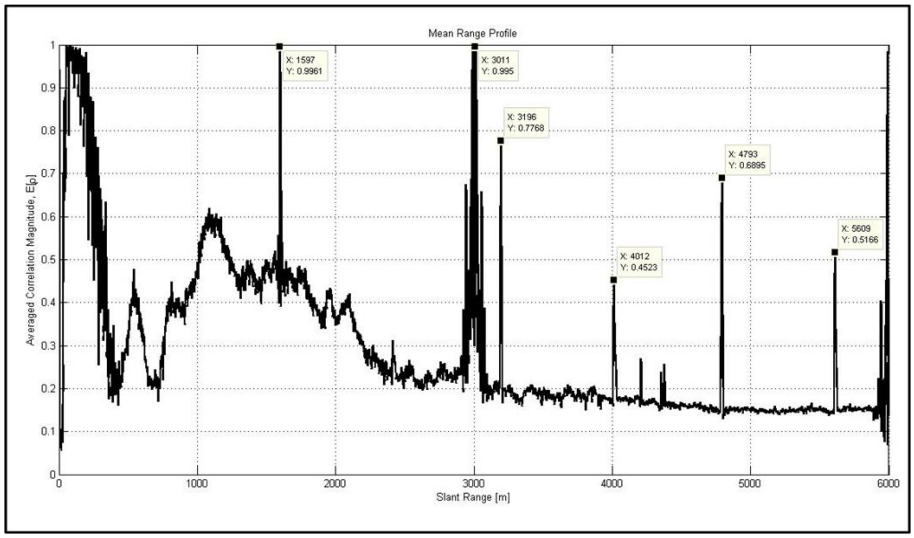

Figure 6.5. Mean range profile from data collected on August 26, 2010.

6.4 Hardware Modifications

Hardware modifications were required in order to address the problems observed in Figures 6.4 and 6.5. As discussed in Section 6.3, these problems appeared as unusual phase behavior and range striping, both hypothesized to be products of external and/or internal interference. This hypothesis was partially refuted after numerous laboratory experiments suggested internal sources to be the problem. During experimentation, the method which seemed most useful in determining these problems was to operate the radar in a receive-only mode. Using this approach, the receiver's role in image degradation could be determined. Isolating these types of problems to specific locations in the receiver required step-by-step observations. By meticulously de-embedding each receiver section, these measurements could deduce the general location of problems in the receiver. Figure 6.6 shows a crude receiver block diagram, pre-modification, representing the receive-only setup used to isolate areas affected by hardware interference. The letters circled in red represent specific locations in

hardware considered problematic. Table 6.1 shows five probable paths of interference leading to the data acquisition unit.

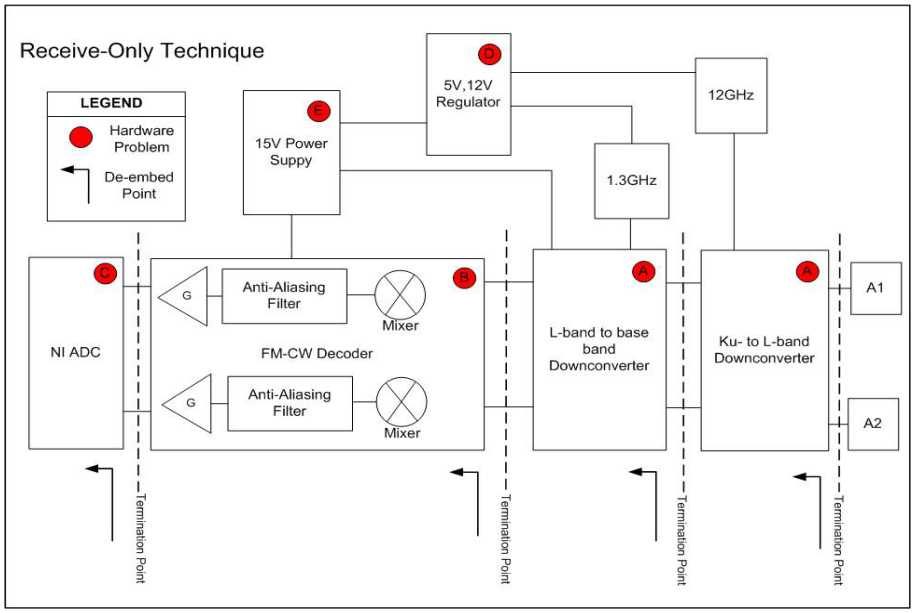

Figure 6.6. Receive-Only Block Diagram

Paths of Interference
$A \rightarrow B \rightarrow C$
$A \rightarrow E \rightarrow B \rightarrow C$
$B \rightarrow C$
$D \rightarrow E \rightarrow B \rightarrow C$
$E \rightarrow B \rightarrow C$

Table 6.1. Pre-modification paths of interference to the NI ADC

At each termination point, matched loads were utilized to isolate portions of the receiver. For example, by connecting a matched load to the input of the NI ADC, collected measurements would characterize only the NI ADC, completely isolating any contributions from the FM-CW decoder and the Ku-DDC. Figure 6.7 shows results using the LabView data acquisition program collected at several termination points in the radar. Figure 6.7a shows measurements of the NI ADC as described in the

previous example. From these results, it can be shown that interferers located at f_{NI1}, f_{NI2}, f_{NI3}, and f_{NI4} are inherent to the NI ADC and are, consequently, beyond the scope of change or modification by the user. Figure 6.7b shows measurements of NI ADC combined with the FM-CW decoder obtained when the termination point was moved to baseband. As a result, interferers from the FM-CW decoder were detected consisting of a fundamental interferer, f_I, and subsequent harmonics, $2f_I$ and $3f_I$ as well as low-level spurious signals throughout the sample space. As in Figure 6.7b, Figures 6.7c and 6.7d present similar observations as to the locations of f_I, $2f_I$, and $3f_I$, however, differences in power levels provide further insight suggesting that the problem lies closer to the Ku-DDC.

Another noticeable problem is the interference band ranging between 25kHz and 500kHz, detected using both the L-band and Ku-band termination points. Appendix D Figure D.1 provides a better depiction of this interference band. Upon further analysis, it appears that this interference band is only detected on channel 0, further complicating the troubleshooting process. Fortunately, an explanation to this anomaly can be found by comparing power levels at channel 0 and channel 1. Figure 6.8 shows subplots of results collected as the receiver was terminated at Ku-band. In this figure, markers clearly show a gain difference of approximately 13dB between channel 0 and channel 1 suggesting that the interference band detected on channel 0 could be hidden below the noise floor of channel 1. As a result, it was assumed that both channels shared this problem, thus simplifying experimentation and eventually hardware modifications.

So far, the receive-only technique has been able to establish a general idea of where to locate interference within the receiver block. The step that followed in this debugging process involved using an oscilloscope to probe areas in the receiver with suspected hardware problems. In reference to the red circled areas from Figure 6.6 as well as the interference paths listed in Table 6.1, it was determined that all suspected

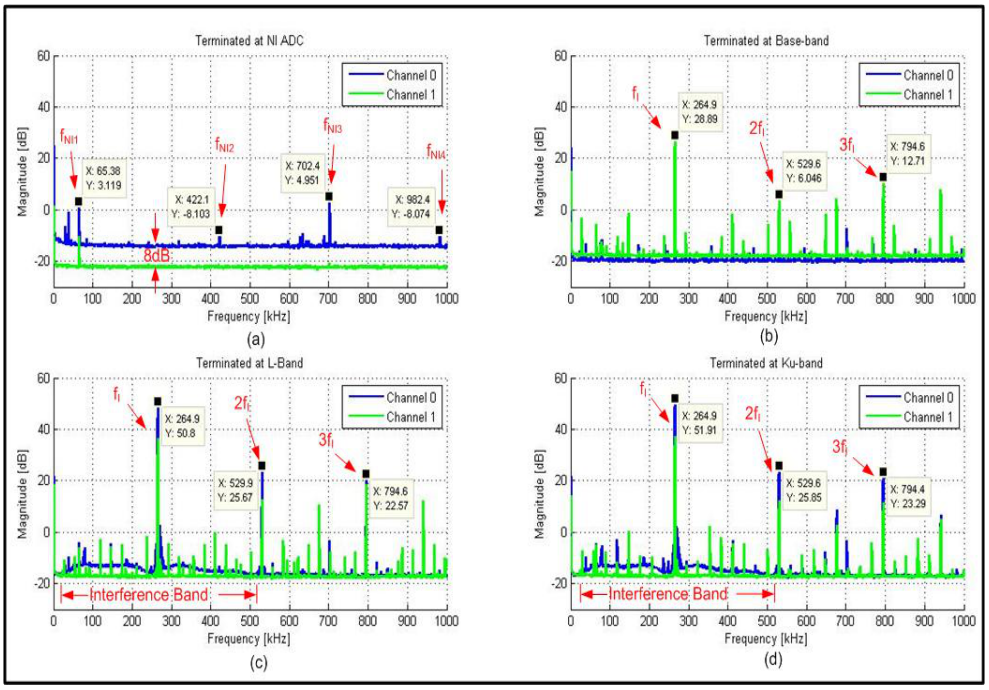

Figure 6.7. Measurement results using the receive-only technique. Termination points include the NI ADC (a), the baseband output of the Ku-DDC (b), the L-band output of the Ku-DDC (c), and the Ku-band input of the Ku-DDC (d).

areas, except for (C), required further analysis. After implementing a variety of power-up combinations using an external DC source and ripple attenuator modules (RAM), it was clear as to where the interference was originating from using the oscilloscope. From this debugging process, it was determined that interferers located at f_I, $2f_I$, and $3f_I$ were originating from the Ku-DDC (A), interfering with other circuitry through the 15V supply line. This observation was verified by unplugging the Ku-DDC during a baseband terminated receive-only measurement in which no interferers were observed. As for the other spurious signals, they were assumed to be caused by intermodulation distortion produced from the numerous cascade of amplifiers in the receiver (A and B). The interference band shown in Figures 6.7c, 6.7d, 6.10a, and 6.10 were determined to be caused by excessive voltage ripple from voltage regulators used in the system (A, D, and E). Originally, DC power was sourced

to the receiver from two 15V supplies requiring circuitry to regulate 15V to 5V and 12V in order to supply the correct voltages to the local oscillators facilitating the upconversion and downconversion. Similarly, the Ku-DDC takes in a 15V supply, internally regulating that voltage to levels usable by the low-power amplifiers and other low voltage circuits on that PCB. Unfortunately, these regulators produce a voltage ripple or ringing modulated on top of the DC, shared on both channels, between 25kHz and 500kHz. Coincidently, the voltage ripple seen on channel 0 and channel 1 can explain the interferometric phase problems observed in Figure 6.4. As a consequence to the voltage ripple's presence on each channel, a correlation performed in post-processing would have resulted in a zero phase contribution in addition to the resultant interferogram.

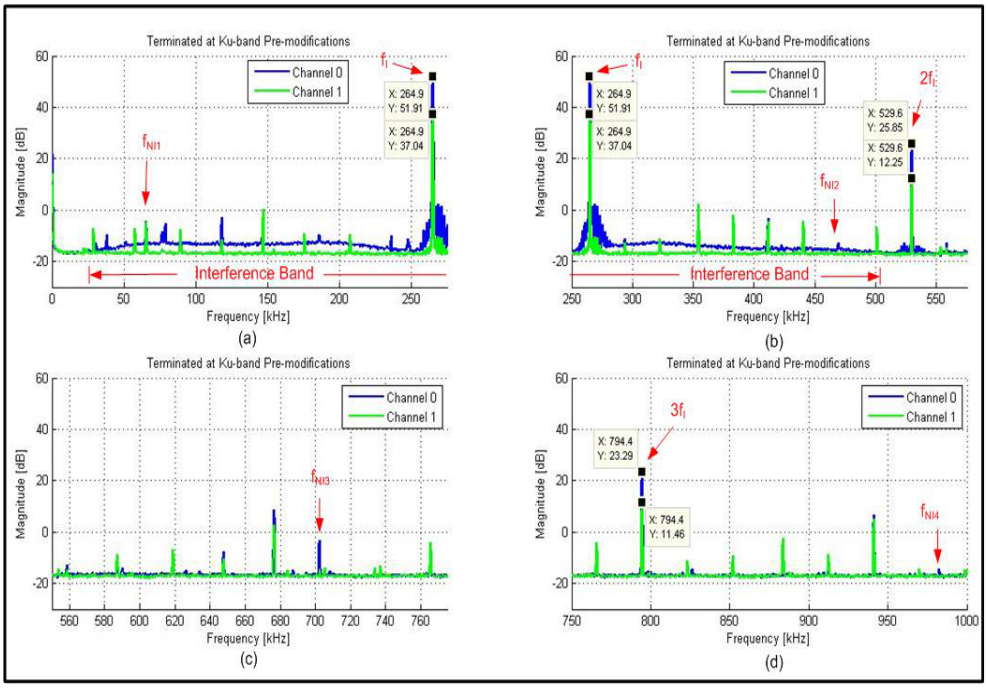

Figure 6.8. Results shown at the Ku-band termination point pre-modifications for the following frequency ranges: 0kHz to 275kHz (a), 250Hz to 575kHz (b), 550kHz to 775kHz (c), and 750kHz to 1000kHz (d).

In response to these findings, subsequent hardware changes were needed to mitigate this receiver interference. Figure 6.9 highlights the areas changed using green and yellow circles. Closer analysis shows that the Ku-DDC and the NI ADC remain unchanged due to their inherent complexity and fundamental role in the system. Consequently, modification to the NI ADC are beyond any scope of change as mention earlier; however, despite also being unable to modify the hardware in the Ku-DDC, a solution to minimize the effects of interference was determined. This involved separating the biasing circuitry for each component in the receiver in order to bypass the problems contained in the Ku-DDC. As a result, the Ku-DDC, the FM-CW decoder, and the local oscillators were all isolated to their own power supplies. Ripple attenuator modules (RAM) were also added to each line effectively reducing any potential ringing that could occur. Section 4.4 provides a description of the radar power supply. Lastly, the filters and amplifiers inside the FM-CW decoder were rearranged in order to suppress any spurious signals created before being sampled by the ADC.

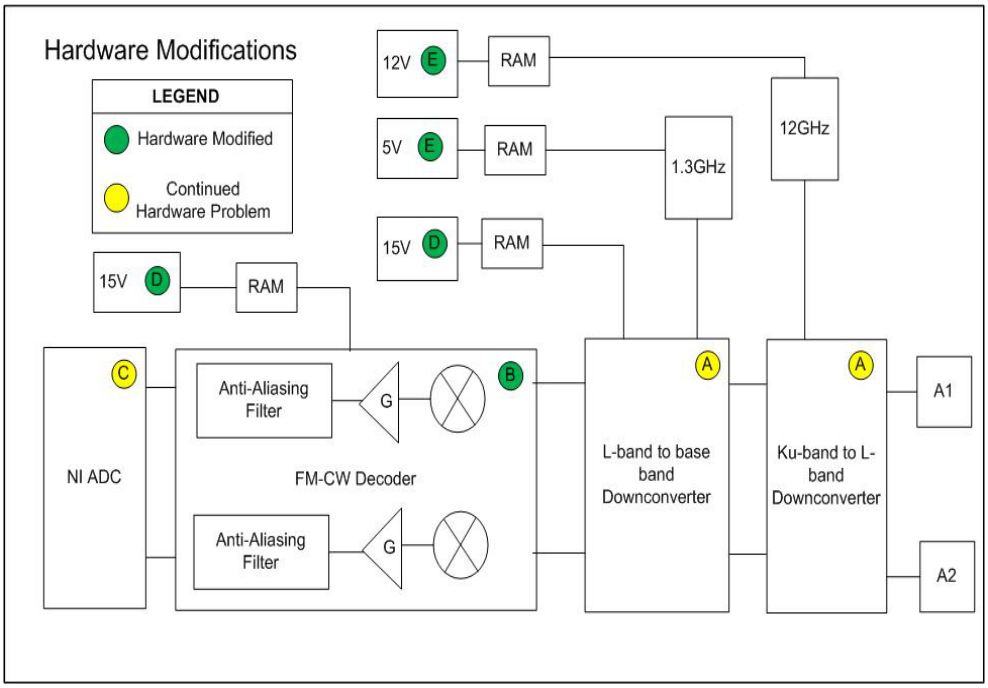

Figure 6.9. Hardware Modifications Diagram.

In order to reinforce the effectiveness of these changes, a post-modification, receive-only measurement was taken at the Ku-band termination point. The results from this experiment are presented in Figure 6.10. By comparing these results with corresponding pre-modification results, it was clear that these changes in hardware had significantly improved the performance of the receiver. As a result, interferers located at f_I, $2f_I$, and $3f_I$ were completely eliminated from the spectrum. The narrow-band interference between 25kHz and 500kHz has also been removed while the localized interferers created by the NI ADC remain visible. Lastly, the paths of interference from Table 6.1 have been bypassed as a result of these changes leaving only $A \rightarrow B \rightarrow C$, which, coincidently, has less significance than the other paths primarily because active components encountered along this path are band-limited, naturally rejecting these interferers before allowing them to reach the ADC.

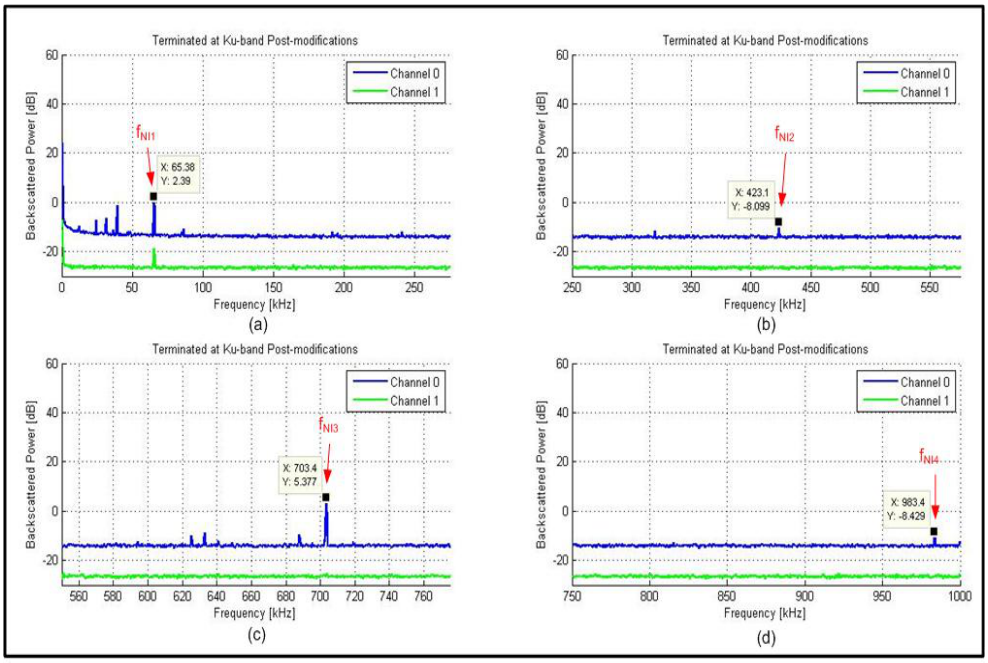

Figure 6.10. Post-modification results shown for the Ku-band termination point at the following frequency ranges: 0kHz to 275kHz (a), 250Hz to 575kHz (b), 550kHz to 775kHz (c), and 750kHz to 1000kHz (d).

6.5 Results from Mount Sugarloaf

6.5.1 Post-modification Assessment

The interferometric results following hardware modifications are presented in Figure 6.11 taken over a 90^o azimuthal swath. Considerable improvements to the radar image can be shown as a result of these modifications; however, persistent striping in the middle of the radar image is still observable as well as contributions from the ADC. These particular interferers are most noticeable in Figure 6.12 showing the mean correlation profile as function of range. Just as in Figure 6.4, the stripes at ranges (frequencies) of 3011m (501kHz) and 4220m (703kHz) persist even after hardware modifications. Unfortunately, the cause for the middle range stripe is yet to be determined, and should be explored in future endeavors. Closer examination of Figure 6.11 shows streaks in range for multiple azimuth positions. This phenomenon is hypothesized to be caused by nonlinearities encountered after the decoder stage in which a very bright target such as a building amplifies this effect.

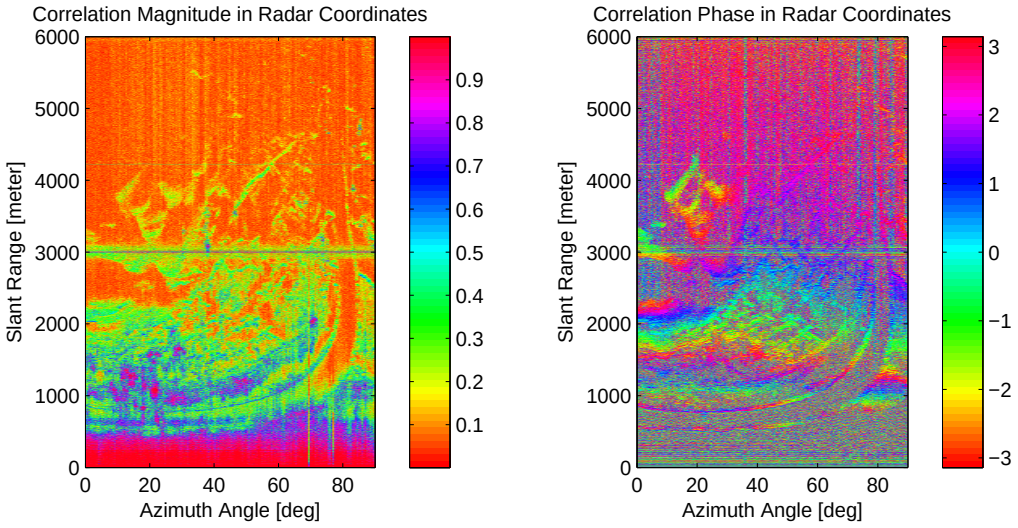

Figure 6.11. Correlation magnitude (left) and interferometric phase (right) observed from Mount Sugarloaf on June 3, 2011.

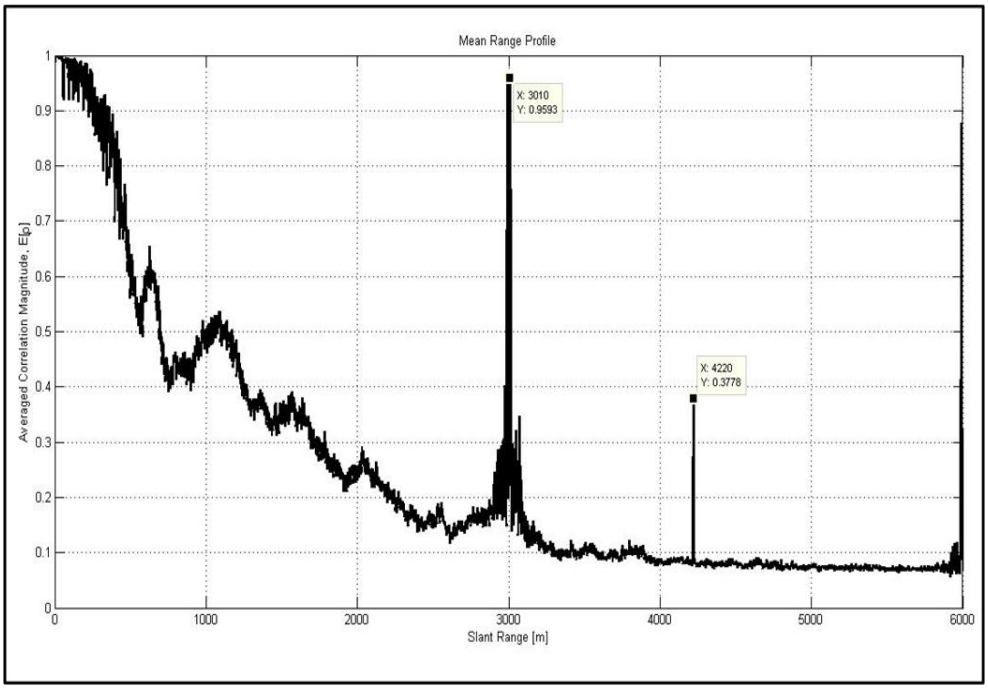

Figure 6.12. Mean range profile from data collected on June 3, 2011.

In comparison to the deployment made in August 2010, the updated radar configuration parameters remained constant with the exception of two changes. First, the maximum scan angle was changed from 120^o to 90^o, and second, the ADC amplitude range was adjusted from the more typical value of $2\mathrm{V_{pp}}$ to $0.4\mathrm{V_{pp}}$. This was employed to increase the receiver gain compensating for an unusually weak signal observed at the ADC. Unfortunately, it was determined later that a reduction in peak transmit power was responsible for this weak signal. As described by (3.8), not only can a loss of transmit power and range, which is proportional to $\frac{1}{R^4}$, affect the sensitivity of a radar. This is important for ground-based radars since at this vantage point ranges varies as a function look-angle. Hence, high SNR is crucial for estimating interferometric phase. Thus, the correlation can be written as a function of SNR expressed as

$$\gamma_{\mathrm{thermal}} = \frac{1}{1 + \frac{1}{\mathrm{SNR}}} \tag{6.1}$$

showing that for high and low values of SNR, γ_{thermal} approaches 1 and 0, respectfully. Thus, a more complete expression for correlation [21] can be written by multiplying (6.1) and (2.2) (Chapter 2) to form the following equation,

$$\gamma_{\text{total}} = \gamma_0 \cdot \gamma_{\text{thermal}}. \tag{6.2}$$

Since the radar interferometer is a two-channel device, an expression taking this characteristic into account is presented in [14] as,

$$\gamma_{\text{thermal}} = \frac{1}{\sqrt{1 + \frac{1}{\text{SNR}^{(0)}}}\sqrt{1 + \frac{1}{\text{SNR}^{(1)}}}} \tag{6.3}$$

where $\text{SNR}^{(0)}$ and $\text{SNR}^{(1)}$ correspond to the channel 0 and channel 1 SNR. Figure 6.13 shows the power measurements at channel 0 and channel 1 collected at the NI ADC for respective deployment dates. Closer examination of Figure 6.13 shows a weaker signal on channel 1 for the June deployment when compared to the same channel 1 data on the August deployment date. When compared to channel 0 this loss of sensitivity proves problematic when computing correlations using (6.2) and (6.3). Hence, the ability to have good interferometric phase estimates becomes more difficult for the June 2011 deployment than for the August 2010 deployment in spite of interference problems encountered by the August 2010 data. Thus, for better measured correlations the accuracy of topographic estimates improves. The relationship between correlation and height estimations are presented in the following section.

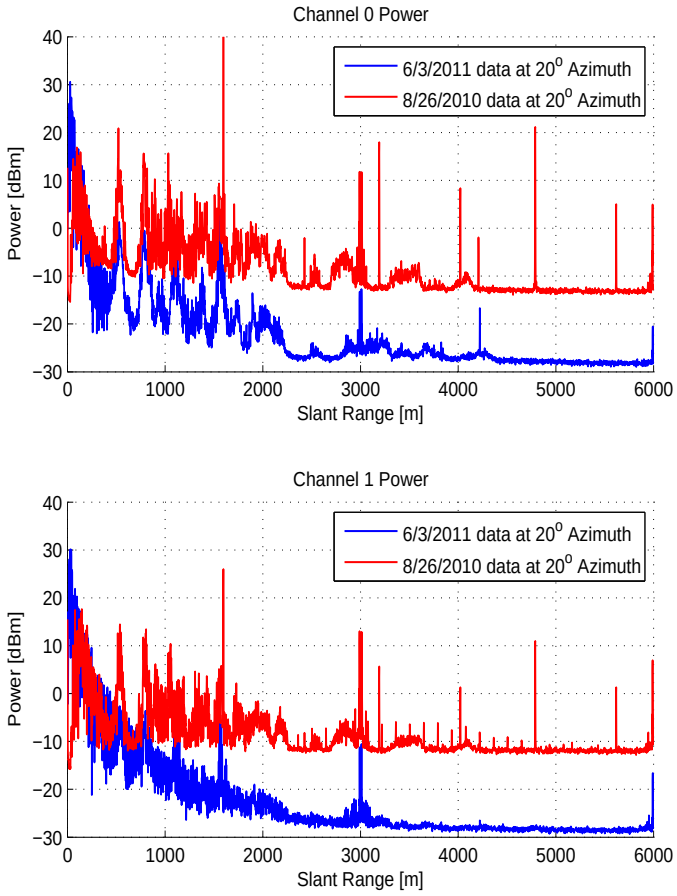

Figure 6.13. Channel 0 and channel 1 power measurement collected at the NI ADC of the August 26, 2010 and June 3, 2011 data.

6.5.2 Estimation of Topography

In this section estimations of topography are presented utilizing some of the fundamental concepts of interferometry described in Chapter 2. For these results, the estimation of topography did not take the direct approach, utilizing a phase unwrapping algorithm[1], instead, a differential interferogram was calculated between the

[1]Phasing unwrapping is a technique converting the topographic induced 2π modulo phase fringes of an interferograms into a map of topography.

measured interferogram, γ, and a simulated interferogram, $\gamma_{\text{simulated}}$, derived from a SRTM digital elevation model (DEM) of the Mount Sugarloaf area. By using this technique, the SRTM DEM acts as a reference point for estimating the topography from the measured interferometric phase. A mathematical expression for the radar DEM is given as

$$h_{\text{radar}} = h_{\text{SRTM}} + \frac{\phi - \phi_{\text{simulated}}}{k_z}. \tag{6.4}$$

where h_{SRTM} represents the SRTM DEM, ϕ represents the measured interferometric phase, $\phi_{\text{simulated}}$ is the SRTM simulated interferometric phase, and k_z is the interferometric wavenumber expressed as the following equation (see also (2.17))

$$k_z = \frac{kB\cos(\alpha - \theta_0)}{R\sin(\theta_0)}. \tag{6.5}$$

Since, the difference between the simulated and measured interferometric phase is expected to be small, it is likely that $h_{\text{radar}} \approx h_{\text{SRTM}}$, thus eliminating the 2π modulo phase ambiguity from the measured interferogram. As a result, the second term in (6.4) can be thought as height difference, Δh, between the SRTM DEM (C-band) and the radar DEM (Ku-band). Hence, (6.4) can be rewritten as

$$h_{\text{radar}} = h_{\text{SRTM}} + \Delta h \tag{6.6}$$

where $\Delta h = \frac{\phi - \phi_{\text{simulated}}}{k_z}$ is a measure of the difference between the radar DEM and the SRTM DEM reference.

In (6.5), the baseline separation B can be approximated as $B = B_0 + \Delta B$ and radar tilt angle α can be approximated as $\alpha = \alpha_0 + \Delta\alpha$, where ΔB and $\Delta\alpha$ are small adjustable parameters with the ability to better fit the computed differential phase, thus accounting for baseline separation and tilt angle errors due to movement or improper positioning during the radar deployment.

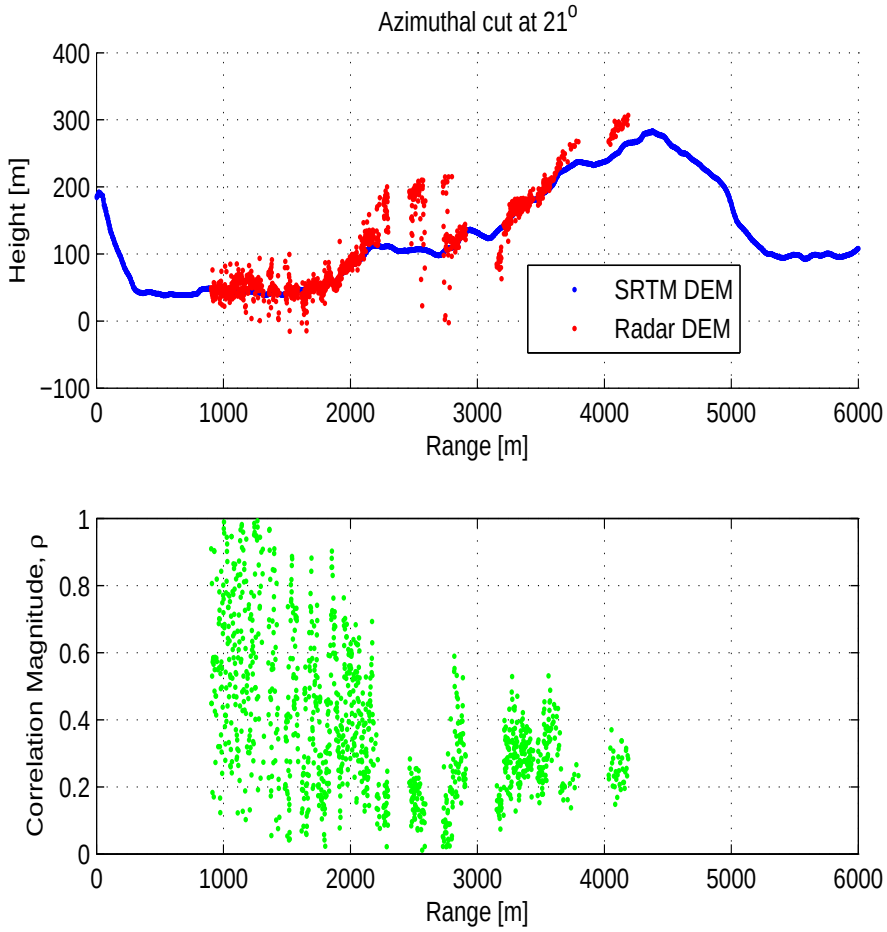

Figure 6.14. A masked profile of the radar DEM overlayed with the SRTM DEM (top) are present with a masked plot of the correlation magnitude (bottom) of data collected on August 26, 2010.

In order to separate usable phase data from unusable phase data contained in areas affected by range stripes, shadowing, and low SNR, a masking process was implemented by partitioning the interferograms into a binary matrix of usable and unusable data pixels. Figure D.2 in Appendix D shows results of a heavily segmented correlation plot. Figures 6.14 and 6.15 present the radar DEM overlayed onto the SRTM DEM, highlighting regions in red where the mask was applied. For both Figures 6.14 and 6.15, the baseline separation and tilt angle were originally assumed

to be 28cm and 90^o implying that $\Delta B = 0$ and $\Delta\alpha = 0$. However, compensation for a phase offset encountered in the June 2011 data using (6.4) required an adjustment to the baseline tilt angle of $\Delta\alpha = -3.2^o$. Accompanying the DEM plots of Figures 6.14 and 6.15 is a masked profile of the correlation magnitude effectively showing the relationship between well correlated data and good height estimations. Closer examination of Figures 6.14 and 6.15 shows higher variation in height estimations for low correlated areas, typically, below values of 0.3.

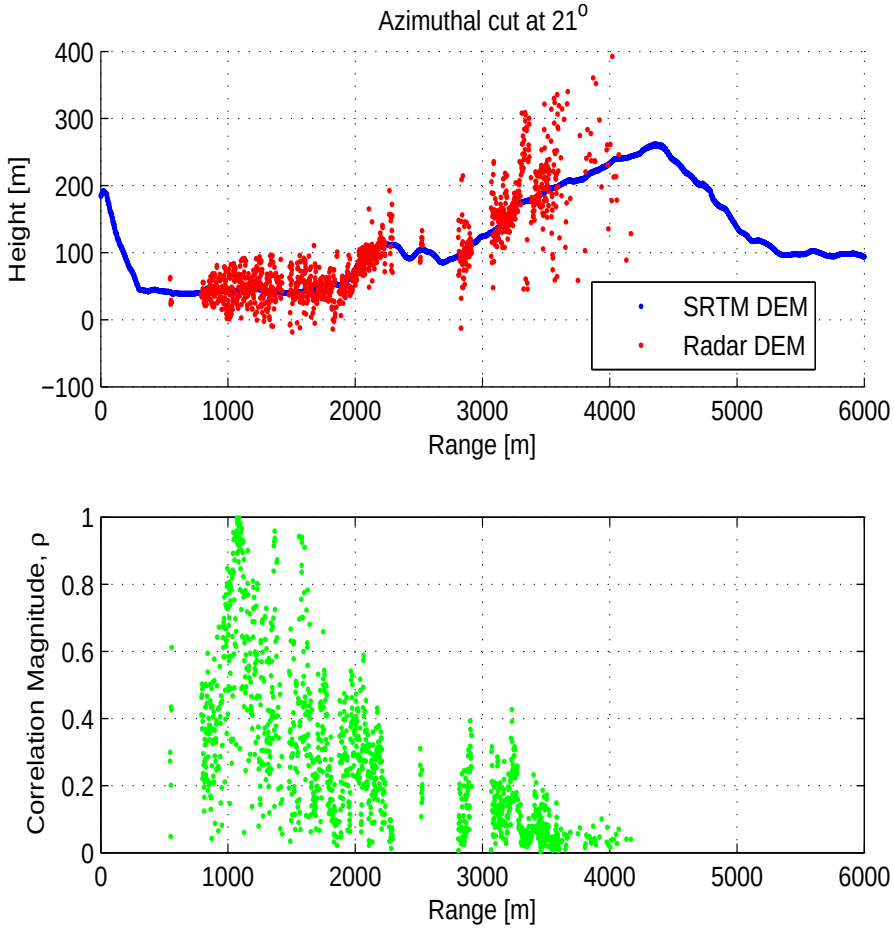

Figure 6.15. A masked profile of the radar DEM overlayed with the SRTM DEM (top) are present with a masked plot of the correlation magnitude (bottom) of data collected on June 3, 2011.

In order to explain the results of overestimated and underestimated heights in the topography, it is important to recognize that imperfections during the masking process may necessitate refinements to the mask. When considering the data used to create the simulated interferogram, small, regional changes in the DEM since the time of the SRTM mission (2000) are expected to have little effect on the overall fit of observation to SRTM data. Furthermore, changes to the landscape during that time period in regard to added vegetation and infrastructure such as buildings, roads, waterways, and farmland are good examples of time-variant targets, providing a potential explanations for masking errors, and, ultimately, height estimation errors.

6.5.3 Geographic Transformation

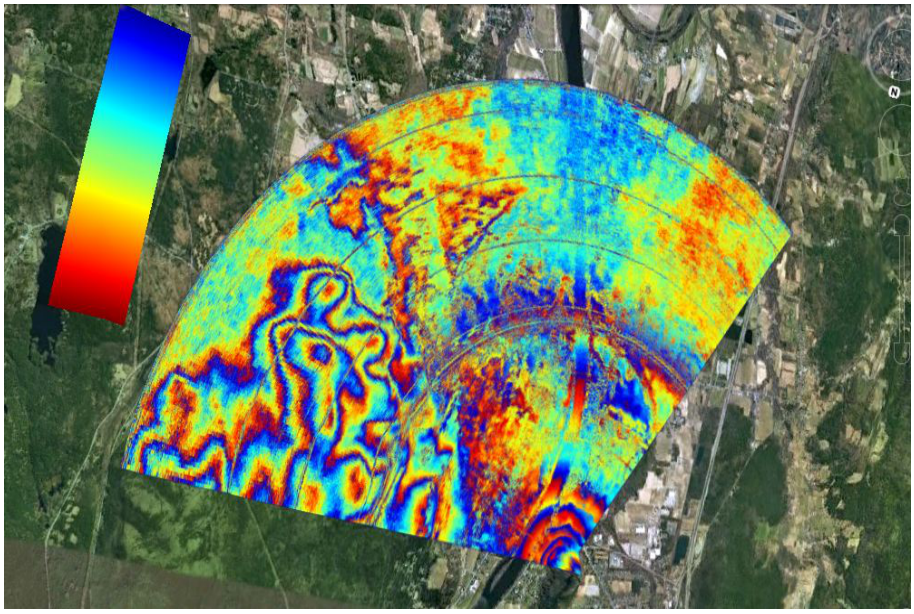

Figure 6.16. The August 26, 2010 radar DEM overlayed in Google Earth

In order to convert from a radar coordinates system (range,azimuth) to a geographic coordinates system (latitude,longitude,altitude), three GPS locations were required in order to properly transform the radar data. These locations were obtained for the radar deployment site as well as two other points in the upper left and upper

right corners of the radar's field of view. These marker locations are listed in Table 6.2 corresponding to the August 2010 and June 2011 radar deployments. These marker locations act as "tie-points" to physical locations on the ground, providing a point of reference during the transformation from radar to geographic coordinates. Figure 6.16 shows the radar DEM from the August 2010 data set in geographic coordinates overlayed into Google Earth.

August 26, 2010	**June 3, 2011**	**Description**
$42^o28'7.56''$N	$42^o28'7.56''$N	Upper left marker latitude location.
$72^o29'59.47''$W	$72^o29'59.47''$W	Upper left mark longitude location.
148m	148m	Upper left marker altitude.
$42^o25'55.02''$N	$42^o24'8.78''$N	Upper right marker latitude location.
$72^o37'55.87''$W	$72^o35'39.99''$W	Upper right mark longitude location.
55m	37m	Upper right marker altitude.
$42^o28'12.66''$N	$42^o28'12.66''$N	Radar latitude location.
$72^o35'31.51''$W	$72^o35'31.51''$W	Radar longitude location.
199m	199m	Radar altitude.

Table 6.2. Marker Locations

The radar deployments conducted at Mount Sugarloaf were used to assess the overall performance of the radar interferometer. However, in the initial test phase of the radar, results collected from the mountain exhibited range striping and interferometric phase problems which were, partially, eliminated following extensive debugging and hardware modifications. Consequently, improvements to the radar's image quality were evident in the plots of the interferogram. As for the overall performance of the radar, the UMass built Ku-band interferometer has demonstrated the capability of a ground-based radar to generate interferometric results and height estimations. For this reason, an airborne application of this radar is highly encouraged and should be employed in the near future. Details on an airborne interferometer are described in Section 7.2.

CHAPTER 7

CONCLUSION

7.1 Summary of Work

In conclusion, this thesis has demonstrated the practical implementation of a ground-based Ku-band radar interferometer, a topic in microwave remote sensing, motivated by the need to characterize high frequency electronics for space applications and the desire to understand the dynamics of Earth on a global scale. In response to these motivating factors, hardware and software developments have contributed into a complete transformation of the original Ku-band radar interferometer [19], increasing the range resolution and sensitivity of the radar. This thesis has described the fundamentals of radar interferometry, and has provided an understanding of the basic principles of FM-CW radar and FM-CW data processing. A detailed description of the instrument has also illustrated some of the key components in the interferometer including the Ku-DDC and slotted-waveguide horn antennas. As part of the quantitative analysis, metrics such as gain, noise figure, isolation, and linearity have provided insight into the performance and capabilities of the instrument. As for the interferometric results observed from Mount Sugarloaf, they have demonstrated the capability of the interferometer to produce high resolution images with the added ability to diagnose and troubleshoot problems that could be encountered on an airplane or spacecraft.

7.2 Recommendations for Future Work

The following sections present recommendations for future work on the current Ku-band radar interferometer.

7.2.1 The Future Airborne Interferometer and Suggested Hardware Modifications

The future outlook for the current Ku-band radar interferometer will involve an airborne conversion that should evolve in two phases, first, as a side-looking aperture radar (SLAR), and finally, as a SAR. In comparison with the ground-based platform, the airborne platform is much better suited for this purpose since there is less restriction in terms of the deployment location. An advantage to deploying the radar from the perspective of an aircraft is that saturation from near-field targets as well as shadowing have less of an affect where as the disadvantage for this type of deployment lies in the aircraft dynamics such as pitch and roll that play a role in the data processing. There are also inherent disadvantages when deploying from an airplane in that the dwell times are limited due to the speed of the aircraft. Fortunately, this can be compensated for by adjusting the pulse rate of the radar and data rate of the NI ADC.

In general the process of converting to an airborne platform will involve a considerable amount of hardware modifications in order to retrofit the current setup to an aircraft setting. In order to meet this challenge, careful attention to the weight and size restrictions of the aircraft as well as the power consumption should be addressed when planning for this type of deployment. Adapting the current antenna assembly to the aircraft's hatchway is an obvious challenge, possibly requiring research into a center-fed Ku-band slotted-waveguide horn antenna designs and perhaps patch antenna designs in order to configure the antennas properly to the body of the airplane. It is recommended that the FM-CW mode of operation be used for this application

due to the low peak power requiring an inexpensive solid-state amplifier. In this mode, modifications will consist of bypassing the L-band to baseband downconversion stage with an equivalent L-band to baseband downconverter that differs from the current downconversion stage by a reduction in gain. This modification to the receiver architecture is advantageous because it lessens the amount of spurious signals introduced by saturation effects caused by coupling between the transmit and receive antennas. Also, the start frequency of the baseband chirp waveform should be increased in order to minimize the contribution of the second image band I_2.

As for the current connectorized transmitter and FM-CW decoder, an upgrade to a PCB layout is recommended in order to reduce the size of the radar by consolidating the transmitter and FM-CW decoder components. In particular, the FM-CW decoder should implement digitally reconfigurable anti-aliasing filters in order to add versatility for various deployment altitudes. For example, this can be implemented either by purchasing surface mount programmable filters capable of providing a variety of filter responses, or by designing a filter bank at various cut-off frequencies by which a multiplexer can by incorporated to switch between different filter responses depending on the deployment location.

The upgraded radar system should also investigate ways to cool the system while in the confined space of the aircraft. As a suggestion, a Peltier cooler, an active electronic cooling system, should be an effective way to transfer heat. These active cooling systems usually draw large amounts of current however, bringing attention to the importance of the aircraft's power budget.

7.2.2 Future Radar Troubleshooting

As mentioned in Chapter 6, range stripes observed around 3011m (501kHz) as well as range streaks observed at multiple azimuth positions have continue to negatively influence the visual performance of the radar image. The purpose of this section is

to provide a troubleshooting scheme that may be helpful in determining the source of these errors.

The recommended method for determining the striping interferer requires finding a relationship between the interferer and a possible alias at the ADC. This can be easily related by collecting data at various sample rates such as 1MHz, 2MHz, 3MHz, and 4MHz. By changing the sample rate of the ADC, the source of this interferer can be designated as an alias if it's position in frequency changes with respect to the sample rate.

The suggested method for determining the effects of the range streaks encountered in radar data will require deploying corner reflector targets in the radar's field of view. By deploying these known targets, it becomes possible not only to determine actual range resolution of the radar but also provides the ability to compare the observed response to the actual response of the reflector. If the reflector response is smeared over multiple range bins, it can be determined that non-linearities in the radar hardware are, in part, responsible for some of the ambiguities in the radar image.

APPENDIX A

WAVEGUIDE ANALYSIS

A.1 Impedance of Wedge Radial Waveguide

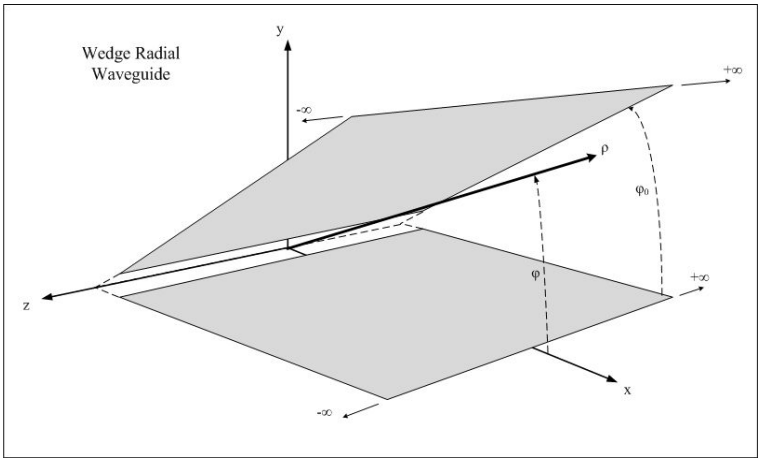

Figure A.1. Illustration of wedge radial waveguide used to approximate the characteristic impedance of an E-plane sectoral horn.

In order to address confusion regarding the expression for wedge impedance found in [18], an analytical formulation for the impedance of a wedge radial waveguide is presented. The wedge radial waveguide can be described using the following TE wave function,

$$\psi^{\mathrm{TE}_p}(\rho,\phi) = \sum_{p=0}^{\infty} \cos\left(\frac{p\pi}{\phi_0}\phi\right) H^{(2)}_{p\pi/\phi_0}(k\rho) \tag{A.1}$$

where $H^{(2)}_{p\pi/\phi_0}(k\rho)$ is the second-order Hankel function for outgoing waves. Given the determination of height, h, presented in Section 4.3.2, a dominant TE_0 mode can be assumed from which (A.1) can be rewritten as

$$\psi^{\mathrm{TE}_0} = H^{(2)}_0(k\rho). \tag{A.2}$$

Using (A.2), the TE field equations of the wedge can be calculated where the electric and magnetic fields can be expressed as

$$E_\phi = \frac{\partial \psi^{\mathrm{TE}_0}}{\partial \rho} = -kH_1^{(2)}(k\rho) \tag{A.3}$$

$$H_z = \frac{k^2 \psi^{\mathrm{TE}_0}}{j2\pi f \mu_0} = \frac{k^2 H_0^{(2)}(k\rho)}{j2\pi f \mu_0}. \tag{A.4}$$

By taking the ratio between these two field equations the wedge radial waveguide impedance is given as

$$Z^{\mathrm{TE}_0}(\rho) = \frac{E_\phi}{H_z} = \frac{c\mu_0 H_1^{(2)}(k\rho)}{jH_0^{(2)}(k\rho)}. \tag{A.5}$$

A.2 Surface Currents in a Rectangular Waveguide: Slot Configuration

The TE_{10} surface currents in a rectangular waveguides are presented in Figure A.2a. Figures A.2b and A.2c highlighting the polarization orientations of surface currents for non-alternating and alternation slot configurations. As discussed in Section 4.3.1, the spacing between adjacent slots is set as $\lambda_g/2$, corresponding to locations along the length of the waveguide where the electric field is strongest, hence, where the surface currents are strongest. Since these surface currents are phased 180^o every $\lambda_g/2$, the slot cuts along the length of the waveguide need to match the current directions suggested by the red highlighted areas in Figures A.2c. Otherwise by following the slot configuration depicted in Figure A.2b, the required uniform phase progression across the array becomes impossible to obtain. Thus, by properly configuring the slots in an alternating pattern, the slot elements, as expected, radiate in-phase forming a beam in the broadside direction.

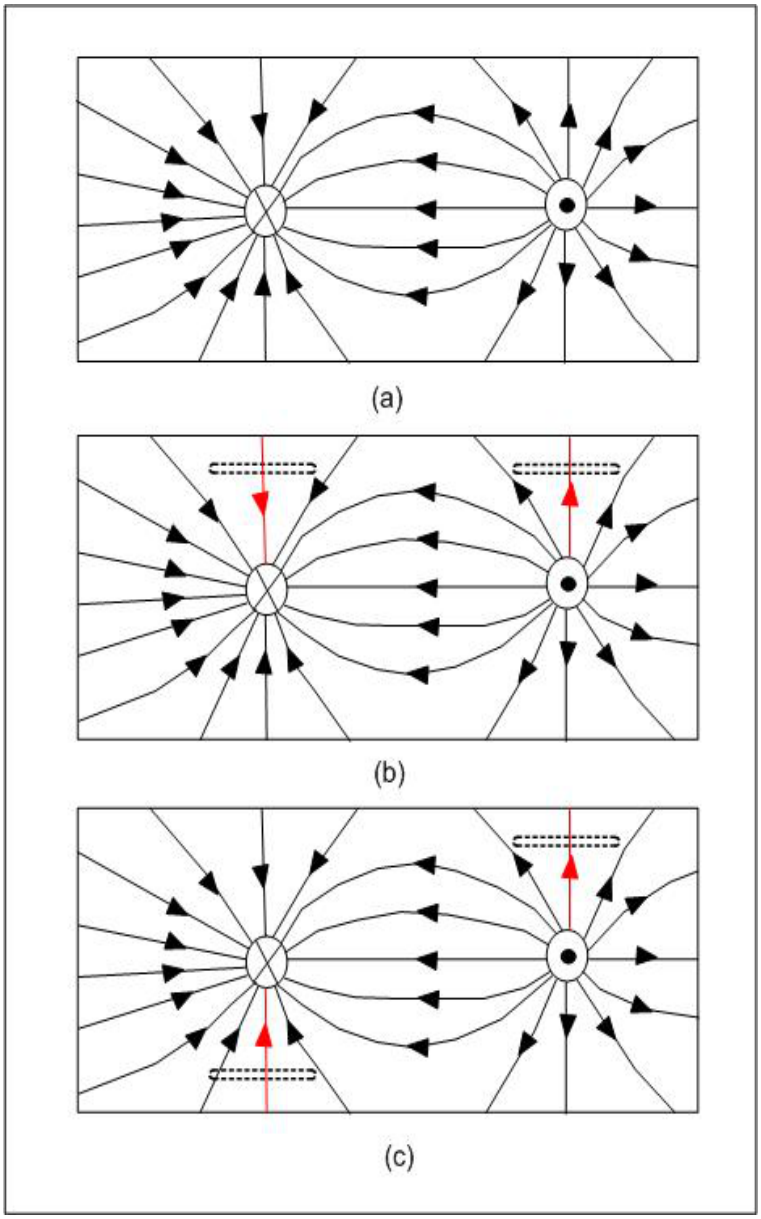

Figure A.2. Illustrations of the TE_{10} surface currents for a rectangular waveguide (a). Highlighted in red are current directions for non-alternating (b) and alternating (c) slot configurations.

APPENDIX B

EDGE-COUPLED FILTERS

Edge-coupled filters are a type of microwave filter where the "staircase" arrangement of microstrip transmission lines along with the coupling interaction between adjacent sections establish a bandpass filter response. Because each section dictates the overall filter response, obtaining a specific type of response such as a Butterworth or Chebychev requires applying the proper weighting coefficients to each section. This ultimately affects the dimensions of each section described by the width, separation, and length. An edge-coupled filter design was recommended because of the lack of surface mount components available at higher microwave frequencies. When designing these types of filters it is important to note that for high frequency designs machining tolerances as well as simulation accuracy may necessitate an iterative approach to the design process. Figure B.1 shows how an edge-coupled filter would appear rendered in Ansoft Designer.

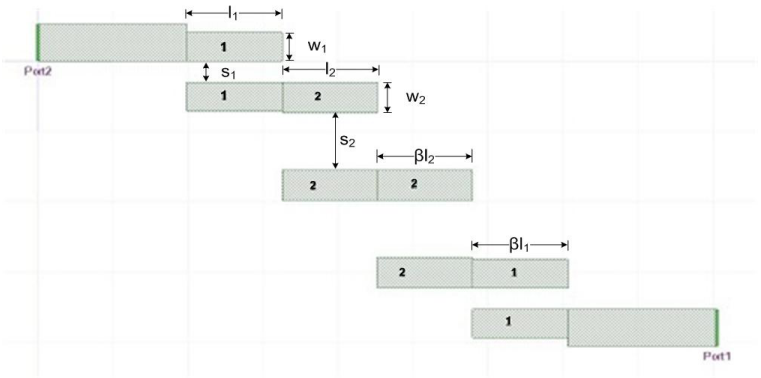

Figure B.1. Edge-Coupled Filter Rendered and Simulated in Ansoft Designer.

The following provides a description of results obtained from existing Ka-band coupled line filters, and demonstrates the simulation capability of Ansoft Designer. Ansoft Designer was chosen for its ability to render the filter problem effectively and produce results in a timely fashion. Unlike Ansoft HFSS, which employs a Finite Element Method (FEM) solver over a three-dimensional space, Designer simulates two-dimensional current meshes using a Method of Moments (MoM) solver, dramatically reducing the complexity of the problem. The Designer suite is appropriate in this regard since edge-coupled filters are planar in structure, thus simplifying the entire design process from drawing to simulation. Figure B.2 shows the actual edge-coupled filters[1] and the end-launch connectors used to connect the filters to test equipment. Figure B.2 also demonstrates how crucial pin-placement is for solderless connections.

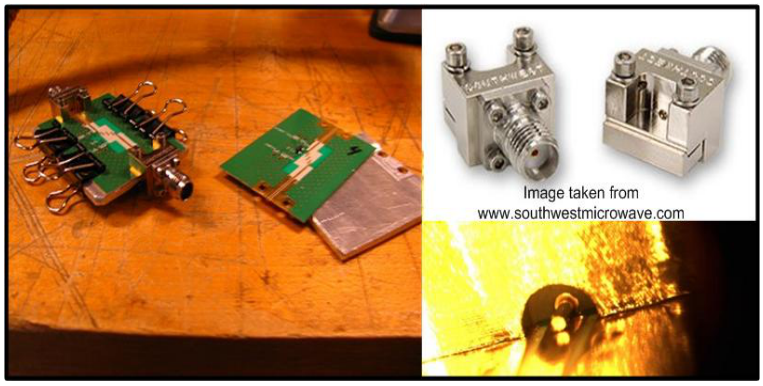

Figure B.2. A picture of the edge-coupled filters (left), the 2.4mm end-launch connectors (top-right), and the proper way to place an end-launch connector (bottom-right).

The design specifications for the edge-coupled filters required a Butterworth or maximally flat response centered at 35.7GHz with 1GHz of bandwidth. The number of sections in the physical structure were dictated by the three pole design. Higher pole designs are problematic and more difficult to implement due to light coupling

[1]Designed by Mark Deluca.

between multiple sections in the physical center of the filter. The design parameters for the edge-coupled filter are described in Table B.1 using Figure B.1 as a reference.

Design Parameter	**Value**
Substrate relative permittivity (Rogers 6002) ϵ_r	2.94
Substrate thickness h	10mil
Section 1 width w_1	16mil
Section 1 separation s_1	12mil
Section 2 width w_2	17mil
Section 2 separation s_2	32mil
Section 1 and 2 length $l_1 = l_2 = l$	{49, 49.5, 50, 50.5, 51}mil

Table B.1. Edge-Coupled Filter Design Specifications

An incremental design approach was implemented in the physical fabrication of these filters. This design approach was accomplished by changing the physical length of each filter section by 0.5mil increments. S-parameter measurements were obtained using a HP8022C vector network analyzer (40GHz) and acquired through a GPIB[2] port connected to LAN switch via a MATLAB user interface. In order to demonstrate the practicality of this design approach, a relationship between frequency and physical length is presented in Figure B.3 showing a plot of S_{11} for section length increments of 1mil. From this plot, it becomes possible to see the inverse proportionality between physical length, l, and frequency, f. This relationship is better understood when describing the filter sections in terms of their electrical length where the typical electrical length for an edge-coupled filter section is given as

$$\beta l = \frac{2\pi}{\lambda_g} l = \frac{\pi}{2} \tag{B.1}$$

where λ_g is the effective center frequency wavelength (or guide wavelength) for microstrip transmission lines. By rearranging terms in (B.1), $l = \lambda/4$ from which the

[2]General Purpose Interface Bus

relationship between frequency and physical length can be expressed mathematically as

$$f \propto \frac{1}{\lambda_g} \propto \frac{1}{l}. \tag{B.2}$$

The relationship presented in (B.2) emphasizes the capability of producing designs in a timely fashion where changes in the physical length are influential to the frequency response of the filter. It is also important to recognize the considerable impedance mismatch from the measured results. This mismatch is primarily a product of the actual design, however, it is possible that poor pin-placement of the endlaunch connector was influential in this poor impedance match.

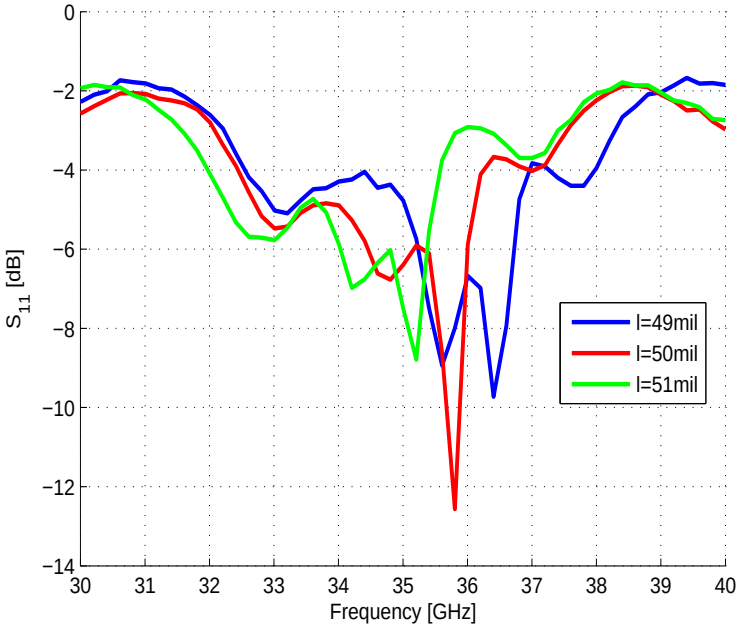

Figure B.3. S_{11} measurements for 1mil increments.

As a prerequisite to simulations, design equations can be used to characterize the filter's performance through even- and odd-mode characteristic impedances, Z_{0e} and Z_{0o}, respectively. These equations [12] allow for a filter design to be synthesized electrically rather than physically, thus, providing a good starting point for initial

designs. The comparison of simulation results to measurement is presented in Figure B.4. Three different simulations were implemented in order to illustrate the sensitivity of the solver when changing simulation parameters. These simulations are listed, presenting specific current mesh scenarios:

1. Simulation #1: Absolute Edge Length, Edge Factor = 12.
2. Simulation #2: Absolute Edge Length, Edge Factor = 36.
3. Simulation #3: Edge Mesh Length Ratio = 0.05, Edge Factor = 36.

As a consequence to increasing the mesh density, simulation results tend to converge to the actual measurement providing sufficient prediction to the actual response of the filter. Hence, by establishing the predicted filter response, a suitable response can be obtained by imposing variation to the dimensions used in the simulation. In most cases, a filter bank consisting of various section lengths, l, allows the designer to exploit the relationship described in (B.2).

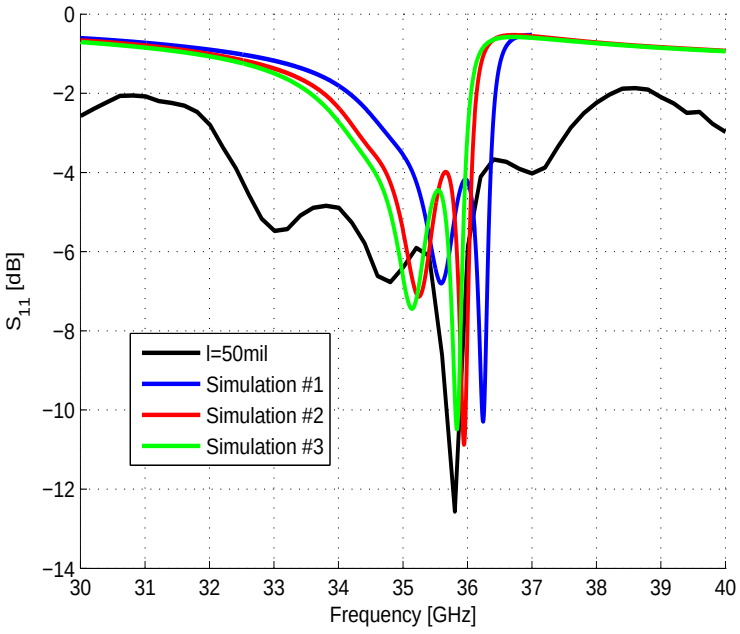

Figure B.4. Simulation versus design.

APPENDIX C

ANTENNA

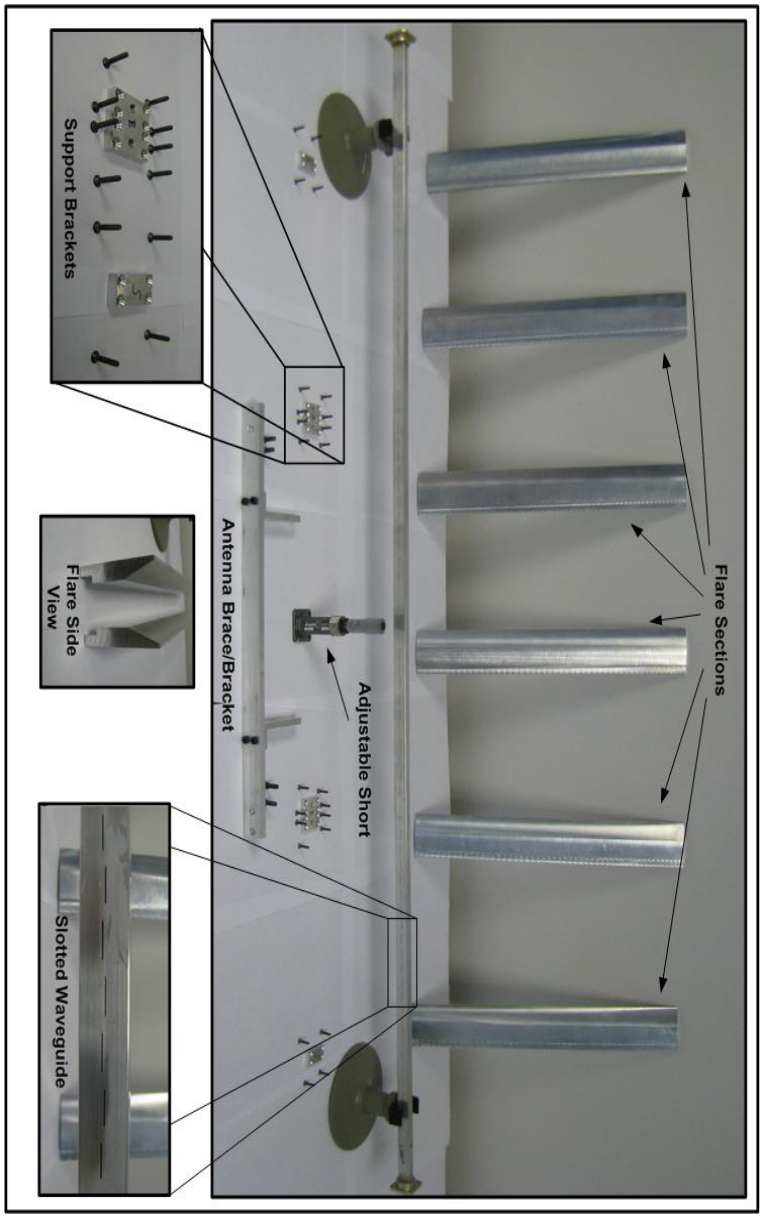

Figure C.1. Exploded view of the slotted-waveguide horn antenna.

APPENDIX D

RADAR PLOTS

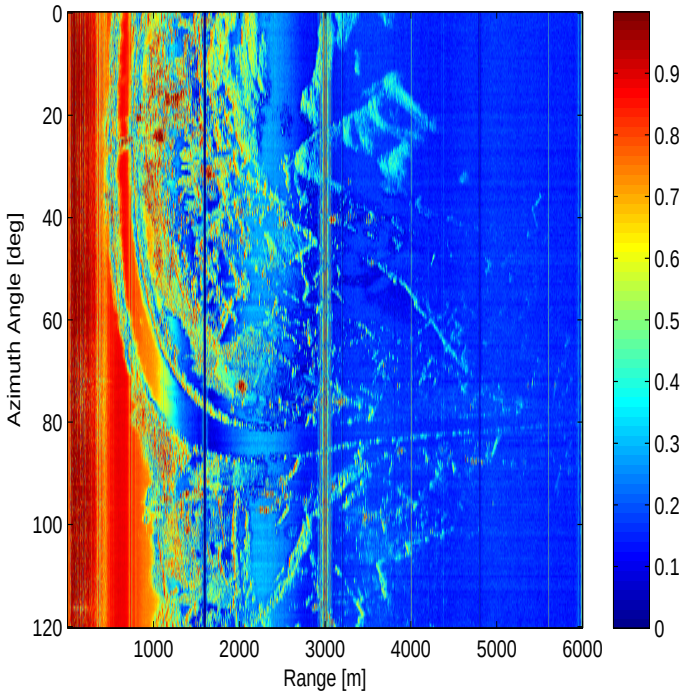

Figure D.1. An image plot of an ensemble average calculated over four scans of the correlation magnitude collected on August 26, 2010. Notice that shadowed regions and areas covered in water which should be uncorrelated are highly correlated.

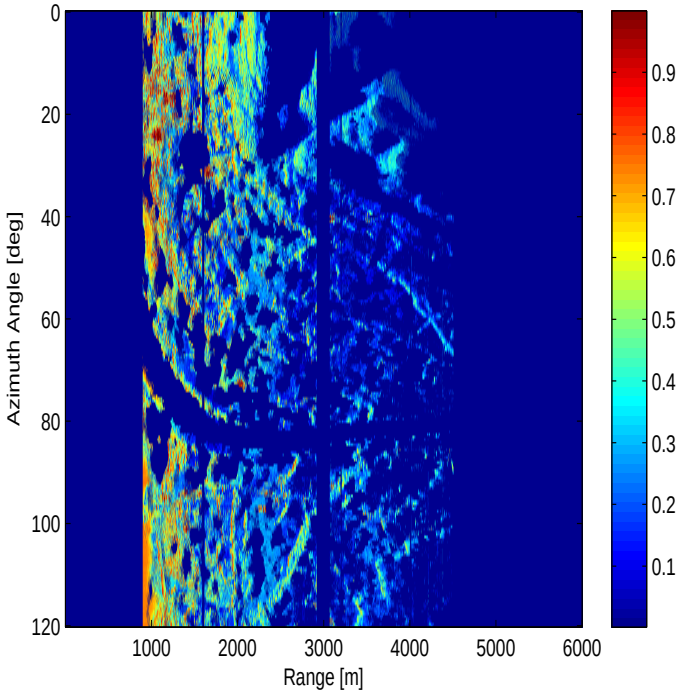

Figure D.2. An illustration of a masked data set collected on August 26, 2010.

BIBLIOGRAPHY

[1] Balanis, Constantine A. *Antenna Theory Analysis and Design*, third ed. John Wiley & Sons, Inc., 2005.

[2] Durand, Michael, Fu, Lee-Lueng, Lettenmaier, Dennis P., Alsdorf, Douglas E., Rodriguez, Ernesto, and Esteban-Fernandez, Daniel. The surface water and ocean topography mission: Observing terrestrial surface water and oceanic submesoscale eddies. *Proceedings of the IEEE 98* (May 2010), 766–779.

[3] Elachi, Charles, and van Zyl, Jakob. *Introduction to the Physics and Techniques of Remote Sensing*, second ed. John Wiley & Sons, Inc., 2006, ch. 6.

[4] Elliott, Robert S., and Kurtz, L. A. The design of small slot arrays. *IEEE Transactions on Antennas and Propagation AP-26* (March 1978), 214–219.

[5] Faller, Nikolaus P., and Meier, Erich H. First results with the airborne single-pass do-sar interferometer. *IEEE Transactions on Geoscience and Remote Sensing 33* (September 1995), 1230–1237.

[6] Graham, Leroy C. Synthetic interferometric radar for topographic mapping. *Proceedings of the IEEE 62* (June 1974), 763–768.

[7] Gruenberg, H. Theory of waveguide-fed slots radiating into parallel-plate regions. *Journal of Applied Physics 23* (July 1952), 733–737.

[8] Hansen, R. C. *Microwave Scanning Antennas: Array Systems*, vol. III. Academic Press, Inc., 1966.

[9] Harrington, Roger F. *Time-Harmonic Electromagnetic Fields*. John Wiley & Sons, Inc., 2001.

[10] Hensley, Scott, Wheeler, Kevin, Sadowy, Greg, Jones, Cathleen, Shaffer, Scott, Zebker, Howard, Miller, Tim, Heavey, Brandon, Chuang, Ernie, Chao, Roger, Vines, Ken, Nishimoto, Kouji, Prater, Jack, Carrico, Bruce, Chamberlain, Neil, Shimada, Joanne, Simard, Marc, Chapman, Bruce, Muellerschoen, Ron, Le, Charles, Michel, Thierry, Hamilton, Gary, Robinson, David, Neumann, Greg, Meyer, Robert, Smith, Phil, Granger, Jim, Rosen, Paul, Flower, Dennis, and Smith, Robert. The uavsar instrument: Description and first results. In *Radar Conference* (2008).

[11] Li, Fuk K., and Goldstein, Richard M. Studies of multibaseline spaceborne interferometric synthetic aperture radar. *IEEE Transactions on Geoscience and Remote Sensing 28* (January 1986), 88–97.

[12] Pozar, David M. *Microwave Engineering*, third ed. John Wiley & Sons, Inc., 2005.

[13] Rogers, A. E. E., and Ingalls, R. P. Venus: Mapping the surface reflectivity by radar interferometry. *Science 165* (August 1969), 797–799.

[14] Rosen, Paul A., Hensely, Scott, Joughin, Ian R., Li, Fuk K., Madsen, Søren N., Rodríguez, Ernesto, and Goldstein, Richard M. Synthetic aperture radar interferometry. *Proceedings of the IEEE 88* (March 2000), 333–382.

[15] Siqueira, Paul, Ahmed, Razi, Wirth, John W., and Bachmann, Alex. Variable precision two-channel phase, amplitude, and timing measurements for radar interferometry and polarimetry. *IEEE Transactions on Microwave Theory and Techniques 55* (October 2007), 2248–2256.

[16] Skolnik, Merrill I. *Introduction to Radar Systems*, third ed. The McGraw-Hill Companies, Inc., 2001.

[17] Stevenson, A. F. Theory of slots in rectangular waveguides. *Journal of Applied Physics 19* (January 1948), 24–38.

[18] Vedantham, Harish. Design and development of a ka-band interferometer for cryospheric applications. Master's thesis, University of Massachusetts, Amherst, 2009.

[19] Venkatasubramanian, Karthik Srinivasan. Design and development of timmi - an interferometric radar. Master's thesis, University of Massachusetts, Amherst, 2007.

[20] Werner, Charles, Strozzi, Tazio, Wiesmann, Andreas, and Wegmüller, Urs. A ground-based real-aperture instrument for differential interferometry. In *IEEE Radar Conference* (2009).

[21] Zebker, Howard A., and Villasenor, John. Decorrelation in interferometric radar echoes. *IEEE Transactions on Geoscience and Remote Sensing 30* (September 1992), 950–959.

[22] Zisk, S. H. Lunar topography: First radar-interferometer measurements of the alphonsus-ptolemaeus-arzachel region. *Science 178* (December 1972), 977–980.